Model Deficiencies of ERA5 Atmospheric Reanalysis Over Arctic Sea-Ice

Analysis of the Winter Surface Radiative Energy Budget by Using MOSAiC and Satellite Observations.

Lia Herrmannsdörfer

Department of Geosciences
Faculty of mathematics and natural sciences

UNIVERSITY OF OSLO

February 2022

Acknowledgements

First and foremost, I would like to thank my supervisor Malte Müller for inspiring the thesis' topic, combining highly interesting data from the worlds of models and measurements. Thank you for always giving constructive feedback, for pointing out interesting aspects and for encouraging me to develop own ideas and strategies. I could not have wished for supervision with better balance of support and freedom.

I also like to thank Yurii Batrak for extracting and merging the MODIS data into a tidy format.

Huge thanks also to Matthew Shupe and his team at NOAA for sharing the MOSAiC Distributed Network data. Thanks to Philip Rostosky and Gunnar Spreen from the University of Bremen for providing the AMSR-E/2 snow depth data and to Sang-Moo Lee from the University of Colorado for helping with the AMSR/AVHRR snow depth data.

Thanks to the Norwegian Meteorological Institute for providing equipment.

Abstract

As part of the global climate change the Arctic is warming rapidly. The surface energy budget is a central aspect of the Arctic system with sea ice growth and melt. However, the representation of the surface energy budget and its components has large errors in atmospheric reanalyses, which are often used for climate model comparisons, forcing of ocean and sea ice models and initialisation of climate predictions. Since observations of the Arctic surface energy budget are sparse, expeditions like MOSAiC (2019/2020) are crucial to understand the components of the Arctic system and to validate global and regional earth system and forecasting models. In order to analyse deficiencies of the surface radiative energy budget over Arctic sea ice in clear sky conditions and possible error sources, the ERA5 global atmospheric reanalysis is compared to the MOSAiC campaign data from December 2019 to February 2020 and to the pan-Arctic MODIS ice surface temperature remote sensing product. The analysis shows a *surface temperature* warm bias of 4°C to 6°C in clear sky conditions. Furthermore, ERA5 is not able to distinguish the observed radiative Arctic winter states, but simulates the timing of clear sky periods sufficiently. The sensitivity analysis of possible error sources, by including satellite products of snow depth and sea ice thickness, shows that the main errors are caused by insufficient *ice thickness* and *snow depth* representation in the reanalysis system.

Contents

Chapter 1

Introduction

The Earth's source of energy is characterised by the incoming solar radiation, distributed unevenly due to the surface's curvature. The imbalance between the poles and equatorial regions cause a poleward energy transport, that is basis for all atmospheric circulation. As such, the Arctic surface energy budget is not only a central aspect of the Arctic system, defining sea ice growth and melt through radiative feedbacks. It also influences the Earth's changing climate [Serreze and Barry, 2014]. The winter Arctic radiative surface energy budget is mainly dependent on the long wave radiation, as the shortwave radiation is zero during the polar night. The radiative energy budget is thereby composed by long wave radiation at the surface, emitted downwards from the atmosphere and emitted upwards into the atmosphere. Consequently, it is also influenced by the presence of clouds and the atmospheric boundary layer stability. Sea ice and snow layers alter the budget by hemming the subsurface energy flux from the ocean into the atmosphere [Zhang et al., 1996; Shupe et al., 2020a; Stramler et al., 2011; Walden et al., 2017; Kayser et al., 2017; Sedlar et al., 2021].

Global and regional earth system and forecasting models are used for simulating the components of the Arctic system, like atmosphere, ocean and cryosphere, and for predicting its future state. Still, the representation of the surface energy budget and its components in models, such as the ERA5 global atmospheric reanalysis, have large errors [Kayser et al., 2017; Graham et al., 2017]. From previous studies, a warm bias of surface temperature was discovered in ERA5 reanalysis for winter clear sky periods in the sea ice covered Arctic [Batrak and Müller, 2019; Krumpen et al., 2021].

As conventional observations of the Arctic are sparse, expeditions are crucial for understanding the Arctic system and improving models in the Arctic domain. The history of polar explorations is reaching back more than a century. Nowadays, scientific expeditions offer a wide range of interdis-

ciplinary observations. Examples are the Surface Heat Budget of the Arctic Ocean (SHEBA) expedition (1997/1998) [Uttal et al., 2002] and the recent decade Norwegian Young Sea Ice (N-ICE2015) expedition (2015) [Cohen et al., 2017]. The recent expedition of Multidisciplinary drifting Observatory for the Study of Arctic Climate (MOSAiC), took place from autumn 2019 to summer 2020, drifting across the Arctic Basin. The gathered data shall help to understand the components of the Arctic System, their interaction, spatial variability and heterogeneity of processes at multiple scales and during the seasonal cycle [Barber et al., 2020; Shupe et al., 2020b].

Satellite observations allow for a spatial coherent view, can be used to compare conventional and expedition observations to an Arctic context and act as model input. For example, MODIS provides a wide range of Earth observation variables on a global scale and in high spatial and temporal resolution in the Arctic [Hall et al., 2004; Hall and Riggs, 2015a].

In this work, ERA5 reanalysis deficiencies of the surface radiative energy budget on Arctic sea ice in clear sky condition are analysed, for the example of the MOSAiC expedition winter from December 2019 to February 2020. The warm bias and surface temperature errors are assessed for the MOSAiC winter trajectory and pan-Arctic, for two example periods of the MOSAiC winter. Furthermore, two main model problems, contributing to the warm bias, will be addressed. These are the ability of ERA5 simulating clear sky conditions, as part of the two Arctic atmospheric states and consequences of lacking sufficient representation of sea ice and snow layers. Therefore, surface and near surface MOSAiC observations are compared to ERA5 reanalysis, for the 2019/2020 winter along the winter MOSAiC trajectory. Pan-Arctic MODIS *ice surface temperature* observations are used for selected cloud-free periods to compliment the MOSAiC winter data set. In addition, *snow depth* and *ice thickness* are used, that are based on CryoSat-2, AMSR-E/2 and AVHRR satellite measurements.
In the following, used data and methods are described in chapter 2. In chapter 3, the surface energy budget and its radiative states are explained theoretically, Arctic expeditions are described and previous comparisons to ERA5 reanalysis are summarised. In addition, conditions of sea ice, snow and atmosphere during MOSAiC winter are compared to the conditions of previous decades. Chapter 4 contains the first part of the analysis results, comparing ERA5 to the MOSAiC winter trajectory. Chapter 5 analyses model capabilities in clear sky conditions in more detail along the trajectory and expands to an Arctic context. In chapter 6, the main results are discussed and compared to previous findings. Chapter 7 gives a summary and an outlook for the future, concerning the analysed deficiencies.

Chapter 2

Data & Methods

In this work, model and observational data from multiple sources is used. An overview is given in table 7.1.

2.1 ERA5 Reanalysis

ERA5 is a widely used, global reanalysis covering the time period of 1979 until present at a resolution of 31 km (HRES). It uses Integrated Forecasting System (IFS) version Cy41r2 from 2016 and is provided by the European Centre for Medium-Range Weather Forecasts (ECMWF). The main ERA5 components are ATMO (atmosphere), LAND (land surface), WAVE (ocean waves), SST (sea surface temperature) and ICE (sea ice). All of the components are coupled [Hersbach et al., 2020].

The data assimilation (DA) consists of multiple parts. A 4-dimensional Variational Data Assimilation (4D-VAR) with 12h assimilation window is used. It evaluates the smallest possible error through minimising the cost function for projecting the analysis state from model background and observations. The Ensemble Data Assimilation (EDA) is a component of 4D-Var and contains one control member and 9 perturbed members. Land Data Assimilation (LDAS) includes 1D and 2D Optimal Interpolation (OI) and a Kalman Filter. Another DA is the Ocean Wave Optimal Interpolation (OI). A large number of in-situ and remote sensing observations are assimilated into the model [Hersbach et al., 2020].

Conventional observations, gathered from near-surface land stations (SYNOP), drifting and moored buoys (DRIBU), radiosondes and dropsondes (TEMP), balloons (PILOT) and airplanes (AIRCRAFT), are used. In addition, data from polar orbiting and geostationary satellites is used. Microwave and infrared radiometers (e.g. AMSR-2) measure radiance for deriving temperature and humidity profiles. Altimeter (e.g. CryoSat) measure

the distance of the Earth's surface and thus can provide *ocean wave height* or *sea ice thickness*. Scatterometer supply wind and soil moisture measures. Also, wind can be derived from atmospheric motion vectors. A blacklist excludes observations related to general retrieval methods, sources, regions and time periods, that decrease the accuracy of the model output. In addition, historical data sets are reprocessed for improved quality and calibration [Hersbach et al., 2020].

As boundary conditions, climatological information, such as aerosols, greenhouse gases, ozone and related radiation forcing, is needed. The ocean boundary is prescribed by set *sea surface temperature* (SST) and *sea ice concentration* (CI) from perturbed observations (e.g. OSI SAF). The ice edge is defined at $CI = 15\%$ and the Central Arctic can have CI under 100% [Hersbach et al., 2020].

The reanalysis uses tiles that are assigned one or multiple surface types for the length of the forecast. The surface energy budget and top surface layer temperature (SKT) are in balance with the fluxes for each tile. SKT is calculated due to the surface type of the tile and, thus, is equal to SST for tiles with water surface only and equal to *ice surface temperature* IST for sea ice surfaces only. Sea ice is modelled with 4 layers, adding up to a total, constant thickness of $1.5\,m$ with no snow on top. The heat transfer trough the sea ice is defined by the ice temperature, the constant volumetric heat capacity and set thermal conductivity of the ice. Sea water ($SST = -1.7°\mathrm{C}$) and atmosphere (SKT) act as lower and upper boundary layers [ECMWF, 2016].

In the present work, the global reanalysis ERA5 is used in a pan-Arctic context with a grid size of 1440×240, and with the nearest grid cell along the trajectory for hourly time steps. The variables used for the analysis are *downwelling* and *net surface long wave radiation* (LWD, LWN), $2\,m$ *air temperature* ($T2M$), *surface skin temperature* (SKT), *ice surface temperature* (IST), *ice temperature of layer 1* ($ISTL$), *mean* $10\,m$ *wind speed in u and v direction* ($u10m, v10m$), *mean sea level air pressure* (pp) and *sea ice concentration* (CI). The ERA5 data is available from the Copernicus Climate Change Service (C3S) Climate Data Store (`https://cds.climate.copernicus.eu/`).

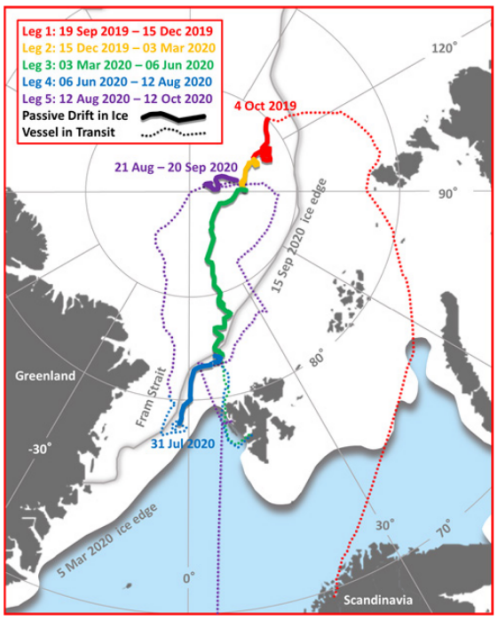

Figure 2.1: MOSAiC expedition drift with the natural ice movement (solid) and transits for ship repositioning, resupply and crew exchange (dashed) with expedition phases, called Legs (colouring) and the ice edges of March and September. Taken from [Shupe et al., 2020b] (Figure 2).

2.2 MOSAiC Expedition

The Multidisciplinary drifting Observatory for the Study of Arctic Climate (MOSAiC) has been an international, interdisciplinary initiative during the Year of Polar Prediction (YOPP). The year-long expedition provided a platform to measurements of various components of the Arctic System at multiple scales and during the same time periods [Barber et al., 2020; Shupe et al., 2020b].

Resembling the original Fram Expedition, the icebreaker Polarstern was moored to an ice floe, to drift along with the natural movement of the sea ice. The transpolar drift started in the Laptev Sea in September 2019, continued through the Central Arctic close to the geographical North Pole and arrived in the Fram Strait in July 2020 (see figure 2.1). Because the drift speed was higher than expected, Polarstern was relocated in the Central Arctic in August to September 2020 [Barber et al., 2020; Shupe et al., 2020b].

The expedition duration allows for measuring the seasonal cycle of the Arctic system components atmosphere, ocean, cryosphere and biosphere, and their interaction. Various measurement devices are used to sense the thermodynamic structure, boundary layer, clouds, precipitation, aerosols,

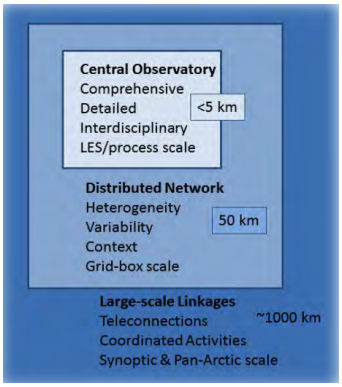

Figure 2.2: Schematic of MOSAiC levels of observations: Central Observatory, Distributed Network and Extended Network. Taken from [Barber et al., 2020] (Figure 3.1).

surface layer and various other information from the atmosphere. Measurements also cover sea ice and snow properties, their mass balance and morphology. For the ocean, momentum, heat and freshwater budget, ocean layers, mixing and turbulence are covered. The observations are also meant to detect the impact of climate change on the Arctic system [Shupe et al., 2020b,a; Barber et al., 2020].

MOSAiC also aims at working at different scales (see figure 2.2). The Central Observatory (CO) targets at understanding processes and interaction in detail and at a small scale. The measurement network of the CO is deployed on board Polarstern and on the surrounding ice within a distance of $5\,km$ [Barber et al., 2020].
The Distributed (Regional) Network (DN) is set up in a $5\,km$ to $50\,km$ circle around the ship and central floe with various manned, autonomous or remotely accessibly sites (see figure 2.3). The DN is meant to examine spatial variability and heterogeneity of processes, separate the spatial differences from temporal ones and deliver boundary conditions for the detailed processes discovered in the CO. It is designed to fit the model grid scales of Regional Climate Models and Earth System Models [Barber et al., 2020].
At a $1000\,km$-scale, observations from ships, drifting ice stations, buoys, satellites and air crafts are coordinated across the entire Arctic Basin. This Extended Network can show component interactions and boundary conditions on an even larger scale (see figures 2.2, 2.3) [Barber et al., 2020].

In addition to the observations, modelling is used to fill spatial and temporal gaps, to relate the regional context to global processes and to link MOSAiC to other studies. In addition, some observations are assimilated into Climate Models and Weather Forecast Systems. For example, radio-

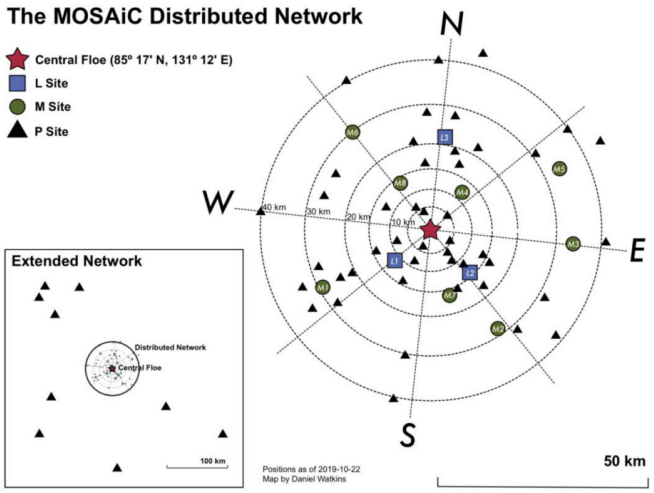

Figure 2.3: Example for the relative position of MOSAiC Central Floe, Distributed Network and Extended Network including DN sites L1, L2 and L3. Taken from [Shupe et al., 2020a] (Figure 3).

sonde observations are assimilated into 2019-2020 ERA5 Reanalysis [Barber et al., 2020].

The data used in this study was gathered by Atmospheric Flux Stations (ASFS) mounted on sledges at DN sites L1, L2 and L3 (see figure 2.3). The ASFSs contain broadband radiometers for measuring surface long and short wave radiation facing up- and downwards, sensors for measuring near surface meteorological variables and sonic anemometers for measuring wind variables. The ASFS also have water vapour sensors and flux plates for measuring conductive heat fluxes. The ASFS sledges were designed for the MOSAiC expedition by the University of Colorado, in cooperation with CIRES and NOAA Physical Sciences Laboratory [Shupe et al., 2020a]. In this thesis, Level-2 preliminary data is used, which is quality controlled for the used time period and variables [Shupe, 2021, pers. Commun.].
It has a $10\,min$ resolution along the trajectory and is available for the largest part of the used winter months December, January and February. In detail, the availability is 12.1.2019 to 26.2.2020 for ASFS30 and ASFS40 at L2 and L1. ASFS50 data from L3 is only available from 12.1.2019 to 23.1.2020 and 30.1.2020 to 5.2.2020. The reasons are damages by a severe storm in the end of January and ice deformation at L3 in the beginning of February, which caused the Flux sledge to fall over and get further damaged [Onl, 2020]. In this work, the ASFS variables *up and downwelling long wave radiation* (LWU, LWD), *2m air temperature* $(T2M)$, *ice surface temperature* (IST), *surface air pressure* (pp), *wind direction* (w_{dir}) and *wind speed* (w_{sp}), will be used .

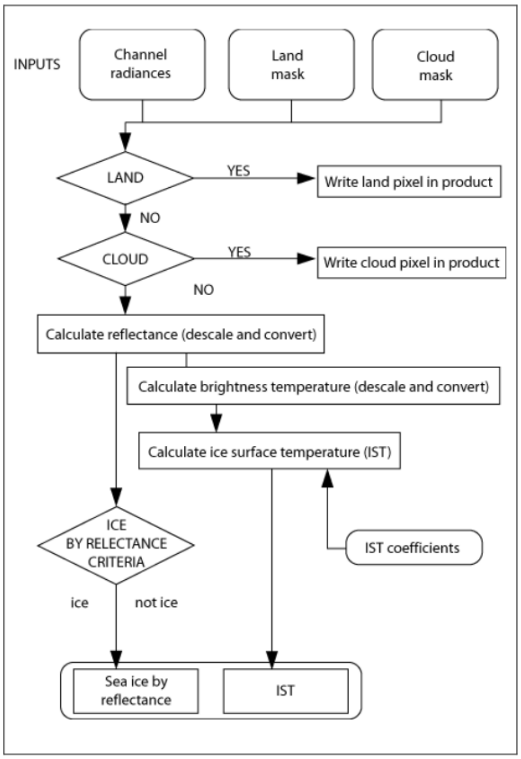

Figure 2.4: MODIS *ice surface temperature* IST retrieval scheme. Taken from Hall and Riggs [2015a] (Figure 3).

2.3 MODIS Ice Surface Temperature

The Moderate Resolution Imaging Spectroradiometer (MODIS) provides numerous measurements at different wavelengths ranges (Bands) on a global coverage and a frequency of about $99\,min$ at the poles [Hall and Riggs, 2015a]. In the following, the retrieval algorithm for *ice surface temperature* is explained.

First, calibrated channel radiance is filtered for cloud-free ocean pixels using land mask (geolocation) and cloud mask (see figure 2.4). Second, reflectance calculated from input radiance is then used to retrieve the IST and to identify pixels with sea ice [Hall and Riggs, 2015a].
In order to detect sea ice, a criteria test is applied, that is based on reflectance at visible and near-infrared spectrum. Assuming a snow cover on top of the sea ice, the *normalised difference snow index* ($NDSI$) is calculated using reflectance of Band 4 at $0.55\,\mu m$ and Band 6 at $1.66\,\mu m$. Pixels that satisfy a $NDSI > 0.4$, Band 2 reflectance > 0.11 and Band 1 reflectance > 0.10, are identified as sea ice [Hall and Riggs, 2015a].

$$NDSI = \frac{(Band4 - Band6)}{(Band4 + Band6)}$$

In order to derive the IST, sensor radiances E $[mWm^2srcm^{-4}]$ at bands 31/32 with $11\,\mu m/12\,\mu m$ are converted into brightness temperatures Tb $[K]$ using central wavelength v $[cm^{-1}]$, emissivity e and constants $ci/c2$ [Hall and Riggs, 2015a].

$$Tb = \frac{c_2 v}{ln(\frac{1+ec_1v^3}{E})}$$

A split window technique, adapted from Advanced Very High Resolution Radiometer (AVHRR), is now applied using band 31/32 Tb and sensor scan angle q. a, b, c, d are coefficients of multi-linear regression between Tb and *surface temperature* for different temperature ranges [Hall and Riggs, 2015a].

$$IST = a + bT_{31} + c(Tb_{31} - Tb_{32}) + d[(Tb_{31} - Tb_{32})(seq(q) - 1)]$$

The product is limited to cloud free ocean pixels and also applied to ocean pixels without sea ice, in the first place. These need to be filtered out during the use of IST, as the method is not designed for open water. The MODIS IST is available for day and night time [Hall and Riggs, 2015a; Hall et al., 2004].

Errors result from all input parameters, radiance, geolocation and cloud mask. The conservative nature of the cloud mask allows for the presence of clouds or water vapour without being detected by the mask. The inconstant scan angle contributes to the total error, too. More problems lie in the difficulty of distinguishing clouds and ice surfaces due to their resembling temperature range. In addition, the range of possible humidity and temperature states are more variable than the retrieval method coefficients consider. The emissivity of snow and ice are also not known in detail [Hall and Riggs, 2015a; Hall et al., 2004].

Hall et al. [2004] compared MODIS IST to observational data from drifting buoys and multiple microwave and thermal sensors in the Arctic and Antarctic. Despite the described problems and errors, Hall et al. [2004] found, that MODIS performed reasonably well in polar winter conditions with a small bias of $-2.1\,K$ and $3.7\,K$ RMSE. If additional cloud and fog filtering was applied, the results were even better in clear sky conditions with $-0.9K$ bias and RMSE $1.6\,K$. With $\pm 1\,K$ error and no offset, Scambos et al. [2006] made resembling findings comparing MODIS IST to ship and airborne infrared radiometric measurements in the autumn Antarctic of $245 - 270\,K$ temperature range. Scambos et al. [2006] also discovered, that the *ice surface temperature* is influenced strongly by near surface inversions in cold, clear sky conditions. It must be considered, that the retrieval method was likely improved since this uncertainty estimates were made.

In this thesis, a composite of Level-2 MOD29 and MYD29 hourly aggregated swaths, from the MODIS instruments onboard the Terra and Aqua satellites, is used for the Arctic region. The resolution is $5\,km$ on a polar stereographic grid of size 1800×1400. Only non-land mask pixels are used.

2.4 CryoSat-2/SMOS Sea Ice Thickness

CryoSat-2/SMOS *analysis sea ice thickness* (h_i) is a composite using sea ice products from ESA SMOS (Soil Moisture and Ocean Salinity) and CryoSat-2 (CS2) satellite. Due to different sensitivities of SMOS and CryoSat-2, the entire *sea ice thickness* range is covered while the uncertainty is reduced [Ricker et al., 2017].

Sea ice thickness can be calculated from CryoSat-2 altimeter *ice freeboard* (Fb_i) and Warren snow climatology ($W99$). The method's relative error is small over thick MYI $> 1\,m$ and large over thin FYI $< 1\,m$ (see figure 2.5). Sources of uncertainties are diverse including *snow and ice density*, *ocean surface height*, *W99* climatology, *sea ice concentration* (CI) under 100% and latitude dependent data coverage [Ricker et al., 2017].
Sea ice thickness can also be obtained from SMOS microwave radiometer *brightness temperature* (Tb) at $1.4\,GHz$ for latitudes $< 85°North$. The SMOS *sea ice thickness* relative error is high for thick perennial ice $> 1\,m$ and small for thin FYI (see figure 2.5). Therefore, SMOS is not used for MYI regions defined by Ocean and Sea Ice-SAF (OSI-SAF) ice type product. Upon other terms, sources of uncertainty are *sea ice concentration* under 100%, assumed fluxes and *snow depth*. The product is dependent on the *air temperature* and temperature gradient within the sea ice [Ricker et al., 2017].

In order to merge the two data sets, two methods are applied. The weighted mean (WM) weights the observations according to the individual product uncertainties at grid cells with observations available [Ricker et al., 2017].
The optimal interpolation (OI) scheme both weights observations due to their uncertainties and minimises the observational error. As weekly background fields for the OI, CS2 and SMOS data is weighted and averaged $1-2$ weeks before and after the target week. In addition, a nearest neighbour scheme is applied to fill the gaps, a low pass filter is implemented and grid cells with OSI SAF $CI < 15\%$ are eliminated. Therefore, OSI SAF CI and sea ice type are averaged over the analysed week as additional background fields. The correlation length scale is chosen dependent on the local ice thickness gradient. Applying the OI, observational error and covariances are minimised using weekly observations and background fields [Ricker et al., 2017].

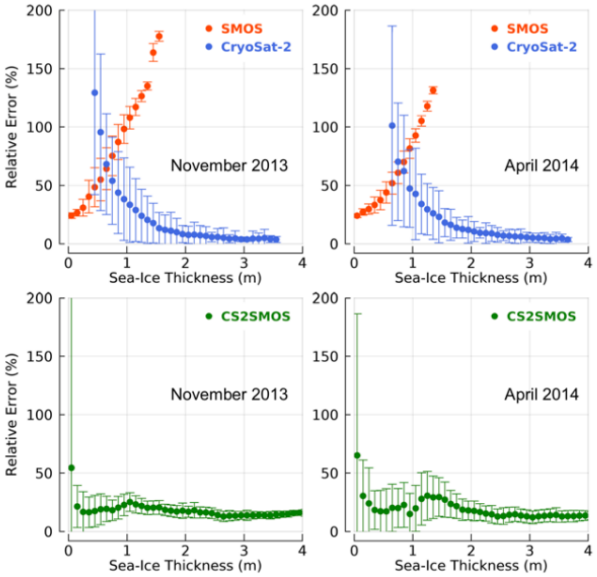

Figure 2.5: Binned relative error of CryoSat-2, SMOS and merged CS2SMOS *sea ice thickness* for an autumn and spring example. Taken from AWI [2021b] (Figure 1).

The output *analysis sea ice thickness* is available weekly for a October to April period. It is available Arctic-wide on a $25\,km$ EASE2 Grid with dimensions 432×432. Because of the complementary uncertainties of the merged products, the resulting *analysis sea ice thickness* has a small relative error throughout the thickness range (see figure 2.5). While FYI representation is improved heavily showing even small thickness gradients, problems with heavily deformed MYI are still present. The *analysis sea ice thickness* is validated with airborne electromagnetic thickness measurements from the Barents and Beaufort Sea [Ricker et al., 2017; AWI, 2021a,b].

The CryoSat-2/SMOS data is available from the Copernicus Climate Change Service (C3S) Climate Data Store (`https://cds.climate.copernicus.eu/`).

2.5 AMSR-E/2 Snow Depth

AMSR-E/2 *snow depth* (h_s) is a retrieval over FYI and MYI, using *brightness temperature* (Tb) at $6.9\,GHz$ and $18.7\,GHz$ and *sea ice concentration* (CI) from satellite based Advanced Microwave Scanning Radiometer (AMSR-E and AMSR2) [Rostosky et al., 2018].

The retrieval method assumes a relation between measured Tb and separate *snow depth* observations using regression coefficients. Firstly, Tb is calculated from the radiation emitted and reflected from the snow surface at $6.9\,GHz$ and $18.7\,GHz$. The Tb is depending on the chosen frequency and the snow and ice condition. The radiation is scattered on snow grains of certain size and in deep snow, which leads to reduced Tb. Liquid water content and density play analogue roles. Depending on frequency and temperature, radiation also interacts with the underlying sea ice. FYI can be distinguished from the snow cover at the given frequencies. Radiation at $19\,GHz$ passes through the uppermost layers of MYI and is scattered on air bubbles inside the upper layer MYI and the often rough surface [Rostosky et al., 2018].

Secondly, the gradient ratio (GR) is calculated using Tb, CI and correction factors k accounting for open water surfaces. In the following, only grid cells with $CI > 80\%$ will be used. Tb and $GR(19/7)$ are strongly influenced by the given conditions [Rostosky et al., 2018].

$$GR(19/7) = \frac{Tb_{19} - Tb_7 - k1(1 - CI)}{Tb_{19} - Tb_7 - k2(1 - CI)}$$

Linear regression is applied between GR and the training data set, for FYI and MYI separately. As training data set, Operation IceBridge (OIB) data from both airborne snow radar and in-situ measurements covering the spring months March and April, is used. The data covers the regions of Beaufort Sea, Central Arctic and Canadian Archipelago, and thus FYI (30%) and MYI (60%). With coefficients a, b of the regression and $GR(19/7)$, the snow depth h_s can be retrieved for FYI and MYI [Rostosky et al., 2018].

$$hs_{FYI/MYI}(cm) = a_{FYI/MYI} + b_{FYI/MYI} * GR(19/7)$$

Because of the interaction of snow and ice at used frequencies, the uncertainty of AMSR-E/2 *snow depth* is highest for deep snow over MYI. The average uncertainties are $0.1\,cm$ to $6\,cm$ for FYI and $3.4\,cm$ to $9.4\,cm$ for MYI. Comparison to the MOSAiC in-situ observations showed good agreement within a $5\,cm$ uncertainty [Krumpen et al., 2021]. Main sources of uncertainty are limited size of the training data and, to a smaller extent, the uncertainty of CI and regression coefficients. Uncertainty also derives from ice type identification, surface roughness and high spatial variability of *snow and ice thickness* in MYI regions [Rostosky et al., 2018]. Modelled uncertainties show, that *snow depth* retrieval from GR using microwave Tb is adequate and that uncertainty mainly results from variability in snow conditions and less due to MYI impact and the cloud free atmosphere [Rostosky et al., 2020]. AMSR-E/2 *snow depth* was validated using OIB data, that was excluded from the training data set. The validation showed 93% of the

errors being $< 5\,cm$ for FYI and 56% of the errors being $< 5\,cm$ for MYI, in spring. AMSR-E/2 *snow depth* is overall smaller than W99 snow climatology with differences of up to $10\,cm$ [Rostosky et al., 2018].

AMSR-E/2 *snow depth* is provided at a polar stereographic grid of size 448×304. The applicability is limited due to snow conditions, sensitivity of the chosen frequency and data available. Firstly, in early to mid winter, the snow cover is beginning to build up, being mostly freshly fallen, shallow and dry. In spring, the snow layers will have accumulated over the winter and have gone through metamorphosis, resulting in a snow pack with high depth, grain size and possibly also water content. Secondly, the used frequencies are not equally well applicable to these snow conditions. In contrast to spring metamorphosed snow, dry snow on MYI is almost invisible at $7\,GHz$ and only partly visible at $19\,GHz$, which lead to underestimation of early winter snow on MYI. Because of smaller grain size and smaller *snow depth*, overestimation of snow over FYI is likely in early winter. Because of this, and also deriving coefficients and validating for spring only, the product is not representative for all seasons, or for the entire Arctic [Rostosky et al., 2018].

2.6 AMSR/AVHRR Snow Depth

AMSR-AVHRR *snow depth* (h_s) is a monthly Arctic-wide product, using several different data sources, which will be described in the following [Lee et al., 2021].

Advanced Microwave Scanning Radiometer (AMSR-E and AMSR2) deliver passively measured *brightness temperature* (Tb), *snow ice interface temperature* ($SIIT$) and ice type for January to March, using $6.9\,GHz$, $10.7\,GHz$, $18.7\,GHz$ and $36.5\,GHz$ frequencies. Advanced Very High Resolution Radiometer (AVHRR) provides Tb at $3.7\mu m$, $10.8\mu m$ and $12.0\mu m$, which is translated into *snow top temperature* (STT), distributed by OSI-SAF. Satellite altimeters ICESAT and ICESAT-2 provide *total freeboard* (F_t), which is the distance from ocean surface to snow top on the Arctic ocean. *Sea ice concentration* (CI) is used from passively retrieved NOAA/ NSIDC Climate Data Record. Atmospheric data from ECMWF ERA5 reanalysis is used as model input, additionally. The AMSR-AVHRR *snow depth* (h_s) is provided on a $25\,km$ polar stereographic grid [Lee et al., 2021].

The method consists of two main parts: getting *total freeboard* from snow-ice scattering properties and relating *total freeboard* to snow-ice thickness ratio. Firstly, coastal and open water regions are rejected by cutting grid cells within a $100\,km$ range from any coast and grid cells with

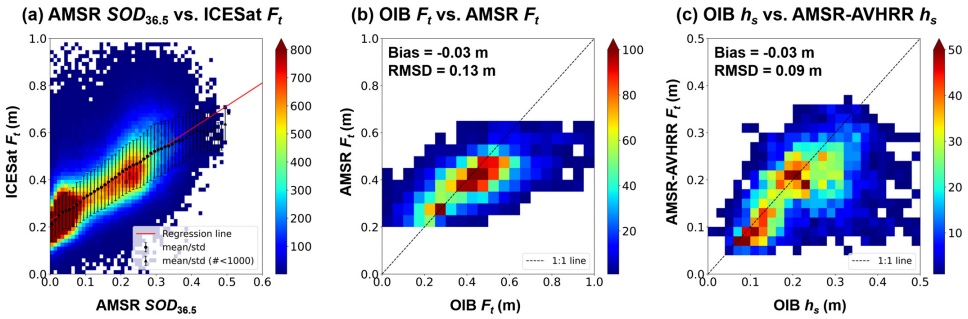

Figure 2.6: 2D histogram of (a) *snow-ice scattering optical depth SOD* derived from AMSR *brightness temperature* (Tb) and ICESat *total freeboard* (F_t) with regression and standard deviation. (b) *total freeboard* (F_t) from validation data set OIB and from using AMSR and ICESat. (c) *snow depth* (h_s) from validation OIB and AMSR-AVHRR end product. Bias and RMSE are given for (a)-(c). Taken from Lee et al. [2021] (Figure 1).

NOAA/NSIDC $CI > 98\%$. Secondly, AMSR top-of-atmosphere Tb is transferred to snow surface level accounting for atmosphere using simulations with input from ERA5. Thirdly, *snow ice scattering optical depth* (SOD) is derived using Tb in a sea ice radiative transfer equation. Now, regression of F_t (ICESat) and SOD (calculated with AMSR Tb) provides regression coefficients $c1$, $c2$ for finding analysis F_t [Lee et al., 2021]. The relation of AMSR SOD and ICESat F_t and the regression can be seen in figure 2.6.

$$F_{t,analysis} = c1 \cdot SOD + c2$$

Assuming a linear temperature profile within snow and ice layers and assuming continuous heat flux at snow-ice-interface, α is calculated from monthly averaged STT and $SIIT$ data. α is defined as the ratio of temperature differences within the snow layers ($STT - SIIT$) and ice layers ($SIIT - SST$). Now, h_s can be gathered, combining analysis F_t and α ratio. *Bulk densities* of water, ice and snow ρ_w, ρ_i and ρ_s are needed as well [Lee et al., 2021].

$$h_s = \frac{\alpha\rho_w}{\rho_w - \rho_i + \alpha(\rho_w - \rho_s)} F_{t,analysis}$$

Uncertainty is introduced by all the input parameters and sums up to a total of $8 - 10\,cm$. The main sources are α and F_t, while ρ contribute less. Operation Ice Bridge (OIB) snow radar and lidar data was used for validation and good agreement was found for F_t and h_s with -0.03 bias and RMSDs of $0.13\,m$ and $0.09\,m$. The comparison, of OIB F_t and h_s to analysis (AMSR and ICESat) F_t and AMSR-AVHRR h_s, is shown in figure 2.6, in more detail. In addition, AMSR-AVHRR h_s is 30% smaller, compared to modified W99, when halving W99 over FYI and applying a model also using ERA5 atmospheric data. Also, Lee et al. [2021] raises

awareness against possible biases occurring in snow depth and ice thickness products using OIB and W99 as part of the retrieval method. Reasons are that OIB is biased itself, W99 can not offer interannual information and snow conditions have changed since OIB campaign and W99 climatology years [Lee et al., 2021].

2.7 Methods

In this work, the MOSAiC winter time periods from 1.12.2019 0:00 to 26.2.2020 21:00 (ASFS30 at L2 and ASFS40 at L1) and 1.12.2019 0:00 to 22.1.2020 1:00 and 30.1.2020 0:00 to 5.2.2020 23:00 (ASFS50 at L3) are used. For a more detailed analysis of specific cases along the trajectory and the spatial analysis, the periods of early January (JAN: 31.12.2019 3:00 to 2.1.2020 4:00) and mid-February (FEB: 10.2.2020 5:00 to 17.2.2020 14:00), are used. For temporal means, the hours of 13.2.2020 15:00 to 14.2.2020 17:00 are excluded for February, because they do not represent clear sky conditions.

The used temporal resolution along the trajectory is hourly (full hour). For MOSAiC ASFS30-50, only full hour observations are used, matching the ERA5 availability. The ERA5 approximately $31 \times 31\,km$ grid cell closest to the L1-L3 trajectory is used.
For spatial analysis, MODIS and ERA5 have hourly mapped data, although some of the aggregated MODIS slices are empty, due to satellite and cloud coverage. *Snow depth* and *ice thickness* products are available with daily means (AMSR-E/2), weekly means (CryoSat-2/SMOS), and monthly means (AMSR-AVHRR). Daily means are averaged for the January and February period, while the closest weekly and monthly means are selected, e.g. February mean for mid-February period, even though the mean might cover more hours or none of the period days. For comparisons of mapped data, the natural grid of ERA5 (1440×240, $31\,km$), CryoSat-2/SMOS (432×432, $25\,km$), AMSR-E/2 and AMSR-AVHRR (448×304, $25\,km$) are projected on the higher resolution MODIS grid (1800×1400, $5\,km$).

The Polarstern winter trajectory, depicted in figure 2.1, is going in north-west direction from around $113°E$ $86°N$ (1.12.2019) to $40°E$ $88.5°N$ (26.2.2020) (see figure 2.7). Being distributed around Polarstern, the MOSAiC DN sites L1 to L3 have a mean distance of $10\,km$ (L2), $16\,km$ (L1) and $23\,km$ (L3) to the ship, and a distance of up to $30\,km$ from another. As all sites move with the sea ice drift and deformation, the relative position is approximately conserved. The following analysis mainly uses site L2, but all plots and calculation can be found for L1 and L3 in the appendix.

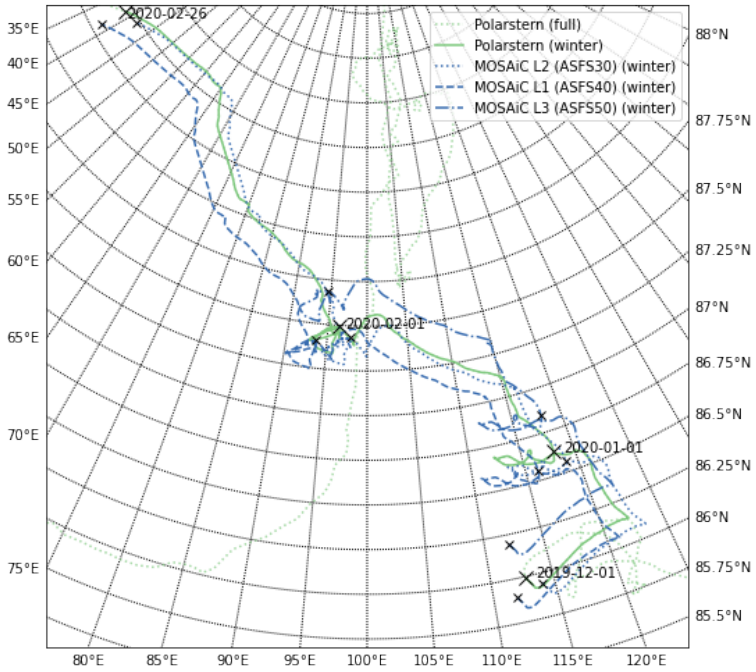

Figure 2.7: Trajectory of Polarstern ship (green, solid) and Distributed Network sites L1 (blue dashed), L2 (blue dotted) and L3 (blue dashed-dotted) from 1.12.2019 to 26.2.2020. The Polarstern trajectory was also plotted outside the December to February month (green dotted).

ERA5 LWU and MOSAiC LWN were not available directly and, thus, were calculated from the relation $LWN = LWD - LWU$. ERA5 *wind direction* and *wind speed* are calculated from $10\,m$ wind in u and v direction $(u10m, v10m)$ with

$$w_{sp} = \sqrt{u10m^2 + v10m^2} \tag{2.1}$$

$$w_{dir} = 180 + (180/\pi) \cdot \arctan(u10m, v10m) \tag{2.2}$$

Because the sea ice covered Arctic is analysed in this work, spatial ERA5 and MODIS IST and SKT are only used for areas with $CI_{ERA5} > 80\%$ or $IST_{MODIS} < -2°\mathrm{C}$.
The analysis of this work is carried out using Python 3 and standard statistical functions.

Chapter 3

Theory & Background

3.1 Energy Budget and Radiative States in the Arctic

3.1.1 Arctic Energy Budget

The Arctic energy budget, over snow and sea ice covered ocean, can be expressed by the *net short wave radiative flux* (SWN), *net long wave radiative flux* (LWN), *sensible heat flux* (HFs), *latent heat flux* (HFl) and *conductive heat flux* (HFc). A resulting total surface flux $F_{total} > 0$ represents energy gain of the system and, thus, warming, while $F_{total} < 0$ shows energy loss and cooling. All of the terms depend on the atmospheric condition and radiative state [Shupe et al., 2020a].

$$F_{total} = SWN + LWN + HFs + HFl + HFc \tag{3.1}$$

(adapted from Shupe et al. [2020a], Stramler et al. [2011])

In an Arctic winter domain without short wave solar radiation, long wave radiation is an important part of the surface energy budget. Hence, the focus will be set on the *net long wave radiative flux* (LWN), consisting of long wave radiation emitted downwards from the atmosphere (LWD) and radiated upwards from the surface (LWU). Radiation going into the surface, enhancing the surface budget, is defined positively and radiation emitted from the surface is defined negatively, as it decreases the total sum [Zhang et al., 1996; Shupe et al., 2020a].

$$LWN = LWD + LWU \tag{3.2}$$

(adapted from Zhang et al. [1996] Shupe et al. [2020a])

Surface downwelling long wave radiation (LWD) is dependent on the atmosphere's temperature, humidity and the presence of clouds [Stramler et al., 2011; Sedlar et al., 2021]. As winter storms transport warm, moist air and clouds into the Arctic, synoptic activity influences the LWD. Associated winds also affect the sea ice drift and upper ocean mixing. The LWD is also influenced by atmospheric patterns, like the Arctic Oscillation (AO) and Arctic Dipole (AD), as they are related with large scale temperature anomalies, wind patterns, storm activity and storm tracks [Cohen et al., 2017]. The influence of clouds is mainly defined by cloud coverage, height, temperature, water content and micro-physical properties [Zhang et al., 1996; Shupe et al., 2020a]. The downwelling radiation is not only influenced by, but also influences the near-surface and surface temperature and, thus, the LWU [Shupe et al., 2020a].
Surface upwelling long wave radiation (LWU) is dependent on the ocean temperature, ice and snow thickness and conductivity. In detail, it characterises the energy flow, from the warmer ocean, through the sea ice and snow cover, into the lower atmosphere [Shupe et al., 2020a].

In absence of large scale air mass advection, the surface energy budget determines the surface temperature. Thus, the surface temperature is an indicator for surface radiative fluxes and the radiative energy budget of the Arctic system over snow and ice-covered ocean. Assuming a snow emissivity of $\varepsilon_s = 0.99$ and σ as the Stefan-Boltzmann constant, the *surface skin temperature* (SKT) can be obtained.

$$SKT = [\frac{LWU - (1 - \varepsilon_s) \cdot LWD}{\varepsilon_s \cdot \sigma}]^{\frac{1}{4}} \tag{3.3}$$

(adapted from Walden et al. [2017]; Batrak and Müller [2019])

The *ice surface temperature* (IST) can be obtained using sea ice cover concentration CI and $LWU^{(ocean)}$ [Batrak and Müller, 2019]. If $CI = 100\%$, than SKT equals IST. If the analysed region encloses open water surfaces, IST should be used for analysing the temperature of the ice surface.

$$LWU^{(ocean)} = 0.98 \cdot \sigma \cdot 271.15\,K^4 \tag{3.4}$$

$$IST = [\frac{CI^{-1} \cdot (LWU - (1 - CI) \cdot LWU^{ocean}) - (1 - \varepsilon_s) \cdot LWD}{\varepsilon_s \cdot \sigma}]^{\frac{1}{4}} \tag{3.5}$$

(adapted from Batrak and Müller [2019])

The theoretical error of model or observational surface temperature (ΔT_s) can be derived dependent on the snow depth (h_s), ice thickness (h_i) and their errors $\Delta hs, \Delta hi$. Fix values are assumed for the ocean temperature

$T_o = 271.15K$ and the ice and snow conductivity $k_s = 0.31\,Wm^{-1}K{-}1$, $k_i = 2.1\,Wm^{-1}K{-}1$ [Batrak and Müller, 2019].

$$\alpha = \frac{k_i \cdot k_s}{k_s \cdot h_i + k_i \cdot h_s} \tag{3.6}$$

$$\alpha' = \frac{k_i \cdot k_s}{k_s \cdot (h_i + \Delta h_i) + k_i \cdot (h_s + \Delta h_s)} \tag{3.7}$$

$$\Delta T_s = \frac{(\alpha' - \alpha)(T_s[K] - T_o[K])}{4 \cdot \varepsilon \cdot \sigma \cdot T_s[K]^3 - \alpha'} \tag{3.8}$$

[Batrak and Müller, 2019]

3.1.2 The Two Arctic Winter Atmospheric Radiative States

Two main radiative states of the Arctic winter atmosphere can be observed and categorised by the surface energy budget [Stramler et al., 2011]. These states are present throughout the troposphere and stratosphere and can even be observed in subsurface layers, such as the ocean mixed layer, sea ice and snow layers [Stramler et al., 2011]. These states are driven by synoptic activity, that cause anomalies in temperature and humidity, and large scale atmospheric circulation patterns, influencing wind patterns and storm tracks, in addition [Stramler et al., 2011; Cohen et al., 2017]. The bimodal nature of the winter Arctic atmosphere can be seen in the frequency distributions of various related variables, such as near surface and surface temperature and long wave radiation [Stramler et al., 2011]. Related to climate change, the frequency of occurrence for the two preferable atmospheric states is evolving in the evolving Arctic system [Graham et al., 2017]. The change of the system from one into the other radiative state is called transition [Stramler et al., 2011].

Radiatively Clear State

The radiatively clear state is connected to winter calm periods, it lasts from days up to two weeks and can be seen as background state [Kayser et al., 2017; Stramler et al., 2011].

The clear state mainly occurs in the high pressure phases of baroclinic waves ($> 1020hPa$) [Kayser et al., 2017; Stramler et al., 2011]. Although ice phase clouds can occur in these ridges, their optical thickness is too small and the cloud bases are too high to contribute to the surface radiation budget [Stramler et al., 2011; Shupe et al., 2020a]. Without optically thick clouds, the *downwelling long wave radiation* at the surface is considerably small, while energy is still radiated upwards from the surface, which leads to a surface energy deficit. As a result, surface and near-surface temperatures are very low. In this synoptic state, wind speed is mostly low [Graham et al.,

2017; Shupe et al., 2020a]. Due to this calm and cold conditions the lower troposphere is stable and a strong surface based temperature inversion is present [Walden et al., 2017].
Subsurface gradients are linear and steep through ice and snow, resulting in heat being conducted through ice and snow and escaping into the atmosphere [Stramler et al., 2011]. As a result, there is an imbalance and a large energy flux at the surface, while there is near-equilibrium at the ice-snow interface [Stramler et al., 2011; Graham et al., 2017].

Opaquely Cloudy State

The opaquely cloudy state mainly appears in phases of storms and synoptic activity and can be seen as perturbation from the background clear state [Kayser et al., 2017].

Caused by cyclonic events during low pressure phases of baroclinic waves (trough), the cloudy state lasts from days to 10 days, but longer than the cyclone itself [Kayser et al., 2017; Stramler et al., 2011]. Heat and moisture transport by the cyclones causes a rapid and strong temperature increase at start of opaque periods, followed by a phase of consistently warmer temperatures [Cohen et al., 2017; Graham et al., 2017]. Resulting from a sufficient supply of moisture and warm temperatures, liquid and mixed phase clouds are present, which further increases the LWD, and thus the surface temperature and LWU [Kayser et al., 2017]. Advection of moisture and clouds and related winds decrease the stability, resulting in an unstable lower troposphere [Walden et al., 2017; Cohen et al., 2017]. Thus, there is no surface based inversion, but a surface mixed layer, limited by inversion on top [Kayser et al., 2017; Stramler et al., 2011]. The opaquely cloudy state can occasionally occur in high pressure due to drifting clouds and after frontal passages [Stramler et al., 2011].
Subsurface gradients of snow and ice are different, which causes a temperature difference at the snow-ice interface, a disequilibrium [Stramler et al., 2011]. In contrast, the surface is in near-equilibrium with net-zero energy flux [Stramler et al., 2011; Graham et al., 2017]. The strengthened winds also cause sea ice drift and upper ocean mixing, influencing the surface and subsurface layers once again [Cohen et al., 2017].

3.2 Previous Expeditions and Comparison to ERA5 Reanalysis

3.2.1 Previous Expeditions and their Representativeness

As the Arctic is remote and difficult to access, its characteristics have been unknown for long and even nowadays, in-situ measurements are rare, espe-

cially for winter. Ship based expeditions in the Arctic sea ice offer a platform for a wide range of observations and, thus, numerous expeditions were carried out during the last 130 years. An example for early polar exploration took place in the late 19th century. Under Fridtjof Nansen, the ship Fram drifted across the Arctic with the natural movements of the ice from the New Siberian Islands, through the Central Arctic, towards Svalbard. Even though it did not reach the North Pole, it gathered a lot of, entirely new, information about the sea-ice-covered Arctic [Uttal et al., 2002].

An important field expedition in the time of modern measurements, was carried out from October 1997 to October 1998, drifting the ship *Des Groseillers* in the thick sea ice of the Canadian Basin north-east of Alaskan Prudhoe Bay, through the Beaufort Sea, to the Chukchi Cap. The Surface Heat Budget of the Arctic Ocean (SHEBA) expedition offered a platform for interdisciplinary study of the physical processes around the Arctic energy budget and ice mass balance. It already spotted the influence of climate change in the Arctic [Uttal et al., 2002]. During the SHEBA winter, due to above average synoptic high pressure occurrence, the near surface air temperature was below average [Graham et al., 2017].

The recent decade Norwegian Young Sea Ice (N-ICE2015) expedition was carried out from January 2015 to June 2015 [Cohen et al., 2017]. The covered region north of Svalbard was characterised by young, thin sea ice, that dominates the ice covered Arctic nowadays [Cohen et al., 2017]. During the expedition, observations of the atmosphere, ocean, cryosphere and biosphere were gathered simultaneously, to understand the new Arctic system with its components and interaction of components [Kayser et al., 2017]. During January and February 2015, above average cyclone activity, related to a positive phase of the Arctic Oscillation, and a thick snow cover were observed. The measured temperature maxima around the melting point are not exceptional for the Atlantic Sector of the Arctic [Graham et al., 2017].

The latest and most extensive expeditions in the Arctic sea ice has been the 2019 to 2020 MOSAiC expedition, covering multiple aspects of the Arctic system, spatial and temporal scales [Barber et al., 2020; Shupe et al., 2020b] (see detailed description in section 2.2).

Even though expeditions help to understand the Arctic system components and their relation in their specific setting, the findings might not be valid in the entire Arctic, for all seasons and years with different synoptic activity [Graham et al., 2017]. The SHEBA winter might not be representative for regimes with thin ice cover and, thus, for large parts of the nowadays state of the Arctic [Kayser et al., 2017; Graham et al., 2017]. It might also not be representative for regions with high synoptic activity, such as the At-

lantic Sector. Vice versa, the N-ICE winter might not be representative for the wider MYI Arctic context or for lower synoptic activity [Graham et al., 2017]. Because of the differences, rather different climate change trends were observed during the two expeditions, supporting the idea of heterogeneous climate change in the Arctic [Graham et al., 2017].
Despite their contrasting settings, the expeditions also show similarities, in e.g. tropospheric structure [Kayser et al., 2017]. Thus, their difference might allow conclusions for a pan-Arctic context. The two preferable radiative states of the winter Arctic atmosphere could be observed in both N-ICE and SHEBA [Graham et al., 2017]. Because of the applicability of the radiative states onto the fundamentally different settings, it was concluded, that the bimodal nature of the winter atmosphere might be valid for the entire Arctic Basin regardless of the ice thickness, the regional weather regimes and meteorological conditions [Graham et al., 2017]. Supporting this idea, the variability between the two states is greater than the large geographical variability of temperature and humidity characteristics [Stramler et al., 2011; Graham et al., 2017]. Still, given the regional and temporal differences, the states can be pronounced differently in strength and character, as in the comparison of the SHEBA and N-ICE drifts [Graham et al., 2017]. Differences might be visible in the variable range, frequencies of occurrence and variable values of the frequencies. Following, an application of the two radiative state theory onto the MOSAiC expedition seems reasonable, even though previously used criteria for categorisation may need adaption. In the first part of the analysis of this work, the applicability of the two states theory will be analysed for MOSAiC and the two states will be applied on the MOSAiC winter drift. Further, it will be analysed if the ERA5 reanalysis can reproduce the two states.

3.2.2 Comparison of ERA5 to Expedition Data

Given the applicability and importance of the bimodal nature of the winter Arctic atmosphere, we would expect that Arctic weather, climate models and reanalyses, should be able to represent these states of the atmosphere and subsurface with their frequency of occurrence [Stramler et al., 2011].

Despite the importance, models have problems simulating the states and, thus, the energy budget [Kayser et al., 2017]. Difficulties can occur due to incorrect simulation of the boundary layer and surface based inversions [Kayser et al., 2017; Graham et al., 2017]. Also, models tend to refuse liquid water under low temperature conditions and, thus, underrate the liquid water content of clouds [Graham et al., 2017]. The modelled surface energy budget is also largely influenced by the modelled sea ice and snow characteristics [Graham et al., 2017].
Batrak and Müller [2019] analysed the warm bias of winter Arctic clear sky

periods for several reanalyses and weather forecast models, by using the N-ICE winter observations and a pan-Arctic satellite data set for 2015 to 2017. They found a $5\,K$ to $10\,K$ warm bias for most of the reanalysis and forecasts systems. Most of the models showed a warm bias in all observed surface temperatures under $-25°$C. In a pan-Arctic comparison, highest temperature errors often were found, where the surface temperatures were lowest. The main reason is the missing or unrealistic snow representation in most of the models. It causes too high ocean-to-atmosphere conductive heat flux and thus LWU errors of $+20\,Wm^{-2}$ to $+30\,Wm^{-2}$ and consequently, too high surface temperatures. Because snow insulates seven times more effective than sea ice, even a relatively thin snow layer (in the order of $10\,cm$) has a significant impact on the surface temperatures. Surface temperature errors are largest where snow thickness are large. Where the snow layer is thin, errors in ice thickness are becoming highly relevant. The ERA5 reanalysis showed these characteristics, including a warm bias throughout all the N-ICE winter clear sky periods and the entire ice covered Arctic, in a spatial context. Batrak and Müller [2019] also pointed out the importance of simulating the clear sky conditions correctly. Not captured clear conditions, led to the highest temperatures biases of up to $15\,K$ in ERA5 and other ECMWF reanalysis. Still, in correctly resolved clear sky conditions, due to simulating low LWD correctly, a warm bias of up to $+7\,K$ was found for ERA5 [Batrak and Müller, 2019].
Consistent with Batrak and Müller [2019], Krumpen et al. [2021] found a $2\,K$ to $3\,K$ warm bias for ERA5 simulations along the MOSAiC trajectory. These findings will be analysed further for winter clear sky periods, in this work.

3.3 Conditions of Sea Ice, Snow and Atmosphere during Arctic Winter

3.3.1 Arctic Winter Conditions and Changes of the last Decades

Sea Ice Conditions

Sea ice is a fragile and critical part of the Arctic system, influencing the energy budget and the atmosphere to a large extent. The seasonal cycle is characterised by sea ice formation and growth in autumn and winter and sea ice melt during spring and summer. Because of climate change, the sea ice extent and thickness is decreasing rapidly from year to year [Perovich et al., 2020].

Mean 1981 to 2010 *sea ice extent* covers the Arctic Basin, coastal North Canada, Alaska and Russia at seasonal maximum in March (see figure 3.1).

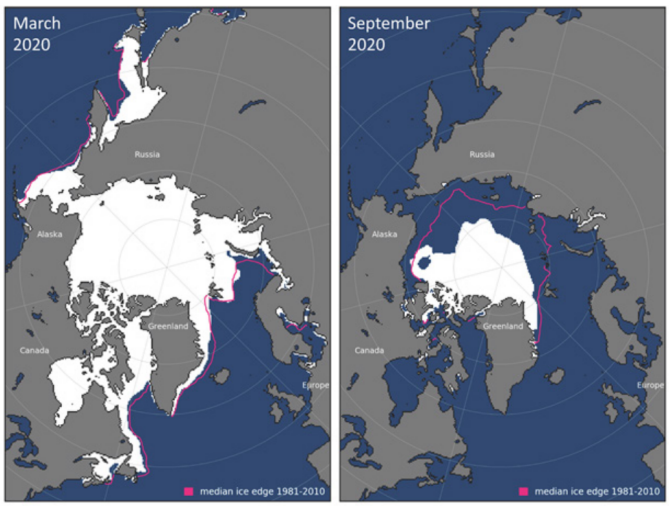

Figure 3.1: Mean *sea ice extent* for March 2020 (left) and September 2020 (right), representative for the yearly maximum and minimum sea ice extent, compared to the median sea ice edges from 1981 to 2010 climatology (purple lines). Taken from Perovich et al. [2020] (Figure 1).

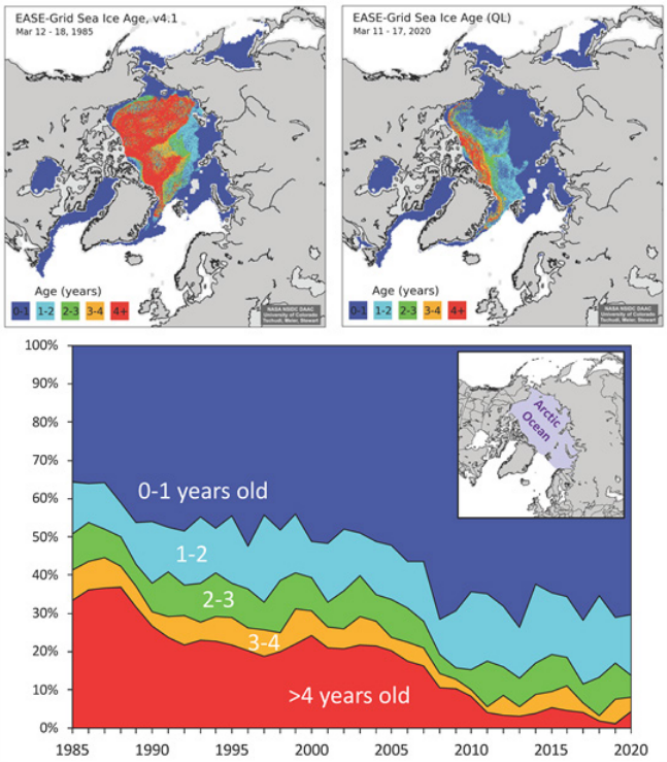

Figure 3.2: March sea ice age maps for 1985 (upper left) and 2020 (upper right). Time series of sea ice age coverage percentages for the Arctic Ocean from 1985 to 2020. Taken from Perovich et al. [2020] (Figure 3).

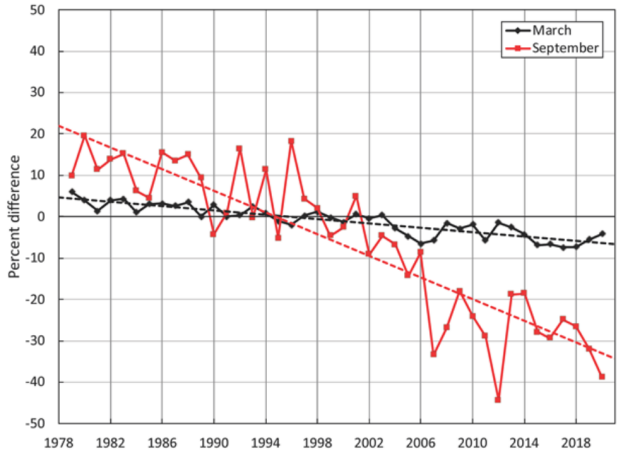

Figure 3.3: 1978 to 2020 March (black) and September (red) mean *sea ice extent* percentage of difference relative to the 1981-2010 mean and linear trends (dashed lines). Taken from Perovich et al. [2020](Figure 2).

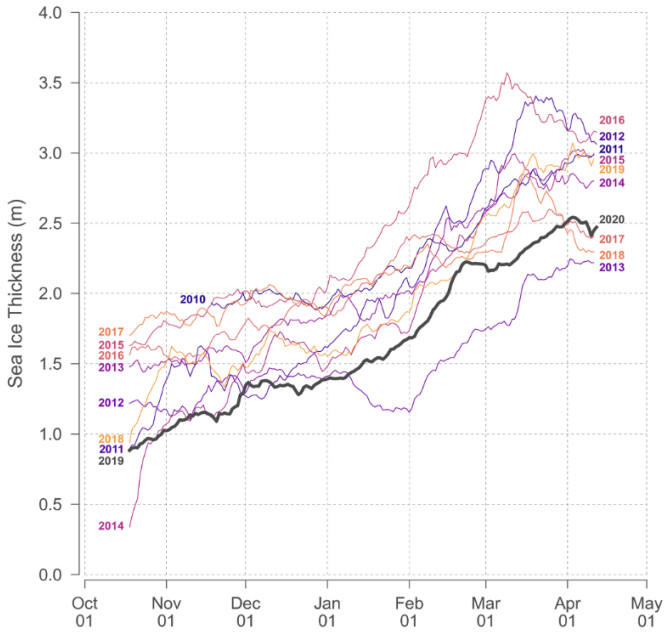

Figure 3.4: October to May *sea ice thickness* growth within a 50 km radius around the MOSAIC trajectory for the years 2010 to 2020 using CryoSat-2/SMOS. Taken from Krumpen et al. [2021] (Figure 13).

At mean minimum seasonal extent in September, the Arctic Basin is not entirely ice covered (figure 3.1). Over the last 40 years the March (maximum) *sea ice extent* decreased with a rate of -2.5% per decade, while the September (minimum) extent decreased even more rapidly with -13.1% per decade, which can also be seen in the 2020 minimum and maximum *sea ice extent* (see figure 3.1,3.3) [Perovich et al., 2020].

Sea ice thickness increases in average by $1.5\,m$ during the autumn to spring growth period of the years 2010 to 2020, but still decreases from year-yo-year (see figure 3.4). Minimum and maximum *sea ice extent* and *sea ice thickness* are highly variable from year-to-year (see figure 3.3,3.4) [Perovich et al., 2020; Krumpen et al., 2021].

Because sea ice thickens with time, its age is directly related to its thickness. In 1985 more than 50% of the ice was MYI, of which 41% was $\geq 3\,years$ and 34% $\geq 4\,years$ old (see figure 3.2). In 1985 MYI ice was present from the Siberian coast, through the Central Arctic, to the north coasts of North America and Greenland. Since then, the amount of old ice decreased and first and second year ice becomes more and more dominating. Again, a high year-to-year variability can be seen. In 2010, less than 30% remain as MYI and since 2010, the rate of old ice loss has stagnated (see figure 3.2) [Perovich et al., 2020].

Snow Conditions

Snow is a an important component of the Arctic system, dampening the ocean to atmosphere energy flux more efficiently than sea ice, influencing the ice-mass balance and controlling the surface's reflectivity. Thus, even small differences in snow depth can cause large changes in the surface energy budget [Overland and Guest, 1991; Webster et al., 2018]. On the one hand, snow is difficult to measure. On the other hand, snow can be highly variable in space, making in-situ measurements unrepresentative for a spacial distribution on their own. Remote sensed snow depth covers the entire Arctic at a high frequency, but is highly error prone and uncertain. Thus, snow depth values from multiple sources need to be assessed, in order to better understand its impact and representation in models.

Figure 3.6 shows the mean January to March spatial distribution of *snow depth* (h_s) for the modified W99 (2003-2020) climatology and for the AMSR/AVHRR *snow depth* retrieval, that is described in Lee et al. [2021] and used in this work. Highest snow depth of $28\,cm$ to $30\,cm$ (mW99) and $24\,cm$ to $27\,cm$ (AMSR/AVHRR) can be seen north of Greenland and the Canadian Archipelago, within 85% MYI frequency (see figure 3.6). The *snow depth* decreases towards lower latitudes and away from Greenland and

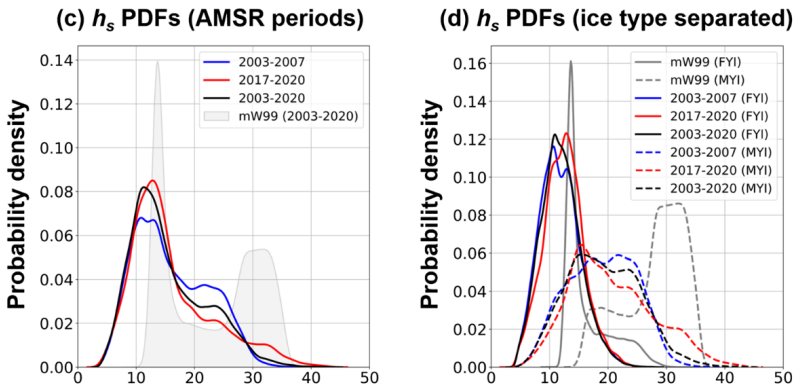

Figure 3.5: *Snow depth* (h_s) probability density distribution using the method described in Lee et al. [2021] for AMSR/AVHRR data for the years 2003-2007, 2017-2020 and 2003-2020 and the modified W99 climatology for the years 2003-2020 (left). Snow depth probability density distribution as in the left figure, but separated for FYI and MYI (right). Taken from Lee et al. [2021] (Figure 3c,d).

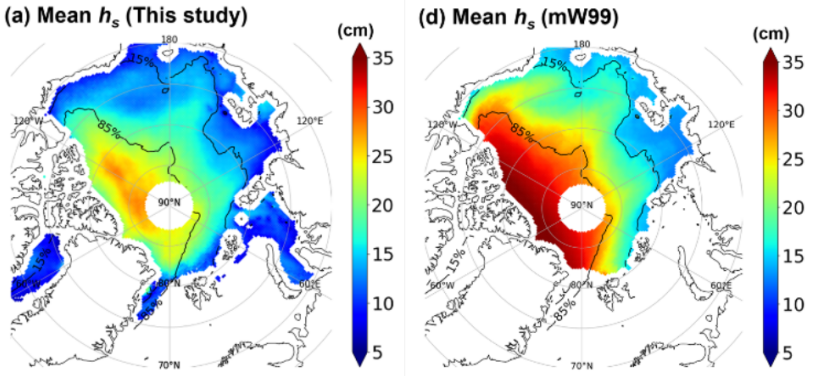

Figure 3.6: Mean *snow depth* (h_s) using the method described in Lee et al. [2021] for AMSR/AVHRR data (left) and using the modified W99 climatology (right) for the years 2003-2020. Adapted from Lee et al. [2021](Figure 2a,d).

the North American continent. Snow on MYI is deeper and appears frequently on a range of 14 cm to 24 cm (AMSR/AVHRR) and 27 cm to 36 cm (mW99) (see figure 3.5). *Snow depth* on FYI is smaller and most frequently around 13 cm to 14 cm deep for mW99 and AMSR/AVHRR [Lee et al., 2021].

The seasonal cycle of *snow depth* mainly consists of snow accumulation and increasing depth during autumn and winter. Metamorphosis in late winter and spring is followed by melt in summer [Rostosky et al., 2018]. With a changing Arctic, the regional patterns of *snow depth* and the pan-Arctic snow volume is changing. Because the fraction of FYI increases, the mean Arctic snow depth decreases, despite deepening snow on MYI [Lee et al., 2021].

Atmospheric Conditions

The atmospheric temperature governs the Arctic sea ice melt and growth, which again influences all parts of the Arctic system. The Arctic atmospheric state is driven by solar radiation and heat flux from the open ocean in summer. In winter, the snow-and-ice-covered ocean to atmosphere energy flow, as well as the warm air and moisture transport due to storms, is defining. Thus, conditions of ice and snow and cloud occurrence are critical. Because the cloud, ice and snow cover is highly variable in space, local and regional differences can be high. Since clouds are also highly variable in time, rapid changes can occur.

Representative for seasonal cycle of the Central Arctic, monthly mean 1979-2019 near surface meteorological variables from the MOSAiC trajectory are depicted in figure 3.9. Missing solar radiation in winter causes a mostly negative surface radiative energy budget of $-50\,W/m^2$ to $-20\,W/m^2$ (min. $-75\,W/m^2$, max. $+20\,W/m^2$), low near surface air temperatures of -28°C to -19°C (min. -38°C, max. 0°C) and low atmospheric water vapour content around $2.5\,kg/m^2$ (see figure 3.9). Winter storms can cause a positive radiative energy budget and can raise the *2m air temperature* up to melting point. *Mean sea level pressure* and *wind speed* means are relatively constant during the year, while variable ranges are widest in winter with 960 hPa to 1060 hPa and up to average 20 m/s) (see figure 3.9). Mean *wind directions* range from south-west to easterly (see figure 3.7). An increase of opaquely cloudy days, according to the preferable atmospheric states, can be observed in the Greenland Sea, the western Central Arctic, but mostly, at the ice edge of the Atlantic Sector [Graham et al., 2017].

In contrast, continuous solar radiation in summer causes high net radiation of $60\,W/m^2$ to $100\,W/m^2$ (min. $40\,W/m^2$, max. $220\,W/m^2$) and thus, high temperatures around 0°C and water vapour content of up to $30\,kg/m^2$.

Because of winter storms, in the seasonal cycle of variable value ranges, temperature, *air pressure* and *wind speed* have the widest distribution in winter and the smallest range in summer. Water vapour and net radiation ranges are widest in summer and smallest in winter (see figure 3.9).

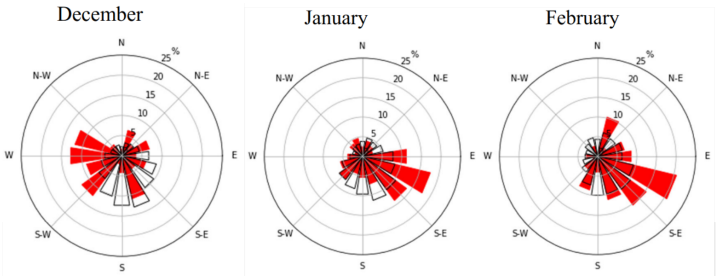

Figure 3.7: Monthly *wind direction* in MOSAIC year (red) and the 1979-2019 climatology (black outlines) using ERA5 reanalysis. Adapted from Rinke et al. [2021] (Figure S6).

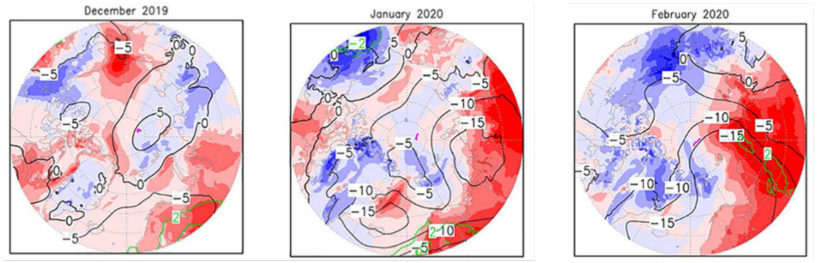

Figure 3.8: Monthly mean anomaly of *2m air temperature* (colours), *mean sea level pressure* (black lines) and *total column water vapour* (green lines). ERA5 for the MOSAIC year and the 1981-2019 climatology. The MOSAiC trajectory is marked for every month (purple lines). Adapted from Rinke et al. [2021] (Figure 5).

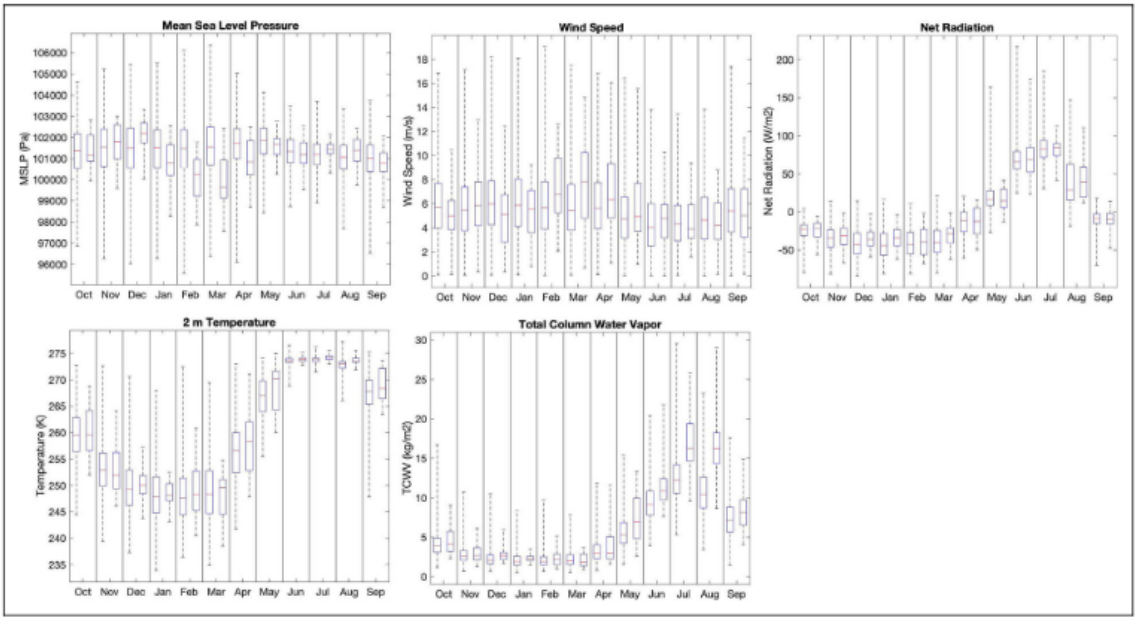

Figure 3.9: Monthly near surface meteorological variables along the MOSAiC trajectory for the ERA5 1979-2019 climatology (left monthly boxes) and ERA5 during the MOSAiC year (right monthly boxes). For all variables *mean sea level pressure*, *wind speed*, *net short- and long wave radiation*, *2m temperature* and *total column water vapour*, the monthly median (red), Interquartile range (IQR) with 25th to 75th percentile (box), minimum and maximum (whiskers) are shown. Taken from Rinke et al. [2021] (Figure 4).

3.3.2 Conditions in MOSAiC Winter 2019/2020

The MOSAiC winter 2019/20 was characterised by initially thin and dynamic sea ice, average snow conditions and average atmospheric conditions for large part of the winter, interrupted by short time anomalous storm events [Shupe et al., 2020b; Krumpen et al., 2021; Rinke et al., 2021].

Sea Ice in Winter 2019/20

Warm *sea surface temperature* (SST) caused a low minimum *sea ice extent* in late summer 2019 and hindered the freezing process in autumn 2019 [Perovich et al., 2020].

Due to stronger dynamic and thermodynamic ice growth and formation likely caused by autumn atmospheric and ocean (SST) conditions, the *sea ice thickness* around the MOSAiC trajectory increased from $0.77\,m$ in October 2019 to $2.4\,m$ in April 2020 (see figure 3.4). In more detail, at the MOSAiC Central Observatory and Distributed Network *ice thicknesses* of

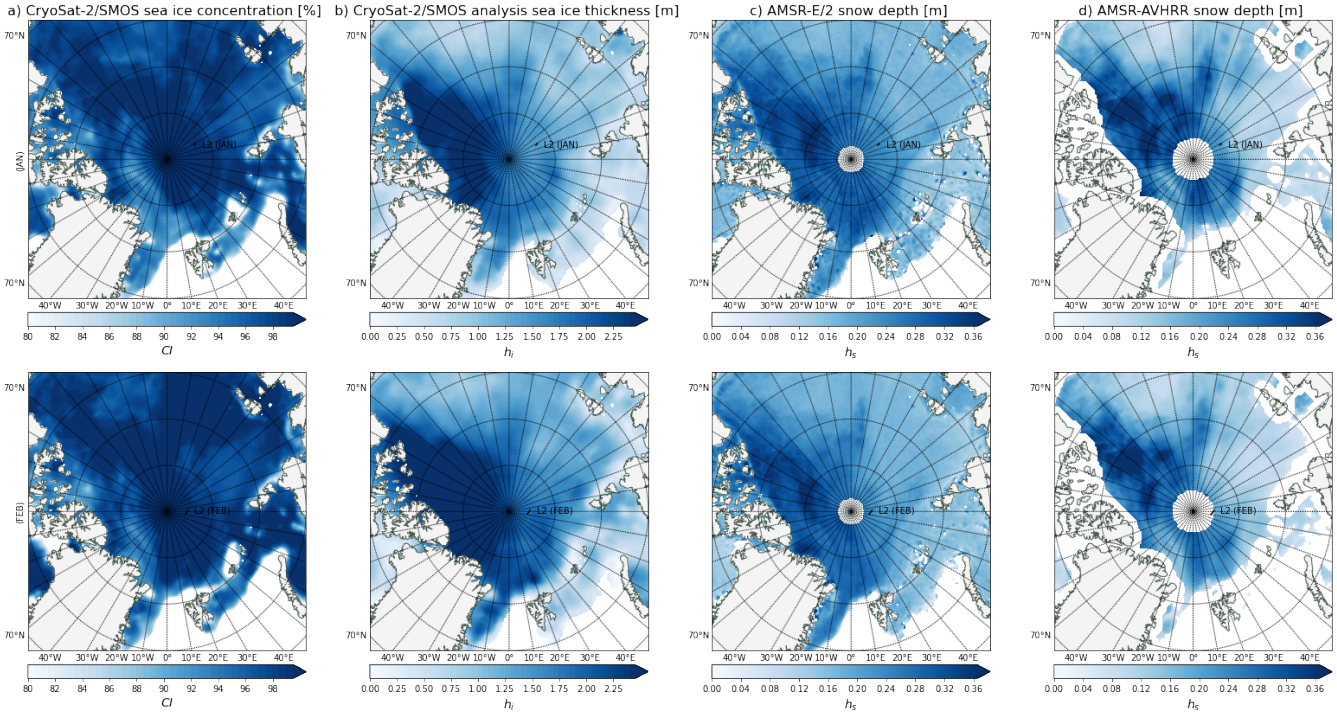

Figure 3.10: Satellite derived pan-Arctic snow and sea ice observations for the clear sky periods in early January (31.12.2019 3:00 - 2.1.2020 4:00) (top row) and mid-February (10.2.2020 5:00 - 17.2.2020 14:00) (bottom row): a) CryoSat-2/SMOS *sea ice concentration* (CI) [%], b) CryoSat-2/SMOS *sea ice thickness* (h_i) [m], c) AMSR-E/2 *snow depth* (h_s) [m], AMSR/AVHRR *snow depth* (h_s) [m]. Temporal means are January and February monthly means (AMSR-E/2), weekly mean(s) closest to the chosen periods (CryoSat-2/SMOS) and period average of daily means (AMSR/AVHRR). The derival methods and products are described in section 2.4-2.6. The MOSAiC trajectory was added for each period (black line).

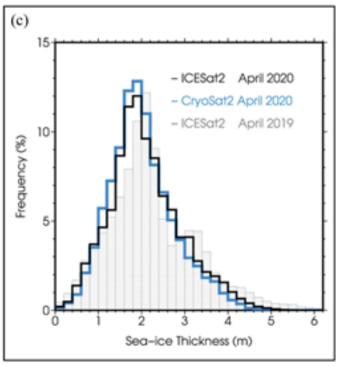

Figure 3.11: Arctic *sea ice thickness* frequency in April 2020 for ICESat2 and CryoSat-2 and April 2019 for ICESAT2. Taken from Perovich et al. [2020] (Figure 4c).

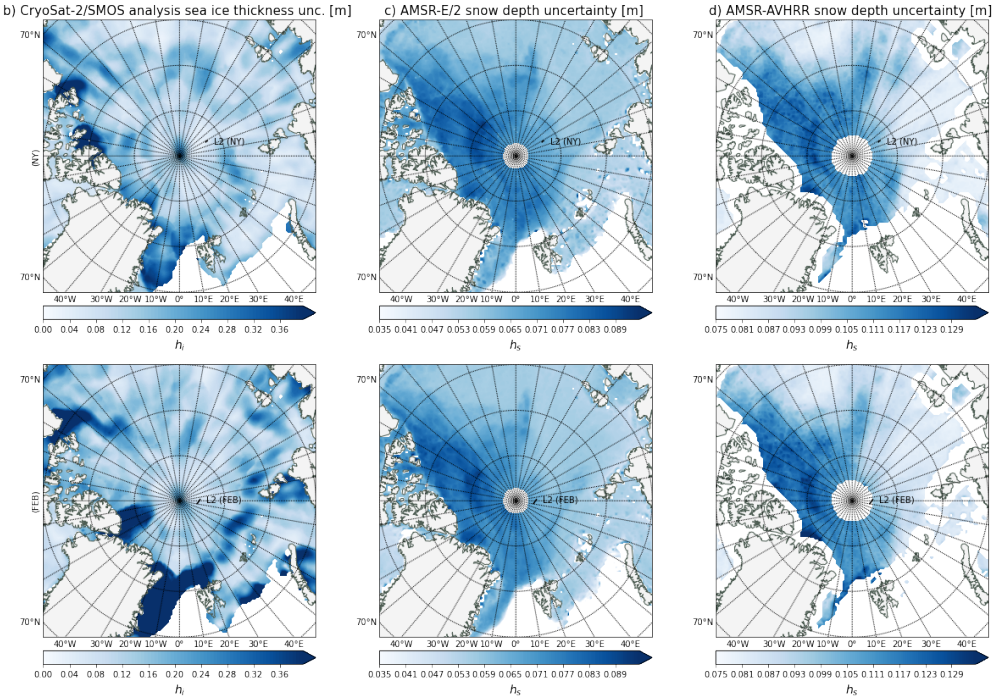

Figure 3.12: Uncertainties of satellite derived pan-Arctic snow and sea-ice observations for the clear sky periods in early January (31.12.2019 3:00 - 2.1.2020 4:00) (top row) and mid-February (10.2.2020 5:00 - 17.2.2020 14:00) (bottom row): b) CryoSat-2/SMOS *sea ice thickness* (h_i) [m], c) AMSR-E/2 *snow depth* (h_s) [m], AMSR/AVHRR *snow depth* (h_s) [m]. The temporal means are January and February monthly means (AMSR-E/2), weekly mean(s) closest to the chosen periods (CryoSat-2/SMOS) and period average of daily means (AMSR/AVHRR). The derival methods and products are described in section 2.4-2.6. The MOSAiC trajectory was added for each period (black line).

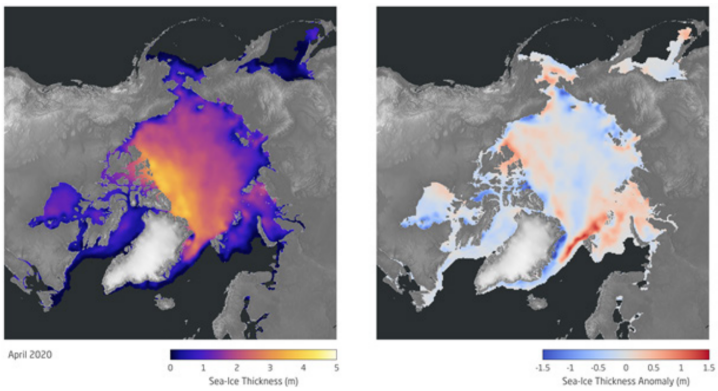

Figure 3.13: April 2020 Arctic *sea ice thickness* (left) and thickness anomaly from the recent decade 2011-2019 mean using CryoSat-2/SMOS (right). Taken from Perovich et al. [2020] (Figure 5).

$1.26\,m - 1.35\,m$ (December), $1.46\,m - 1.51\,m$ (January) and $1.9\,m - 2\,m$ (February) were observed. It is to mention, that the MOSAiC central sites were deployed at a regional *ice thickness* minimum, which decreased difference from the surrounding areas with ice growth [Krumpen et al., 2021].
In a pan-Arctic context, thickest ice with $h_i \geq 2\,m$ can be seen in between the North American continent, Greenland and the North Pole, from $20°W$ to $140°W$ for January and February example periods (see figure 3.10). Sea ice between $h_i = 2\,m$ and $0.8\,m$ can be seen in the Russian Arctic Basin, European Arctic Basin and Greenland Sea. The *ice thickness* decreases towards the Siberian coast, Alaskan coast and the Atlantic, though the regional variability can be high. Generally, a winter ice thickening of at least $0.2\,m - 0.4\,m$ and westward drift of thin and thick ice is visible from early January to February (see figure 3.10). As described in section 2.4, the CryoSat-2/SMOS *ice thickness* product has low errors for large parts of the thickness range, but still contains multiple error sources. Thus, the *ice thickness* uncertainty is $0\,m - 0.25\,m$ for most of the regions, which can be as large as $0.99\,m$ regionally (see figure 3.12).
In April 2020, below mean *ice thickness* could be observed in the Central Arctic, by the Russian Continental Shelf, in some parts of the Canadian Archipelago, coastal Greenland and Alaska (see figure 3.13). Above mean ice thickness was observed in the Beaufort Sea, Barents Sea and north of the Canadian Archipelago (see figure 3.13). Thicker ice north of Svalbard and in the Fram Strait was caused by enhanced ice drift speed and thus advection of thick ice which also caused faster drift for the MOSAiC expedition. Despite the enhanced regional growth, there was a slight Arctic sea ice loss in the period from April 2019 to April 2020 [Perovich et al., 2020]. Enhanced thermodynamic growth and ice dynamics also caused a wider distribution of ice thicknesses, centred around $1.8\,m$ in April 2020 (see figure 3.11) [Krumpen et al., 2021; Perovich et al., 2020].

Only 3.7% of the Arctic Ocean sea ice was $2 - 4\,years$ old in 2020. The oldest ice is located along the northern coasts of Alaska, the Canadian Archipelago, Greenland and in the Fram Strait (see figure 3.2) [Perovich et al., 2020].
Sea ice extent is decreasing annually by 32% for September 2019 (yearly minimum) and by 4% for March 2020 (yearly maximum) (see figure 3.3). Consequently, March 2020 sea ice extent is slightly smaller than the 1981 to 2010 climatology (see figure 3.1) [Perovich et al., 2020].

The sea ice concentration was slightly above average along the MOSAiC track with 97% to 99% and very little variability, which could be observed at the MOSAiC site and from remote sensing. In the end of February, the concentration dropped to 95% [Krumpen et al., 2021]. The ice concentration is not homogeneous and areas of very high $CI > 98\%$ can be found all over

the Arctic, e.g. the Central Arctic including the North American, Russian and European Basin, and the Kara Sea. Lower $CI < 95\%$ are not only present at the ice edges, but also in the Greenland Basin and North of the Canadian Archipelago and even lower $CI < 80\%$ e.g. around Severnaya Zemlya and Franz-Josef-Land. In addition, an increase of CI and high CI areas can be seen from early January to mid-February (see figure 3.10).

Snow in Winter 2019/20

Snow conditions during 2019/20 winter were close to the climatological mean [Perovich et al., 2020]. The March *snow depth* at the MOSAiC site was around $22\,cm$ with a deviation of $3\,cm$ to the climatology and a climatological average uncertainty of $5\,cm$ [Krumpen et al., 2021]. In an Arctic context, highest snow cover $h_s \geq 30\,cm$ is observed on MYI, while *snow depth* decreases towards Chukchi Sea and Russia. There is also a January to February increase (see figure 3.10).
For the assessment of the pan-Arctic *snow depth* distribution, the two satellite products AMSR-E/2 [Rostosky et al., 2018] and AMSR/AVHRR [Lee et al., 2021] are used, which are described in section 2. Even though the products are derived with different methods and assumptions, they cover slightly different time periods, and there are differences in the local *snow depth*, they show consistent patterns. AMSR/AVHRR has a slightly smaller maximum h_s, but shows highest h_s on larger scales, whereas AMSR-E/2 has shows larger depths of small h_s (see figure 3.10). The uncertainties are estimated to range from $0\,cm - 9.8\,cm$ (AMSR-E/2) and $10\,cm - 14.8\,cm$ (AMSR/AVHRR) and are highest for large snow depths on MYI (see figure 3.12). For the MOSAiC track a uncertainty of $8\,cm$, was derived [Krumpen et al., 2021].

Atmosphere in Winter 2019/20

The meteorological conditions during the winter 2019/20 were average compared to the climatology 30% to 60% of the time and despite extremely anomalous events, also inside the previous 40 years climatology range [Rinke et al., 2021]. Furthermore, in autumn 2019, warmer SST caused warmer air temperatures over the Arctic Ocean [Ballinger et al., 2020]. Circulation anomalies caused westwards, rather than northwards winds [Krumpen et al., 2021].

In the end of November a cyclone brought extremely warm and moist air to the MOSAiC site [Rinke et al., 2021]. In the beginning of December a cyclone caused extremely anomalous deviations in radiation, temperature and water vapour content at the MOSAiC site [Rinke et al., 2021]. After this event, no temperature extremes were observed at the site until Febru-

ary, as the number of cyclones and their intensity was very low in December and January [Rinke et al., 2021]. For December and January, monthly mean temperature and *air pressure* anomalies are small along the track (see figure 3.8). Inter quartile range (IQR) and total range of most of the variables are smaller than in the monthly climatology, indicating and further proving average conditions (see figure 3.9).
At a larger scale, slightly higher mean pressure and lower mean temperatures are visible over Siberia and Alaska for December. Slightly lower pressure and higher temperatures occurred in Europe, western Russia, Chukchi Sea and parts of northern Canada (see figure 3.8). Mean wind directions were mainly north-west to south-west rather than south, according to the climatology (see figure 3.7).

In January, pressure systems shifted, so that strongly negative pressure anomalies of up to $-15\,hPa$, accompanied by warm air of up to $+8°$C were located over Siberia and the Arctic Basin along the Russian coast [Krumpen et al., 2021; Rinke et al., 2021; Ballinger et al., 2020] (see figure 3.8). In the beginning of 2020, a strong zonal jet between mid latitudes and the pole caused strong westerly winds and locked cold air in the Arctic north of Greenland and North America [Ballinger et al., 2020]. January and February mean near surface *wind direction* was south-east, which is in the climatology mean (see figure 3.7). The strong near surface temperature anomalies and strong stratospheric Polar Vortex, can be seen in connection to a strong positive phase of the Arctic Oscillation (AO). The positive AO also caused weaker atmospheric circulation over the Central Arctic and 20% faster ice drift. During the course of winter, the negative large scale pressure anomalies shifted towards the Beaufort Sea. [Shupe et al., 2020b; Ballinger et al., 2020; Rinke et al., 2021; Krumpen et al., 2021].

The MOSAiC expedition was most affected by the positive AO in February, when the AO index was the highest and the near surface *air pressure* was extremely low with a monthly mean deviation of $-15\,hPa$ in the Central Arctic and at the MOSAiC site (see 3.9). Both the number of cyclones and their intensity was above average in February. For example, the anomalous 18-22th February winter warming event again brought extreme radiation, temperature and water vapour values [Rinke et al., 2021].

Chapter 4

Comparison of ERA5 Reanalysis with MOSAiC Observations for Winter 2019/2020

A statistical approach analysing ERA5 model abilities and deficiencies is applied using MOSAiC observations and ERA5 reanalysis data along the MOSAiC trajectory for the winter months December 2019 to February 2020. Main questions are the differentiation of the two atmospheric states and ERA5 simulation of the radiatively clear state, described in section 3.1.2, with the frequency of occurrence (section 4.1,4.2), and timing (section 4.3). Therefore, the applicability of the two-atmospheric-Arctic-winter-states on the MOSAiC winter trajectory is assessed (section 4.1). For more, it is analysed how well ERA5 simulates the surface radiative energy budget and surface and near-surface meteorological aspects in relation to the clear sky atmospheric states (sections 4.1 to 4.3). Furthermore, the ERA5 surface temperature simulation and warm bias will be assessed in the time series (section 4.3).

4.1 Representation of the Winter Arctic Atmospheric States

In order to analyse, if ERA5 can model clear sky conditions, it will be analysed whether ERA5 can differentiate the two Arctic winter atmospheric states correctly. In addition, the applicability of the two state theory onto the winter 2019/2020 Central Arctic is tested.

The bimodal nature of the winter Arctic atmosphere can be identified by analysing the frequency of occurrence (or probability density) distribution of the *surface net long wave radiation* (LWN) and *surface downwelling long wave radiation* (LWD) [Stramler et al., 2011; Raddatz et al., 2015]. The two states are also related to and influenced by meteorological and subsurface variables [Stramler et al., 2011]. In the following, LWN and LWD are analysed on their bimodal structure. The *surface upwelling long wave radiation* (LWU), *2-meter air temperature* ($T2M$), *surface temperature* (IST, SKT), *mean sea level air pressure* (pp), *wind direction* (w_{dir}) and *wind speed* (w_{sp}) are analysed with respect to their relation to the atmospheric states. Additionally, it is checked, how well ERA5 is simulating named aspects of the lower atmosphere.

The analysis was carried out for all three MOSAiC Distributed Network (DN) sites L1, L2 and L3 (see section 2.2,2.7). Since the results show consistent characteristics, only results for site L2 are shown in this chapter. In the appendix, figures and tables can be found for L1 and L3.

4.1.1 Up- and Downwelling Long Wave Radiation

At the MOSAiC observational site L2 the *net long wave radiation* LWN ranges from $-76\,W/m^2$ to $+15\,W/m^2$ with its highest values in the frequency of occurrence distribution at around $-5\,W/m^2$ and $-43\,W/m^2$ (figure 4.1a), and thus these two peaks are separable by $-30\,W/m^2$. The values for the *downwelling long wave radiation* LWD observations are ranging from $116\,W/m^2$ to $267\,W/m^2$. The LWD distribution shows a bimodal characteristic with highest frequencies around $157\,W/m^2$ and slightly lower frequencies between $200\,W/m^2$ and $235\,W/m^2$ (figure 4.1b). A $LWD = 160\,W/m^2$ threshold is separating the high frequency lower LWD half of the distribution. The *upwelling surface long wave radiation* (LWU) observations are ranging from $168\,W/m^2$ to $270\,W/m^2$ and have highest frequencies of occurrences between $190\,W/m^2$ and $210\,W/m^2$ (figure 4.1c). The distribution shows no bimodal characteristics and, thus, cannot distinguish between the two states, however it is also not symmetrical around one value.

The ERA5 reanalysis does not capture the general characteristics of the observed distributions of the radiative variables (see figure 4.1a-c). The LWN and LWD distributions obtained from ERA5 are not bimodal, but instead have a wide single distribution, mostly centred at the middle of the variable range, at around $-37\,W/m^2$ and $185\,W/m^2$ for LWN and LWD, respectively. LWU is centred at around $213\,W/m^2$ and is thereby shifted towards higher values by $16\,W/m^2$, compared to the observations. The distributions are not entirely symmetrical. Also, ERA5 does not capture the observed value-ranges of the radiative variables, which is most visible

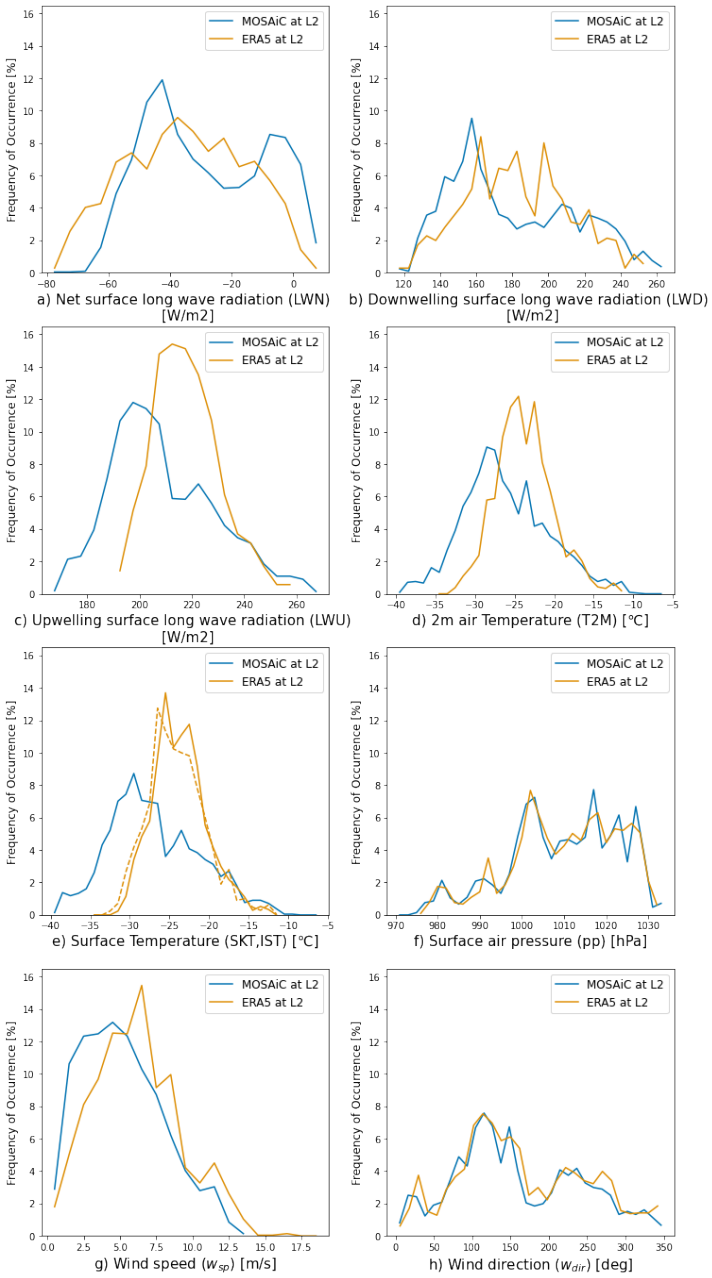

Figure 4.1: Frequency of occurrence of surface and near surface variables for winter MOSAiC observations (blue) and ERA5 reanalysis (orange) at the MOSAiC site L2 and the associated closest reanalysis grid cell. a) *net surface long wave radiation* (LWN), b) *downwelling surface long wave radiation* (LWD), c) *upwelling surface long wave radiation* (LWU), d) *2m air temperature* ($T2M$), e) *ice surface temperature* (IST), f) *surface air pressure* (pp), g) *wind speed* (w_{sp}) and h) *wind direction* (w_{dir}). In addition, e) views the ERA5 *skin temperature* (SKT_{ERA5}) (dashed line). The used time period is 1.12.2019 to 26.2.2020. The bin width is $5\,W/m^2$ for all radiative variables.

for the LWU, by missing all values smaller than $190\,W/m^2$ and larger than $263\,W/m^2$. As a consequence, the LWU distribution is narrower and mid-range values are too frequent. For LWD and LWN, ERA5 misses few marginal values underestimating the frequency of $LWN > -15\,W/m^2$ and heavily overestimating $LWN < -55\,W/m^2$.

4.1.2 Surface and 2-meter Air Temperature

The distributions of *2 meter air temperature* ($T2M$) and *surface temperatures* (IST, SKT) show very similar characteristics compared to the LWU distribution, in particular concerning their shape, the model vs. observation differences, and their single-peak structure (figure 4.1d,e). The MOSAIC observations range from -40°C to approximately -10°C, while the reanalysis misses values below -33°C and higher than -11°C, for all used temperature variables. Highest frequencies are observed around -29°C for both variables, with $T2M$ slightly shifted towards higher temperatures. $T2M$, IST and SKT are most frequently modelled in between -22°C and -27°C. As for the observations, $T2M$ is slightly warmer. SKT and IST are very similar in the distribution. Comparing, the most frequent temperatures for MOSAiC and ERA5, ERA5 is about 4°C warmer for $T2M$ and IST.

4.1.3 10-meter Wind and Mean Sea Level Air Pressure

The *10-meter wind speed* distributions range from $0\,m/s$ to $14.6\,m/s$ (MOSAiC) and $16.8\,m/s$ (ERA5) with peaks in their distributions at around $4.5\,m/s$ (MOSAiC) and $6.5\,m/s$ (ERA5), following (visually) a Weibull distribution (figure 4.1g). This is not further analysed, as it is beyond the scope of this study, but it can be said, that ERA5 is able to represent the observed *10-meter wind speed*. The *10-meter wind direction* distributions obtained from observations and ERA5 show similar characteristics (figure 4.1h).

Mean sea level air pressure occurrences are very variable, but very similar for observations and model values, along the variable range of $974\,hPa$ to $1034\,hPa$. Values in between $1000\,hPa$ and $1027\,hPa$ are more frequent, than lower ones (figure 4.1f).

4.2 Simulations of Clear Sky Conditions by ERA5

In this section, it is analysed, how often clear sky conditions were present in the MOSAiC winter and how often the reanalysis simulates clear sky conditions correctly and incorrectly.

For analysing the ability of the reanalysis model to simulate radiatively clear sky periods, the following three cases are analysed

Thresh.	*hit*	*miss*	*false alarm*
LWN	41.0	10.5	17.5
LWD	17.6	20.1	4.6

Table 4.1: Frequencies [%] of (in-) correct clear sky condition simulation at L2, using a threshold of $LWN < -30\,W/m^2$ and $LWD < 160\,W/m^2$. The frequencies relate to ERA5 correct simulation of occurring clear sky conditions (*hit*), ERA5 missing to model occurring clear sky conditions (*miss*) and ERA5 falsely simulating clear sky conditions (*false alarm*). The frequencies are relative to the number of hourly data from 1.12.2019 to 26.2.2020.

- *hit:* ERA5 correctly simulating occurring clear sky conditions
- *miss:* ERA5 missing to simulate occurring clear sky conditions
- *false alarm:* ERA5 incorrectly simulating clear sky conditions when none occurred

The relative occurrence is shown in %, i.e. the number of hours with *hit*, *miss* and *false alarm* divided by the total number of hours over the entire time period. Note, the occurrence of *all* radiatively clear sky periods in the MOSAiC measurements are provided by the sum of *hit* plus *miss*.

We are using LWN and LWD with thresholds of $LWN < -30\,W/m^2$ and $LWD < 160\,W/m^2$ in order to define clear atmospheric states. In the hourly observations from 1.12.2019 to 26.2.2020 along the L2 trajectory the clear atmospheric states (*all*) are detected in 52% (LWN) and 38% (LWD) of the time (table 4.1).

In contrast, the relative occurrence of clear sky conditions simulated by ERA5 are 59% (LWN) and 22% (LWD) of the winter. Using the LWD threshold, *misses* are slightly more often present, than *hits*, but *false alarms* are rare. Using the LWN threshold, *misses* only make up a fourth compared to *hits*, but *false alarms* make up as much as half of the *hits*. In other words, a $LWD < 160\,W/m^2$ threshold minimises the number of *false alarms*, but increases the number of *misses*, while the $LWN < -30\,W/m^2$ thresholds acts vice versa.

4.3 Time Series Analysis of Winter 2019/2020

In this section, it will be analysed, to which extent ERA5 simulates the clear sky period timing correctly and when clear sky conditions occurred during the MOSAiC winter. The general meteorological situation, the radiative deviations in the surface radiation energy budget and the ERA5 warm bias will be assessed along the trajectory for these months, as well.

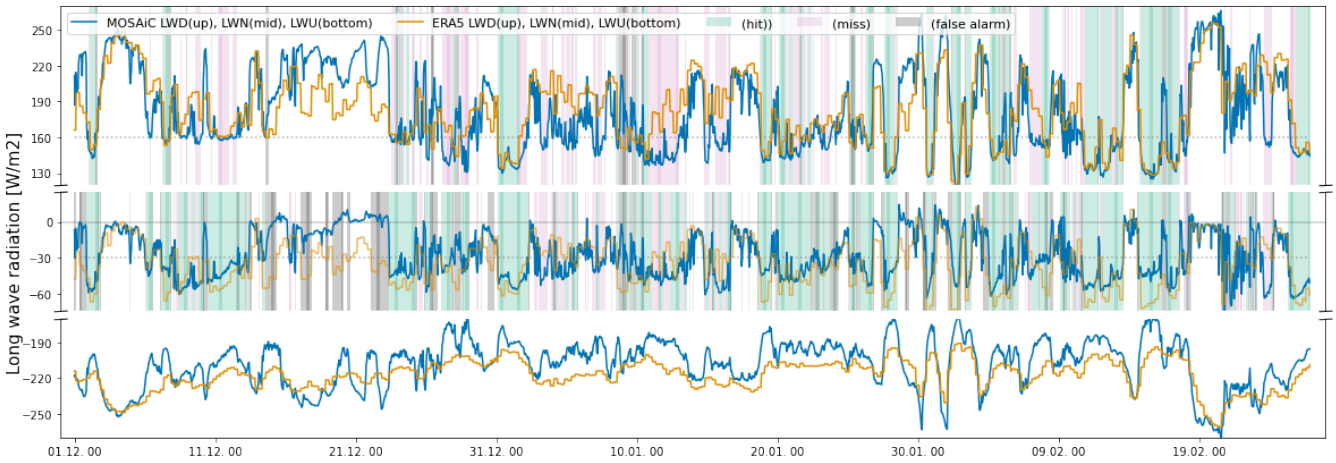

Figure 4.2: Time series of surface radiation variables *downwelling long wave radiation* (LWD) (top), *net long wave radiation* (LWN) (mid) and *upwelling long wave radiation* (LWU) (bottom) [W/m^2] for winter MOSAiC observations (blue) and ERA5 reanalysis (orange) along the MOSAiC L2 trajectory from 1.12.2019 to 26.2.2020. Time periods of (in-) correct clear sky condition simulation, according to the $LWD < 160\,W/m^2$ threshold, are given by the background colouring with correct ERA5 clear sky simulation (*hits*, green), clear sky conditions missed by ERA5 (*miss*, red) and false simulation of clear sky conditions by ERA5 ($false\ alarm$, grey), in the LWD figure. The LWN figure uses the $LWN < -30\,W/m^2$ threshold accordingly. The respective LWN and LWD thresholds are depicted as horizontal dotted lines.

4.3.1 Up- and Downwelling Long Wave Radiation

There is high similarity, between the observed temporal evolution of LWD and LWN with high variability on a scale of hours to days, while LWU is less variable in time (figure 4.2). The months show highly different behaviour for LWD. LWD is mostly high (between $170\,W/m^2$ and $250\,W/m^2$) from 1.12. to 23.12.2019 and lower (between $140\,W/m^2$ and $220\,W/m^2$) until the 25.1.2020. For February, the magnitude of variation covers the entire variable range of $125\,W/m^2$ to $260\,W/m^2$. This change in variability on a scale of hours to days can also be found in LWU and LWN, but with smaller magnitude.
ERA5 deficiencies of the surface radiative variables are varying along the time series (see figure 4.2). In general, ERA5 does not capture the magnitude of variation and variability in timescales of hours to days. In contrast, ERA5 simualtes extreme LWD values and temporal evolution well, for some times, e.g. for 10th to 15th of February.

In the MOSAiC winter time series, periods of correct clear sky simulation (*hits*), missed clear sky conditions (*miss*) and falsely modelled clear sky

conditions ($false\ alarm$) are shown (4.2). For categorisation, thresholds of $LWD < 160\,W/m^2$ and $LWN < -30\,W/m^2$ are used for the LWD and LWN variable, in order to compare the time periods along the time series. Following, observed clear sky periods are indicated by the sum of *hits* and *misses*, showing many short clear sky periods with likewise short interruptions. Clear sky periods appear in all months, but are not equally distributed during the months. The difference of the marked clear sky periods, due to the used threshold, is small. As differences exist, the ability, to model the clear sky period and their timing, is dependent on the threshold choice. Correctly modelled and missed clear sky conditions ($hit, miss$) appear throughout the months with a duration of hours to few days (see figure 4.2). Occurring $false\ alarms$ are very short in the order of hours. Consistent with earlier findings, $false\ alarms$ are rare when using the LWD threshold and much more frequent for the LWN thresholds. The timing of some clear sky periods is sometimes captured dependent on the threshold, in general. Because of the simultaneous categorisation of clear sky conditions for all thresholds and sites, the time period around the beginning of January (31.12.2019 to 2.1.2020) and mid-February (10.2.2020 to 20.2.2020) will be analysed in the detailed clear sky analysis in chapter 5.

4.3.2 Surface and 2-meter Air Temperature

The observed *2m air temperature* ($T2M$) and *ice surface temperature* (IST) show very similar characteristics, although $T2M$ is slightly higher in cold temperatures, which is not analysed further in this work (see figure 4.3). Lowest temperatures are often observed during clear sky periods and higher temperatures often occur in periods of high synoptic activity. Yet some clear sky periods show higher temperature than some cloudy periods.

The ERA5 time series captures the high similarity of $T2M$ and IST. Consistent with the findings of previous sections, ERA5 does not capture the observed variability in time and magnitude well, in general. All three temperature variables have a positive bias of $\Delta IST_{MOSAiC} = 2°\text{C}$ to $3°\text{C}$. As a result, ERA5 temperature errors can be very high occasionally, with up to $\Delta IST_{MOSAiC} + 12°\text{C}$. As the lack of modelled variability can have more influence than the positive bias at times, the modelled temperatures can be lower than the observed ones, with up to $\Delta IST_{MOSAiC} - 9°\text{C}$ error. Consistent simulation of temperature and temporal evolution can be seen, for example, during the onset of the cyclones of early December, 1.2 and 19.2.2020, which are discovered in Rinke et al. [2021]. Reanalysis IST and SKT do not show relevant difference in the time series.

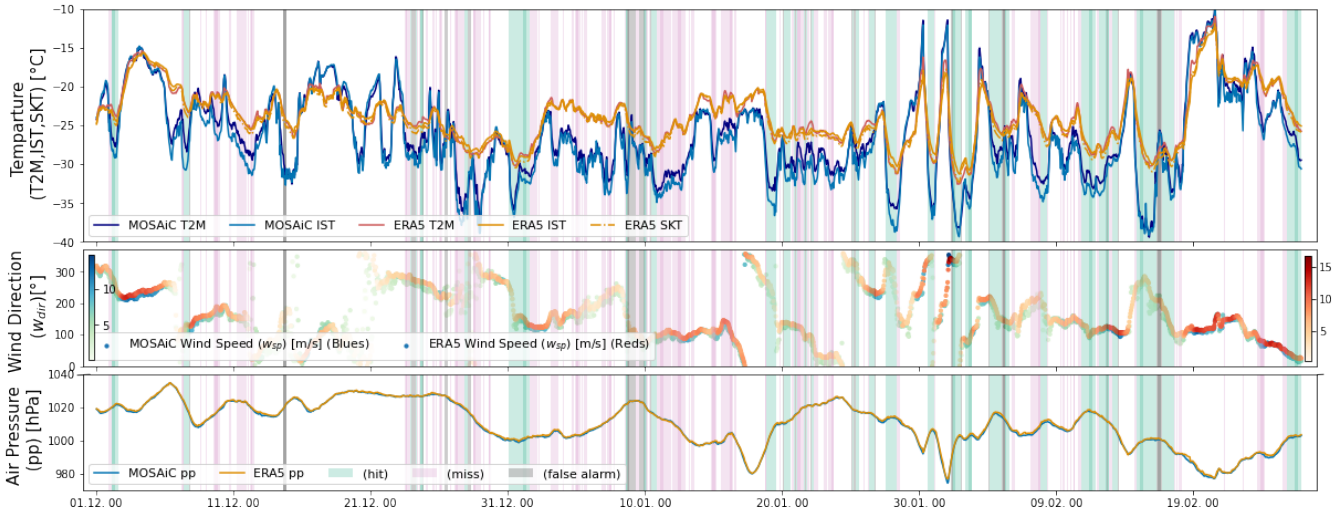

Figure 4.3: Time series of surface and near surface meteorological variables for MOSAiC observations (blue) and ERA5 reanalysis (orange) at MOSAiC L2 from 1.12.2019 to 26.2.2020. Shown are (top) *2m air temperature* ($T2M$) (darker colours), *ice surface temperature* (IST) (lighter colours) and ERA5 *skin temperature* (SKT_{ERA5}) (dashed), (mid) *wind direction* (w_{dir}) (on y-axis) and *wind speed* (w_{sp}) (colour range) and (bottom) *surface air pressure* (pp). Time periods of (in-) correct clear sky condition simulation, according to the $LWD < 160\,W/m^2$ threshold, as in figure 4.2, with correct ERA5 clear sky simulation (*hit*, green), clear sky missed by ERA5 (*miss*, red) and falsely simulated by ERA5 (*false alarm*, grey).

4.3.3 10-meter Wind and Mean Sea Level Air Pressure

The *wind direction* has both, constant periods of hours to days, and rapid in- and decreases within several hours, for both MOSAiC winter and occurring clear sky periods (see figure 4.3). During January and February, for all periods at which the wind direction is stable for more than a few hours, the *wind direction* is around 120° to 140° (south-east), which is also the mean wind direction of these months. Many prominent and some of the longest clear sky periods during winter 2019/20 occur during this constant *wind direction*. The *wind direction* itself is captured well by ERA in temporal evolution. The *wind speed* is observed high and low in both atmospheric states and is captured well by ERA5.
The MOSAiC drift experienced high *surface air pressure* of up to $1035\,hPa$ for a high percentage of early winter and more frequent lower pressure and more variability in February 4.3). Although lowest pressure values can be found in non-clear periods in the time series plot, high pressure $> 1000\,hPa$ also comes along with non-clear periods, as for the beginning of December. In addition, pressure is also not always constant in clear periods. ERA5 represents the characteristics of *surface air pressure*.

Chapter 5

Comparison of ERA5 Reanalysis with MOSAiC and MODIS Satellite Observations for Two Clear Sky Cases

For analysing how well the ERA5 reanalysis represents the surface temperatures during winter clear sky periods in the Arctic, two example periods are used along the trajectory (section 5.1). The time periods cover the beginning of January (JAN: 31.12.2019 3:00 to 2.1.2020 4:00) and mid-February (FEB: 10.2.2020 5:00 to 17.2.2020 14:00). In order to provide for a pan-Arctic view, the ERA5 reanalysis is compared to MODIS satellite observations for the two periods and for the entire Arctic domain (section 5.2). Snow and ice layer representation of the reanalysis model is analysed as possible cause of the discovered deficiencies for the Arctic domain (section 5.2).

5.1 Time Series Analysis

The periods of early January (31.12.2019 3:00 to 2.1.2020 4:00, *JAN*) and mid-February (10.2.2020 5:00 to 13.2.2020 14:00, 14.2.2020 18:00 to 17.2.2020 14:00, *FEB*) are depicted as time series for near-surface and surface radiation, temperature, wind and *air pressure* variables (figure 5.1, 5.2). The time series are selected from section 4.3, because they were both observed and simulated as clear sky for all sites and thresholds and are the longest available in DJF winter 2019/20. Exact beginning and end are explained in the following. The general meteorological large-scale and regional conditions of January and February are previously described in sections 3.3 and 4.

L2	JAN	FEB
$\Delta T2M_{MOSAiC}$	2.9	4.2
ΔIST_{MOSAiC}	4.0	5.2
ΔSKT_{MOSAiC}	3.5	4.5

Table 5.1: Temperature bias ($\Delta T = T_{ERA5} - T_{MOSAiC}$) [°C] along the MOSAiC L2 trajectory for the clear sky periods JAN and FEB.

5.1.1 January Period (JAN)

The observed LWN and LWD decrease from high values to below the threshold on early 31.12.2019, marking the beginning of the analysed clear sky period (see figure 5.1). LWN and LWD remain about constant, slowly increasing until the 2.1.2020, when the thresholds are exceeded at 4:00 simultaneously, marking the end of the 50 *hour* clear sky period. LWU does not drop as much at the beginning of the period, but shows similar gradual increase during the clear sky period. ERA5 captures the drop of LWN and LWD on the 31.12.2019 in timing and approximate magnitude. During the clear sky conditions, simulated LWN and LWD fluctuate slightly around the observed values, increasing too quickly at the end. LWU is simulated with too large values for the entire clear sky period.

The analysed clear sky period shows some of the lowest surface and *2m temperatures* of the winter 2019/20 (see figure 5.1). At the beginning, the temperatures drop down to observed $IST = -37$°C and $T2M = -36$°C and increase again gradually towards the end of the period. The reanalysis does not capture the lowest temperatures, nor the variability within the period or the difference between surface and *2m temperature*. The lowest simulated values are around -30°C for all temperature variables. The resulting temperature error from the MOSAiC observations is up to $\Delta IST_{MOSAiC} = 8$°C and $\Delta T2M_{MOSAiC} = 6$°C. The temperature bias for the January clear sky period is $\Delta IST_{MOSAiC} = 4$°C and $\Delta T2M_{MOSAiC} = 3$°C (see table 5.1). ERA5 SKT is slightly lower than IST and, thus, has slightly smaller errors with maximum $\Delta SKT_{MOSAiC} = 7$°C and mean $\Delta SKT_{MOSAiC} = 3.5$°C.

The *wind direction* is changing from 240° to 110° during the first half of the 31.12.2019, when temperatures are lowest, and is constant until after the end of the clear sky period (see figure 5.1). The *wind speed* is lowest, under $< 1\,m/s$, during the change of direction and increases up to $8\,m/s$ towards the end. ERA5 simulates wind variables agreeing to the observation in general, but does not capture the timing of changing *wind direction* and easternmost values entirely. The air pressure is observed fairly constant around 1000 hPa, with the reanalysis agreeing having consistent characteristics.

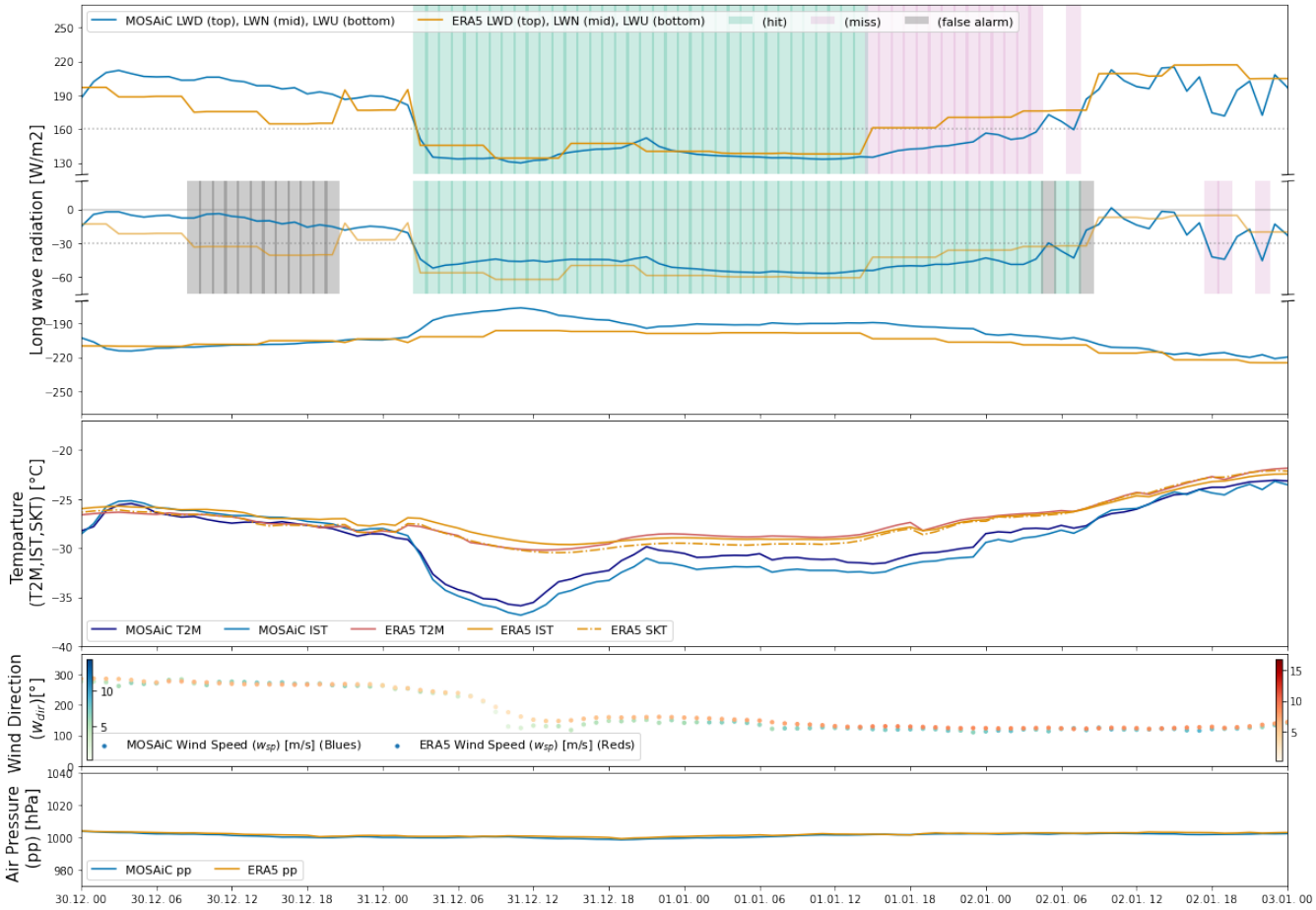

Figure 5.1: Time series of surface and near surface long wave radiation and meteorological variables for MOSAiC observations (blue) and ERA5 reanalysis (orange) along the MOSAiC L2 trajectory for the clear sky period JAN. Shown are (top row) surface radiation variables with *downwelling long wave radiation* (LWD) (top), *net long wave radiation* (LWN) (mid) and *upwelling long wave radiation* (LWU) (bottom) [W/m^2], (second row) temperature variables with *2m air temperature* ($T2M$) (darker colours), *ice surface temperature* (IST) (lighter colours) and ERA5 *surface skin temperature* (SKT_{ERA5}) (dashed), (third row) wind variables with *wind direction* (w_{dir}) (on y-axis) and *wind speed* (w_{sp}) (colour range) and (bottom row) *surface air pressure* (pp). Time periods of (in-) correct clear sky condition simulation are given by background colouring, as in figure 4.2. Correct ERA5 clear sky simulation ($hits$, green), clear sky conditions missed by ERA5 ($miss$, red) and false simulation of clear sky conditions by ERA5 ($false\ alarm$, grey) are marked according to the $LWD < 160\,W/m^2$ threshold within the LWD figure. The LWN figure uses the $LWN < -30\,W/m^2$ threshold accordingly. The respective LWN and LWD thresholds are depicted as horizontal dotted lines.

5.1.2 February Period (FEB)

February 2020 is characterised by strong variability in the time of hours to days for the surface radiative energy budget and temperatures, along the MOSAiC trajectory (see figure 4.2, 4.3). LWD and LWN fluctuate around the thresholds on the early 10.2.2020, thus the 10.2.2020 5:00 is selected as beginning of the clear sky period based on LWN falling below $LWN < -30\,W/m^2$ (see figure 5.2). Later pan-Arctic satellite observations show, that L2 was sufficiently cloud free on this day. Low radiation values can be found until 17.2. 14:00, which marks the end of the 151 *hour* clear sky period. Low radiation values are interrupted by short time exceedance of LWN and LWD thresholds and temporary high radiation values on the 11th, 14th and 16th. All interruptions are characterised by rapid in- and decrease of LWD and LWN and are excluded from calculating FEB clear sky period temporal means. Even though LWU has more gradual evolution in time, all of the tendencies and short time interruptions, can also be seen for LWU. ERA5 represents the timing of the analysed clear sky period within the error range of few hours and especially good for some of the rapidly increasing radiation values. The reanalysis also captures the short time interruptions, though not always with the exact magnitude or duration. Constant, low radiative values are captured for LWD, but are constantly too low/high for LWN and LWU.

Temperatures are low for low radiation values and lowest on the 15th with $IST, T2M = -39°\text{C}$ (see section 5.2). High temperatures occur during the short time interruptions with high radiation values and highest on the 14th with $-18°\text{C}$. $T2M$ is slightly higher than IST. Except for the 16.2. temperature increase, ERA5 captures the temporal evolution, but with too small variability, a warm bias and insufficient difference between $T2M$ and IST. Errors are highest for lowest temperatures in the second half of the period with $\Delta IST_{MOSAiC} = 12°\text{C}$ ($\Delta SKT_{MOSAiC} = 11°\text{C}$) and $\Delta T2M_{MOSAiC} = 10°\text{C}$. These are also the highest temperature errors along the L2 trajectory in the winter 2019/20. The temperature bias of ERA5 is $\Delta IST_{MOSAiC} = 5°\text{C}$ ($\Delta SKT_{MOSAiC} = 4.5°\text{C}$) and $\Delta T2M_{MOSAiC} = 4°\text{C}$ for the analysed February period along the trajectory (see table 5.1).

The *wind direction* is at constant 140° for the first half and swings to 277° on the 14.2.2020 (see figure 5.2). The *wind speed* is increasing up to $11.5\,m/s$ until the 14.2. and is low for the second half of the clear sky period. ERA5 represents the wind variables consistent with the observations for the first half of the period, but cannot capture the variability for the second half. The *air pressure* is high at the beginning with $1020\,hPa$ and lower for the rest of the clear sky period with approximately $990\,hPa$ on the 14th and the last day. ERA5 represents the pressure consistent with the observations.

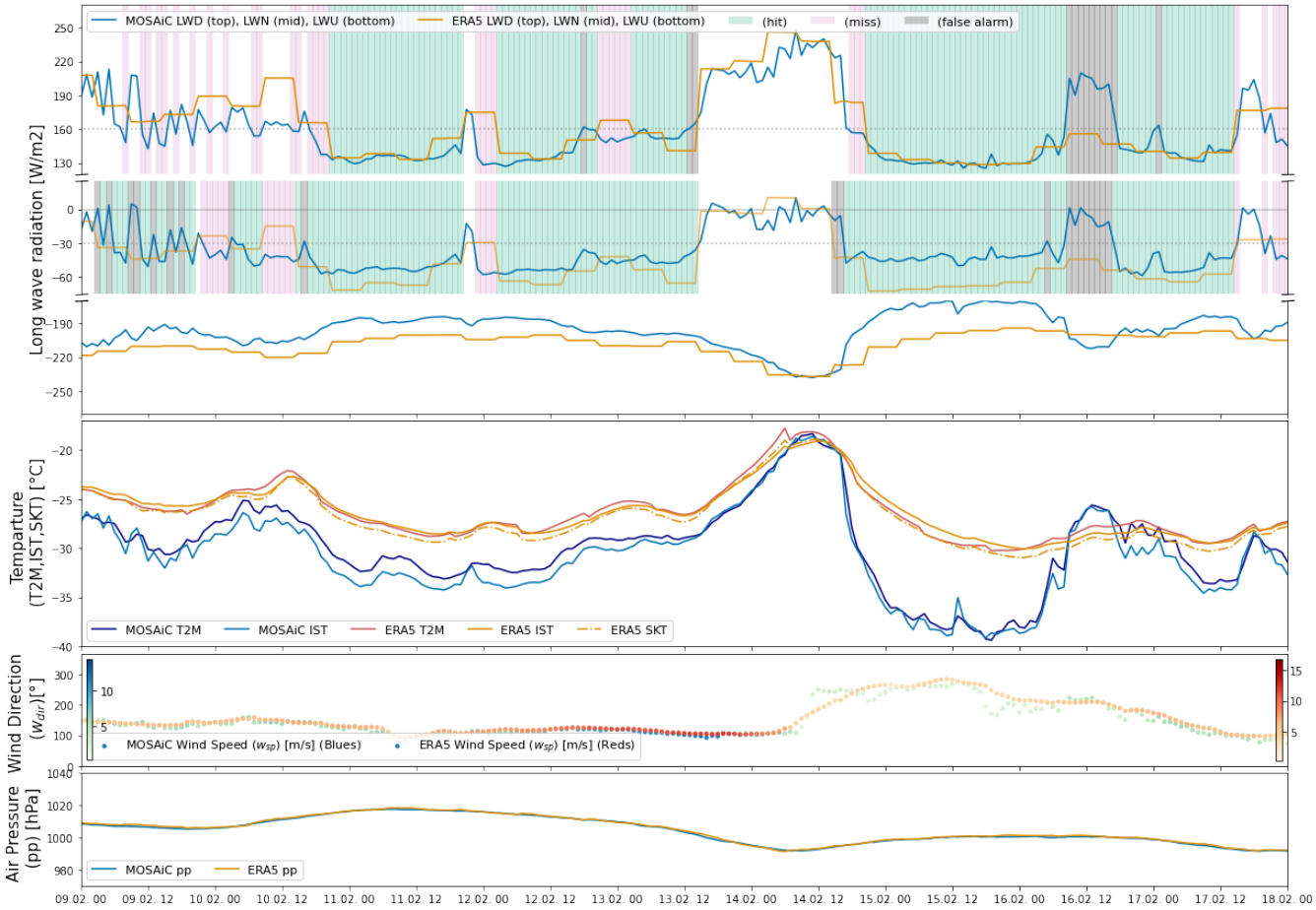

Figure 5.2: Time series of surface and near surface radiation and meteorological variables for MOSAiC observations (blue) and ERA5 reanalysis (orange) along the MOSAiC L2 trajectory for the clear sky period FEB. Shown are (top row) surface radiation variables with *downwelling long wave radiation* (LWD) (top), *net long wave radiation* (LWN) (mid) and *upwelling long wave radiation* (LWU) (bottom) [W/m^2], (second row) temperature variables with *2m air temperature* ($T2M$) (darker colours), *ice surface temperature* (IST) (lighter colours) and ERA5 *surface skin temperature* (SKT_{ERA5}) (dashed), (third row) wind variables with *wind direction* (w_{dir}) (on y-axis) and *wind speed* (w_{sp}) (colour range) and (bottom row) *surface air pressure* (pp). Time periods of (in-) correct clear sky condition simulation are given by background colouring, as in figure 4.2. Correct ERA5 clear sky simulation ($hits$, green), clear sky conditions missed by ERA5 ($miss$, red) and false simulation of clear sky conditions by ERA5 ($false\ alarm$, grey) are marked according to the $LWD < 160\,W/m^2$ threshold within the LWD figure. The LWN figure uses the $LWN < -30\,W/m^2$ threshold accordingly. The respective LWN and LWD thresholds are depicted as horizontal dotted lines.

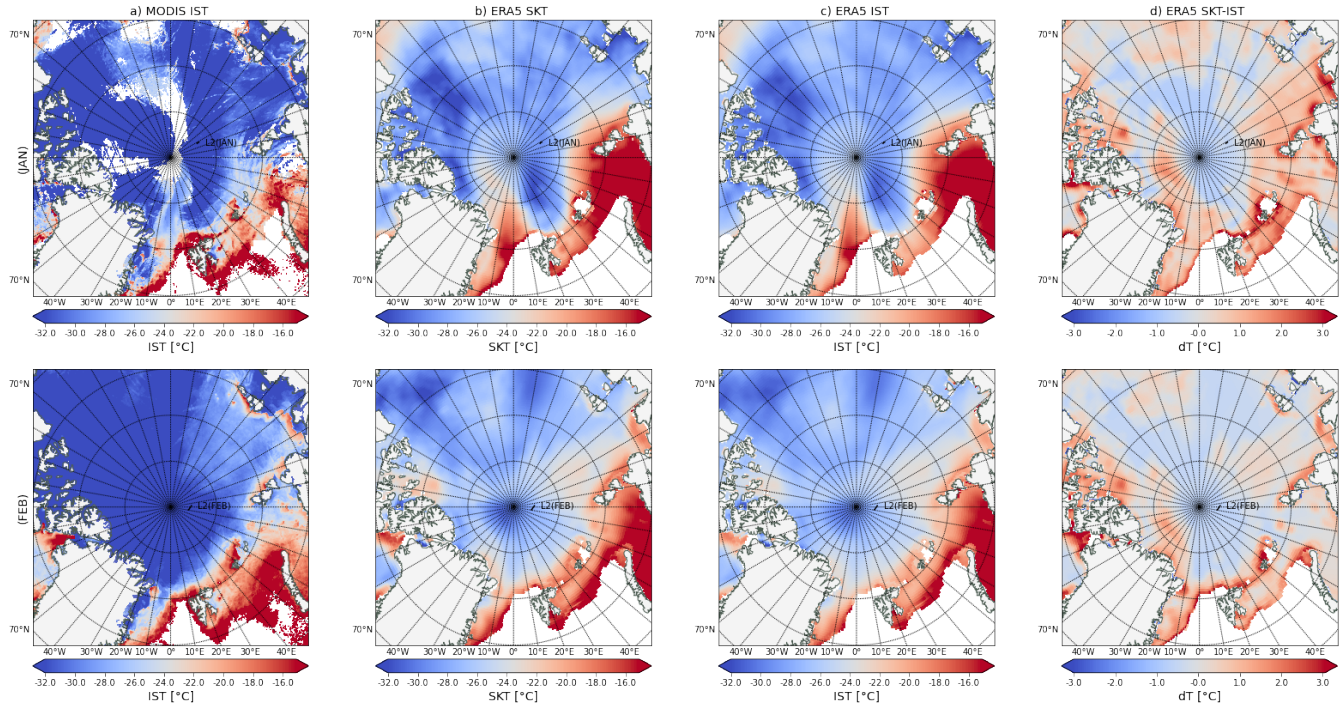

Figure 5.3: Mean surface temperature in the Arctic during clear sky periods JAN (top row) and FEB (bottom row) for a) MODIS *ice surface temperature* (IST_{MODIS}), b) ERA5 *surface skin temperature* (SKT_{ERA5}), c) IST_{ERA5} and d) $SKT_{ERA5} - IST_{ERA5}$ [°C]. The MOSAiC L2 trajectory covered during these periods is marked as black line.

5.2 Pan-Arctic Analysis

The surface temperature error will be analysed for the described clear sky periods in the Arctic domain. Arctic large-scale meteorological, snow and sea ice conditions are previously described in section 3.3. As the analysis is focused on the radiative energy budget over snow covered sea ice, little attention will be put on the ice margins, though regions with lower *ice concentration* inside the ice edge will not be exempt.

5.2.1 Absolute Surface Temperature

In order to understand the spatial characteristics of the ERA5 reanalysis surface temperature errors, maps of MODIS and ERA5 absolute surface temperature are given as daily-means (figures 7.7, 7.8, 7.9, 7.10) and as temporal mean covering the entire analysed periods (figure 5.3). For better comparability between observations and reanalysis, the figures have the same colour scale, which is chosen such that regional differences in the reanalysis are visible. Consequently, the observed and simulated temperature

ranges are not shown entirely, and since there are relatively large differences between MODIS and ERA5, MODIS regional differences are not visible for low temperatures.

In the MODIS observations, the mean clear sky surface temperatures range from −60°C to 0°C, locally (as noted above extreme temperatures are not visible in figure 5.3a). The regional characteristics of the surface temperature are complex. On a regional scale, lowest IST_{MODIS} of around −35°C are predominantly observed in the western half of the Arctic. Most of the Arctic has IST_{MODIS} in a range of −35°C to −28°C. Patterns of locally higher temperatures can be seen north of the Chukchi Sea and Fram Strait for the January period (see figure 5.3a). Highest IST_{MODIS} of $> -24°$ can be seen along the ice margins towards the Atlantic Ocean and the Eurasian continent. On a regional scale, JAN has lower temperatures than FEB.
On a daily view, warmer temperatures spread from the Russian coast westwards, from 31.12.2019 to 2.1.2020, from 13.2.2020 to 15.2.2020 and the 17.2.2020, (see figure 7.7,7.8). In more detail, warmer temperatures spread in a narrow channel, coming from the Kara- and Laptev Sea (13.2.), spanning to the MOSAiC site and North Pole (14.2.) and reaching the Canadian coast (15.2.). Since the surrounding Arctic areas have relatively cold temperatures, the regional temperature gradient can be high.

In general, the ERA5 model simulates warmer mean surface temperatures for the JAN and FEB clear sky periods (see figure 5.3b,c). In particular, IST_{ERA5} and SKT_{ERA5} range down to −36°C, but low temperatures of around −35°C are not simulated on a regional scale, as for MODIS. IST_{ERA5} and SKT_{ERA5} from −35°C to −28°C are present for distinct regions, e.g. north of Canada and Alaska, rather than for most of the Arctic. IST_{ERA5} and SKT_{ERA5} of $> -24°$ are simulated consistent with MODIS observations, but too warm. The slightly warmer area north of the Fram Strait in January is captured, but with too high temperatures. As in the observations, JAN is colder than FEB, but with a smaller difference between the months.
Differences between IST_{ERA5} and SKT_{ERA5} are largest at the marginal ice zones and over thin ice (see figure 5.3d). SKT_{ERA5} can also be up to 3°C warmer on thick MYI, where the CI is lower regionally in figure 3.10, e.g. north of the Canadian Archipelago. Slightly negative $SKT_{ERA5} - IST_{ERA5}$ can be seen all over the Arctic where the CI is close to 100%, e.g. at the MOSAiC site, also changing in patterns from JAN to FEB.
On a daily view, ERA5 captures the observed JAN warming from the east (31.12.2019 to 2.1.2020), but not as uniformly and strong (see figure 7.9). For FEB, the reanalysis represents the westwards warm intrusion in shape and timing, but with too high surface temperatures and a slightly longer duration (see figure 7.10).

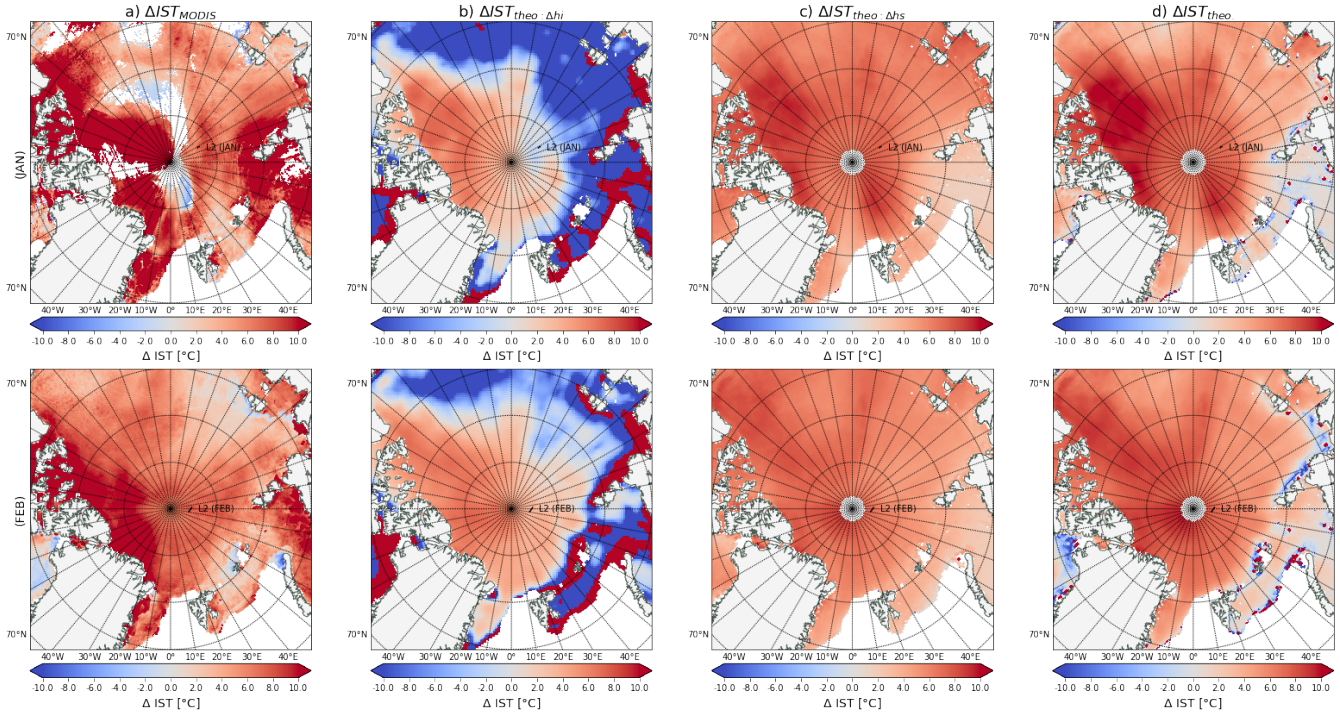

Figure 5.4: Mean ERA5 error of surface temperature [°C] in the Arctic a) compared to MODIS (ΔIST_{MODIS}) and calculated theoretically, dependent on b) *ice thickness* ($\Delta IST_{theo:\Delta hi}$), c) AMSR-E/2 *snow depth* ($\Delta IST_{theo:\Delta hs}$) and d) both snow and ice ($\Delta IST_{theo.}$), as described in section 5.2.2. The spatial distribution is averaged in time for the clear sky periods JAN (top row) and FEB (bottom row). The MOSAiC L2 trajectory covered during these periods is marked as black line.

5.2.2 ERA5 Surface Temperature Compared to MODIS and Theoretical Considerations

In the following, we compare the ERA5 surface temperature IST_{ERA5} to the MODIS observations, to get a spatial error estimate ($\Delta IST_{MODIS} = IST_{ERA5} - IST_{MODIS}$) (see figure 5.4a,5.5a). We also introduce a theoretical error of the surface temperature ($\Delta IST_{theo.}$), which is calculated spatially, using equation 3.6 from section 3.1.1 (see figure 5.4b-d,5.5b-d). $\Delta IST_{theo.}$ is thereby retrieved from the simulated IST_{ERA5}, $h_{i,ERA5} = 1.5\,m$, $h_{s,ERA5} = 0\,m$ and estimates of the reanalysis' misrepresentation of the *snow depth* (Δh_s) and the *sea ice thickness* (Δh_i). The sensitivity of the $\Delta IST_{theo.}$ to Δh_i and Δh_s is analysed separately by comparing to satellite observations ($\Delta h_{i/s} = h_{i/s,obs} - h_{i/s,ERA5}$), or using an $\Delta h_{i/s}$ of $0\,m$, respectively. The used observations, previously shown in figure 3.10, are CryoSat-2/SMOS [Ricker et al., 2017] ($\Delta IST_{theo:\Delta hi}$ in figure 5.4b,5.5b), AMSR-E/2 [Rostosky et al., 2018] ($\Delta IST_{theo:\Delta hs}$ in figure 5.4c) and AMSR/AVHRR [Lee et al.,

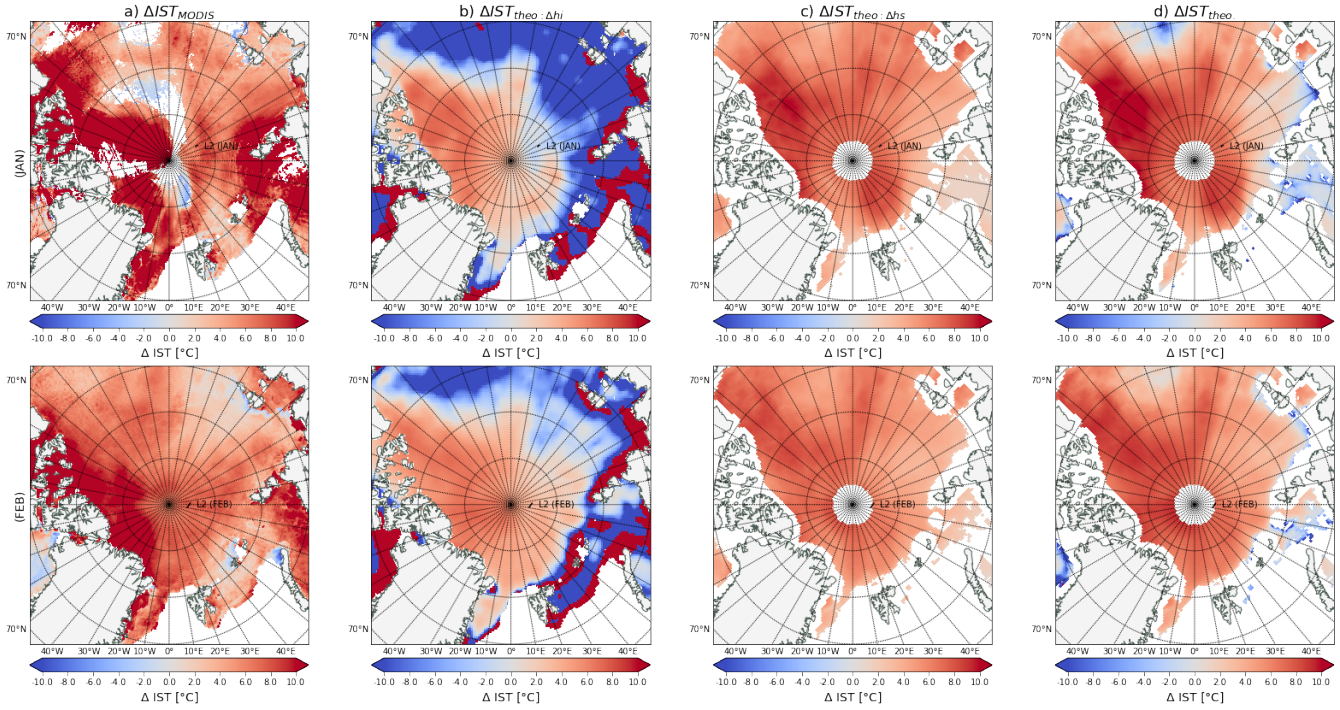

Figure 5.5: Mean ERA5 error of surface temperature [°C] in the Arctic, like in figure 5.4, but using AMSR/AVHRR *snow depth*. The error is a) compared to MODIS (ΔIST_{MODIS}) and calculated theoretically, dependent on b) *ice thickness* ($\Delta IST_{theo:\Delta hi}$), c) AMSR/AVHRR *snow depth* ($\Delta IST_{theo:\Delta hs}$) and d) both snow and ice ($\Delta IST_{theo.}$), as described in section 5.2.2. The spatial distribution is averaged in time for the clear sky periods JAN (top row) and FEB (bottom row). The MOSAiC L2 trajectory covered during these periods is marked as black line.

2021] ($\Delta IST_{theo:\Delta hs}$ in figure 5.5c). For comparison, both observation-based Δh_i and Δh_s are used in figure 5.4d (using AMSR-E/2) and figure 5.5d (using AMSR/AVHRR). Furthermore, regional and pan-Arctic biases are calculated. Both similarities and differences can be found for the depicted ΔIST estimates, and for the two clear sky periods.

Some of the highest ΔIST can be seen north of the North American continent (figure 5.4, 5.5), where highest h_i and h_s are shown in figure 3.10, on a regional scale and common for all error estimates and both periods. Regional biases are high for these high h_i and h_s regions, e.g. the western Central Arctic with $\Delta IST_{MODIS} \approx 8°C$. Regional patterns of high ΔIST also correlate with low absolute $IST < -31°C$ in figure 5.3, predominantly present in the western half, on thick h_i and h_s. Vice versa, regions with $IST > -31°C$ within the western half of the Arctic, have a slightly smaller error. As the IST distribution is different for the two clear sky periods,

there are also regional ΔIST differences between the periods. As a result, ΔIST is not homogeneous across the Arctic.
ΔIST_{MODIS} and the theoretical ΔIST decrease towards the eastern half of the Arctic. The largest part of the Arctic has a ΔIST_{MODIS}, $\Delta IST_{theo.}$ and $\Delta IST_{theo:\Delta hs}$ in the range of 2°C to 6°C (figure 5.4, 5.5). These regions can either have low h_i, e.g. the Beaufort Sea, or high h_i, e.g. the western half of the Central Arctic, where the bias is around 5°C for most of the estimates and both periods. As such, MOSAiC has a local ΔIST_{MODIS} of $3-4$°C and $5-6$°C for the January and February periods, respectively, which is agreeing with the comparison of ERA5 to MOSAiC along the trajectory in previous section 5.1.
Regions of smallest ΔIST are very different for the error estimates and the clear sky periods (figure 5.4, 5.5). Still, all of the lowest errors, within a range of -2°C to 2°C, occur on very high CI and lower h_i in figure 3.10. Dependent on the estimate type and time period, regional biases of the surface temperature are low, with e.g. around $\Delta IST_{MODIS} \approx 3$°C in the East Siberian Sea.
Negative errors can be found in ΔIST_{MODIS} and $\Delta IST_{theo.}$, on mostly small scales and with small error values, e.g. along the Russian coast (figure 5.4,5.5). $\Delta IST_{theo:\Delta hi}$ is around -10°C for regions with h_i sufficiently smaller than $1.5\,m$ in the eastern half of the Arctic.

The different error estimates show difference in error range and patterns (figure 5.4, 5.5). Highest regional ΔIST can be seen for ΔIST_{MODIS} and $\Delta IST_{theo.}$ with around 10°C, also present on the largest extent. $\Delta IST_{theo:\Delta hs}$ and $\Delta IST_{theo:\Delta hi}$ have smaller maximum regional errors of around 8°C and 6°C, respectively. $\Delta IST_{theo:\Delta hi}$ is negative with the lowest values and on the largest extent. $\Delta IST_{theo:\Delta hi}$ and $\Delta IST_{theo:\Delta hs}$ are opposing one another in regions with low h_i, causing a lower $\Delta IST_{theo.}$. $\Delta IST_{theo:\Delta hs_{AMSR/AVHRR}}$ and $\Delta IST_{theo:\Delta hs_{AMSR-E/2}}$ are very similar, though $dh_{s,AMSR/AVHRR}$ causes more negative $\Delta IST_{theo.}$. The pan-Arctic bias of surface temperature is around 6°C in ΔIST_{MODIS} and slightly lower for the theoretical considerations. Still, the ΔIST of the different estimates are within the same order of magnitude for most regions.
Comparing the clear sky periods, highest ΔIST are slightly higher and on a slightly larger area in JAN, for most of the error estimates (figure 5.4, 5.5). The pan-Arctic bias is increasing from JAN to FEB for $\Delta IST_{theo:\Delta hs}$, as negative $\Delta IST_{theo:\Delta hi}$ around -10°C decrease in extent from January to February.
For some regions, the error estimates are controversial, e.g. for the Kara Sea with some of the highest ΔIST_{MODIS}, fairly low $\Delta IST_{theo.}$ and $\Delta IST_{theo:dhs}$, and $\Delta IST_{theo:\Delta hi}$ controversial in itself (figure 5.4, 5.5). Extremely positive and negative values of $\Delta IST_{theo:\Delta hi}$ and $\Delta IST_{theo.}$ along the sea ice margins are an artefact of the calculations, rather than interpretable results.

Chapter 6

Discussion

6.1 The Two Arctic-Atmospheric-Winter-States for the MOSAiC Winter Trajectory

Previous studies relate bimodal distributions of surface radiative variables to the two atmospheric Arctic winter states, described in section 3.1.2, that are similar to the one for MOSAiC winter [Stramler et al., 2011; Graham et al., 2017; Shupe et al., 2020a] (figure 4.1). Since the MOSAiC observations capture the characteristics of the two states as well (see section 4.1), we can assume, that the two state theory is also applicable to the MOSAiC winter observations and, likely the Central Arctic winter 2019/20.

In detail, the part of the distribution related to the radiatively clear state is located at strongly negative LWN of $-43\,W/m^2$ and LWD around $157\,W/m^2$ and the part related to the opaquely cloudy state is located around $-5\,W/m^2$ LWN and between $200\,W/m^2$ and $235\,W/m^2$ LWD. Lower frequencies of occurrence in between the peaks mark the transitional state [Stramler et al., 2011; Graham et al., 2017] (figure 4.1). The variable range of the states is not equally wide, as the atmosphere is either clear or has thin ice clouds, that do not influence the downwelling radiation to a significant extent for the clear state. In contrast, the cloudy state has a large variety of cloud properties with different amounts of liquid water, ice and different drop sizes, that cause different amounts of long wave radiation emitted and reflected downwards, from the atmosphere to the surface. LWU does not show two distinguishable states, since the energy flux from subsurface layers dampens the LWU variations due to the states (figure 4.1).

We defined two thresholds, based on LWD and LWN, in order to categorise clear sky periods for the winter 2019/20 MOSAiC observations. Both thresholds, $LWD < 160\,W/m^2$ and $LWN < -30\,W/m^2$, are used in the analysis. On the one hand, the categorisation of clear sky conditions shows

high similarity, in general, as in Raddatz et al. [2015]. On the other hand, small differences due to using different thresholds add even more information. Furthermore, the results are influenced by the threshold choice, for example, the exact timing is directly dependent on the subjectively chosen threshold (see sections 4.1,4.3).
In comparison, a LWN threshold of $-30\,W/m^2$ was found for the SHEBA dataset for a clear sky mode centred at $-40\,W/m^2$. Despite the very distinct conditions, the same clear sky threshold was used in the N-ICE drift studies [Graham et al., 2017]. A LWN threshold of $-25\,W/m^2$ was used to divide the MOSAiC November to December data into the two states [Shupe et al., 2020a], but without taking account for the transition between the states. Batrak and Müller [2019] used $160\,W/m^2$ LWD as a threshold for clear sky events on N-ICE data. Walden et al. [2017] found radiation values of $110\,W/m^2$ to $125\,W/m^2$ LWD and $160-200\,W/m^2$ LWU for the radiatively clear state, for the N-ICE data. In summary, the two Arctic atmospheric winter states are very similar in the named expeditions of different domain and meteorological setting, further proving the applicability on the Arctic. Although the threshold choice is dependent on the exact study objective, the same thresholds could be used for clear sky categorisation in SHEBA, N-ICE and MOSAiC.

Despite the generally high cloud coverage in the Arctic [Sedlar et al., 2021], we find in the MOSAiC winter observations clear sky conditions at 51.5% and 37.7%, by using the related LWN and LWD thresholds. Observed clear sky periods have a short duration of hours to few days and are interrupted by likewise short cloudy periods. The numbers of occurrences is different for the considered months. The difference of the relative occurrences by using the two thresholds is considerable, however, the clear sky timing is surprisingly similar for the two thresholds (see section 4.2). Our analysis of infrared satellite observations showed an overall low cloud coverage on pan-Arctic scales during the two analysed clear sky periods (see section 5.2.1).
For context, 66% of the SHEBA winter time conditions were identified as radiatively clear, fulfilling a threshold of $LWN < -30\,W/m^2$ [Stramler et al., 2011]. SHEBA experienced high pressure conditions anomalously often, which often leads to clear sky conditions. During MOSAiC winter, the positive AO phase and the connected lower air pressure resulted in more cloudy conditions, explaining the lower number of clear sky cases during the MOSAiC winter, compared to the SHEBA period [Stramler et al., 2011; Rinke et al., 2021].

6.2 Representativeness of MOSAiC Winter and Trajectory

Because of progressive climate change and warm autumn 2019 conditions, the Arctic sea ice in winter 2019/20 showed lower than normal thickness, extent and age compared to the climatology of previous decades. On the contrary, this conditions led to stronger thermodynamic and dynamic ice formation and growth. As a consequence, regional and pan-Arctic patterns in sea ice thickness, extent and age, as well as their rates of change, show great differences to the climatology [Perovich et al. [2020]; Krumpen et al. [2021], figure 3.13, section 3.3.2].
The MOSAiC Central Observatory (CO) was deployed at a regional minimum of ice thickness and age, with decreasing difference during the winter, due to the stronger thermodynamic and dynamic ice formation and growth. Along the trajectory, the *sea ice concentration CI* was above average. The CO sea ice conditions are assumed to be representative for the Distributed Network (DN) and the wider surrounding of up to $100\,km$ distance. High local variability of sea ice and the low representativness of point-measurements for large-scale conditions must be taken into account [Krumpen et al. [2021], section 3.3.2].

The analysis of one *snow depth* product showed that the winter 2019/20 was close to the climatology [Krumpen et al., 2021]. However, different snow depth retrieval methods, uncertainties and the changing percentage of MYI and FYI must be taken into account (section 3.3.2).

In general, the winter 2019/20 meteorological conditions were close to the previous decades climatology for a high fraction of the winter and, also, extreme values were inside the climatology range. Still, the strongly positive phase of the Arctic Oscillation (AO) lead to more intense pan-Arctic temperature and air-pressure anomaly patterns than average. These include below average *surface air pressure* in the Arctic and strong westerly winds, locking the cold air inside the Arctic. They also caused frequent and intense storms, as seen in February 2020. Another result is a 20% faster trans-Arctic ice drift [[Ballinger et al., 2020; Krumpen et al., 2021; Rinke et al., 2021], section 3.3.2].

Thus, the MOSAiC winter trajectory could be representative for the Central Arctic, if accounted for the sea ice thickness minimum. Since, local meteorological conditions are related to large scale atmospheric patterns, the MOSAiC trajectory should not show systematic differences to the Central Arctic concerning *snow depth* or atmospheric conditions. Since the Central Arctic characteristics in sea ice, snow and atmosphere are very different to

other parts of the Arctic, such as regions closer to the ice edge or with much lower *ice thickness*, the MOSAiC trajectory might not be representative for the entire Arctic Basin.
The winter 2019/20 sea ice and atmospheric conditions have features, that differ from the climatology strongly and, thus, cannot represent the recent $40\,years$ or even last decade conditions. As the Arctic has undergone large changes within the last decades, the MOSAiC year could be representative for a new Arctic state. In this new Arctic state, stronger storms bringing more heat and moisture towards higher latitudes, might be normal along with a decreased sea ice volume [Rinke et al., 2021]. The MOSAiC winter might still not be representative for winters in the new Arctic, that have significantly different synoptic features, e.g. a negative phase of the AO. The MOSAiC winter can also not represent non-winter seasons or yearly averages.
As the MOSAiC expedition took place in different synoptic, snow and ice settings, than previous expeditions, it compliments previous knowledge. The differences of the studies allow for understanding differences due to regions and meteorological situation, as well as, forming universal statements for the pan-Arctic context and unrelated to specific meteorological characteristics.

We found high similarity for the MOSAIC DN sites L1, L2 and L3. Because of unavailability of L3 following damages of the measurement system by an intense storm and heavy local ice deformation, the L3 record misses extreme conditions in February [Onl, 2020]. The similarities between the stations can be explained by the small distance of $< 30\,km$ between the sites, compared to synoptic scales, at which the main features are caused. In addition, the sites share similar environmental conditions. All measurement sites were deployed on solid ice floes with a reasonable distance to open water, which should cause a common energy flux through the subsurface, if sea ice thickness, snow height and their structural characteristics are common [Shupe et al., 2020a]. As we found no offset between the variables values of the three sites in this study, this is assumed to be true. As consequence, clear sky periods are common for all three sites and L2 is representative for the area of $30\,km$ around the ship, and likely even for a $100\,km$ vicinity. However, we found small differences between the MOSAIC sites L1-L3, likely imposed by local effects. e.g. small clouds and local ice deformation, which can be neglected in our following comparison to the ERA5 reanalysis.

6.3 Representation of Atmospheric Synoptic Aspects in ERA5 and Connection to the Arctic-Atmospheric-States

The Arctic winter surface energy budget and its components are to a large extent driven by the synoptic atmospheric activity and related wind. The related differences in *air pressure* can be steered by large scale atmospheric patterns, like the one described by the Arctic Oscillation positive phase during the MOSAiC winter. *Surface air pressure* might indicate clear sky, as all SHEBA clear sky periods occurred in pressures above $1020\,hPa$, though cloudy conditions also occurred in high pressure in some cases. As some *wind directions* are connected to storms or high pressure systems, they might indicate clear sky conditions. Rapid changes of *wind speed* and *wind direction* and decreasing *surface air pressure* might indicate the onset of a cyclone and the end of a clear sky period [Walden et al., 2017; Kayser et al., 2017; Cohen et al., 2017; Stramler et al., 2011].

Contrasting the theory, for the MOSAiC winter trajectory, the *wind direction* has similar characteristics for both atmospheric states, including rapid changes and periods of constant *wind direction*. Despite very variable *wind directions* in clear sky periods, some of the longest and all having a constant *wind direction*, occur during the monthly mean and constant *wind direction* of 120° to 140° (south-east), e.g. the JAN and FEB periods. Contrasting lower *wind speeds* in clear sky periods in previous studies, the observed *wind speeds* are not clearly related to the direction and atmospheric state in MOSAiC [Graham et al., 2017; Shupe et al., 2020a]. Compared to the exceptionally cold, high pressure SHEBA winter and the warm, synoptically driven, low pressure N-ICE winter, the MOSAiC drift had more moderate *surface air pressure*, which is below average for the Central Arctic [Stramler et al., 2011; Graham et al., 2017; Rinke et al., 2021]. All clear sky periods occurred in $pp > 1000\,hPa$, but also some single cloudy periods did (see sections 4.1, 4.3, 5.1).
In general, *wind speed*, *wind direction* and *surface air pressure* are consistently represented by ERA5, along the MOSAiC winter trajectory (see sections 4.1, 4.3, 5.1).

In summary, there is a relation of *surface air pressure* and wind to the atmospheric states, but not as directly, as for surface radiative variables. Also, simulating atmospheric synoptic aspects is not influencing the ability of ERA5 simulating the clear sky state or the surface radiative energy budget.

6.4 Representation of the Surface Radiative Energy Budget and Clear Sky Periods in ERA5

Large problems were found simulating the surface radiative energy budget, comparing surface long wave radiation variables LWD, LWN and LWU of ERA5 reanalysis to the MOSAiC winter observations along the trajectory.

ERA5 cannot reproduce the observed frequency of occurrence distributions, as it misses the observed bimodal distribution for LWD and LWN (section 4.1). It is possible, that two partly overlapping single distributions exist, which cannot be separated sufficiently in order to be distinguishable from each other. The frequency of occurrence is overestimated for mid-range values and the variable range is not captured, missing on the most extreme variable values (see section 4.1). In addition, ERA5 is underestimating most of the LWD and LWN variability (hourly-to-daily timescales) and it does not capture changing variability during the analysed months (see section 4.3). The temporal evolution of surface radiation variables is captured differently well. LWD and LWN are captured in very rapid and strongly changing conditions related to synoptic conditions, e.g. in the onset of cyclones on the 14.2. and 18.2.2020 or the rapid drop on the 31.12.2019. This shows that ERA5 has high accuracy on synoptic scales, but has problems with small scale regional processes, e.g. resulting cloud coverage (see section 4.3, 5.1). The LWU is simulated too high, with a smaller range, and the temporal evolution is not captured.
The errors in LWU and LWN errors are to a large extent the result of the overestimated energy flux from ocean to atmosphere (see sections 4.1, 4.3, 5.1), which is partly caused by insufficient ice and snow representation (sections 5.2.2, 6.5). Deficiencies in the radiative energy budget could also derive from insufficient modelling of the subsurface heat transfer in ERA5, that is defined by constant, predefined volumetric heat capacity and thermal conductivity of the ice (section 2.1), that are not known well and are likely not homogeneous in space and time. Misrepresentation of the boundary layer and cloud properties can additionally lead to model biases [Kayser et al., 2017; Graham et al., 2017]. Because ERA5 uses CI observations, the identification of sea ice is assumed to be accurate.

Our analysis shows that ERA5 simulates clear sky condition at 58.5% (LWN) and 22.2% (LWD) of the analysed time period. These values slightly under- and overestimate the observed values of 51.5% (LWN) and 37.7% (LWD), respectively. We also performed a detailed verification analysis of ERA5 in terms of *hits*, *misses* and *false alarms* of clear sky conditions, by using both thresholds of LWN and LWU. The results of the verification are however dependent on the threshold choice. As such the

LWN threshold produces more hits, but also more false alarms, compared to the LWD threshold giving less hits and more misses, but also less false alarms. Clear sky periods are often simulated correctly (*hit*) in periods of high (hours to days) variability, despite rapid changes and related low LWD. Vice versa, clear sky conditions are *missed* in low (hours to days) variability. *False alarms* occur in short transitions within hours (see sections 4.2, 4.3, 5.1).

In conclusion, it is questionable if the radiatively clear state and the cloudy opaque state are distinguishable in the ERA5 data. In the measurements a clear separation can already be see in the LWN and LWD frequency of occurrence distributions, which is not the case for ERA5 (section 4.1). Despite the unclear state distinction, the deviations in the radiative energy budget and the missing (hours to days) variability, many clear sky periods are identifiable correctly along the MOSAiC winter trajectory with their timing, but without sufficient variable difference and range due to the states. The ability of simulating the correct timing is dependent on the meteorological conditions, with a better representation in rapid and strong changes of radiation, which is likely to be connected to synoptic activity (sections 4.1, 4.3, 5.1).

6.5 Representation of Surface Temperature in ERA5

The surface temperature is a product of the surface radiative energy budget (see equation 3.5 and 3.3) and, thus, is influenced heavily by the atmospheric states (see section 3.1.1, 4.1). Following, the surface temperature is highly variable in time and has complex regional characteristics in the Arctic.

Lowest surface temperatures along the winter MOSAiC trajectory are observed during clear sky periods, e.g. on the 15.2.2020 with $IST = -39°\mathrm{C}$ (section 4.3,5.1). Still, clouds can occur in low temperatures and clear sky conditions can be found with higher temperatures, explaining the overlapping temperature ranges due to the states in the frequency distribution (see section 4.3, 4.1). One explanation could be, that even colder air gets transported (e.g. from Siberia) to the Central Arctic, as part of a circulation pattern or a synoptic event. This could be the case for the 16th December, when a cyclone passed between the MOSAiC expedition and Siberia [Rinke et al., 2021]. During the analysed clear sky periods, the lowest surface temperatures are observed in the western half of the Arctic, in a spatial context (section 5.2.1).

Highest surface temperatures along the winter MOSAiC trajectory occur during storms, as they bring heat and moisture from lower latitudes, causing

a positive radiative energy budget (section 4.3, 5.1). In a spatial context, regionally warmer surface temperatures and high local temperature gradients can be due to synoptic activity, e.g. for the warm air intrusion around the 14.2.2020 related to multiple cyclones in the Arctic and surrounded by cold air, trapped inside the Arctic by the positive phase of the AO and related strong westerly winds [Rinke et al., 2021] (section 5.2.1). Increased values of SKT_{ERA5} or IST_{MODIS} and can also be generated, because these quantities do not separate between ocean and sea-ice surface. Exposed water surfaces, in locally lower *sea ice concentration*, have relatively high *sea surface temperature*, e.g. for the East Siberian Islands warm areas, that expand with the ice drift and the easterly wind. Thus gradients of surface temperatures can be strong (figure 3.10, section 5.2.1). During clear sky periods, the surface temperatures are highest at the ice margins towards the Atlantic Ocean (section 5.2.1).

ERA5 global atmospheric reanalysis simulates some characteristics of surface temperature and misses others. Spatial characteristics, like local temperature gradients and regional temporal development (e.g. warmer areas north of Fram Strait in JAN, FEB warm air intrusion), can be simulated consistently in spatial extent and shape, but with a temperature error (see section 5.2.1, 5.2.2). ERA5 also simulates the similarity of IST and SKT along the MOSAiC trajectory or other high CI regions, as the sea ice identification is based on CI observations [Hersbach et al., 2020; ECMWF, 2016] (sections 5.2.1, 4.3, figure 3.10).
On one side, ERA5 captures clear sky periods and some features of the surface temperature temporal evolution, for the MOSAiC winter trajectory, e.g. in the onset of a cyclone on the 17.2.2020. On the other side, ERA5 does not capture the surface temperature range, rapid temporal evolution, variability on a scale of hours to days or the temperature difference due to the Arctic states (section 4.1, 4.3, 5.1).

ERA5 has a positive surface temperature error (ΔIST), for most regions and on a pan-Arctic scale. It can occur in both warm and cold temperatures, averaged in time and in single events. The error is not homogeneous in space (sections 4.3, 5.1, 5.2.2).
Along the MOSAiC trajectory, the winter bias (ΔIST_{MOSAiC}) is around 3°C, which is agreeing with the findings of Krumpen et al. [2021]. Occasionally, the error (ΔIST_{MOSAiC}) can be much higher during clear sky conditions and the lowest temperatures (e.g. $\Delta IST_{MOSAiC} \approx 12$°C on the 15.2.2020). Strongly negative ΔIST_{MOSAiC} can occur due to insufficiently simulated variability in the time series (e.g. $\Delta IST_{MOSAiC} \approx -9$°C). The local MOSAiC conditions blend into the observed regional context for clear sky conditions, with $\Delta IST_{MOSAiC}, \Delta IST_{MODIS}$ in the range of 4°C to 5°C. This is consistent with the findings of an 5°C to 10°C clear sky surface tem-

perature error for ERA5 in Batrak and Müller [2019] (sections 4.3, 5.1, 5.2.2).
On a regional scale, we found large errors e.g. north of the North American continent, where sea ice and snow are thick and IST is low, but also at the ice margins with low h_i and higher ΔIST. In the western Arctic with high h_i and h_s, regional patterns of observed higher IST correlate with regional lower ΔIST. ΔIST can be negative in $h_i < 1.5\,m$, where ERA5 overestimates the actual insulation in the Arctic, due to its fixed sea-ice thickness of $1.5\,m$. Smallest errors and biases are often present on thinner ice and snow of very high CI. Still, the largest part of the Arctic has ΔIST in the range of 2°C to 6°C, including MOSAiC. The pan-Arctic bias is around 6°C (section 5.2.2, 5.2.1, figure 3.10).

Error estimates are calculated for comparing ERA5 to MOSAiC along the trajectory, to MODIS spatially and calculating theoretically. The error estimates have many differences, but still are within the same order of magnitude. On a regional scale, ΔIST_{MODIS}, $\Delta IST_{theo.}$ are largest with $\approx$ 10°C , followed by $\Delta IST_{theo:\Delta hs} \approx$ 8°C and $\Delta IST_{theo:\Delta hi} \approx$ 6°C. The pan-Arctic bias is highest in ΔIST_{MODIS}, but as the regional errors cancel out, only slightly lower for the theoretical calculations (section 5.2.2).
Regionally agreeing error estimates could indicate, that assumed error sources h_i and h_s are correct. Thereby, the assumed $h_{i,ERA5}$ and $h_{s,ERA5}$ influence the ΔIST in the same order of magnitude, because the insulating effect is seven times higher for $\Delta h_s \approx 0.2\,m$ than for $\Delta h_s \approx 1.5\,m$ [Batrak and Müller, 2019]. In detail, similar spatial characteristics of h_i and h_s in figure 3.10 have opposite effects on the ΔIST, where the actual h_i is lower than $h_{i,ERA5}$. There, ERA5 overestimates the insulation by ice and snow and, thus, models the IST too low. Thus, the IST errors due to h_i and h_s cancel out, decreasing the total $\Delta IST_{theo.}$ for this regions and the pan-Arctic context (section 5.2.2, figure 3.10).

Despite their influence and importance to the study, the observations of *snow depth* and *sea ice thickness* from CryoSat/SMOS, AMSR-E/2 and AMSR/AVHRR, used for calculating theoretical ΔIST, can have high uncertainties. All $h_{i,CryoSat/SMOS}$, $h_{s,AMSR-E/2}$ and $h_{s,AMSR/AVHRR}$ use error-prone observations as input, calibration and validation, e.g. *sea ice concentration*, sea ice type, temperatures at the atmosphere-snow-ice-ocean interfaces and h_i or h_s, respectively, causing partly large uncertainties. Due to the used observation's limited representativity and the sensitivity of the derival method, accurate products are also limited to certain seasons and snow and ice conditions. The dependence of h_i and h_s increases the uncertainty further, as the methods have problems distinguishing snow and ice. The uncertainty is highest over MYI, in general, but variability in snow and ice conditions can have even larger impact [Ricker et al., 2017; Rostosky

et al., 2018; Lee et al., 2021; Rostosky et al., 2020]. Though the h_s is different for AMSR-E/2 and AMSR/AVHRR, the imposed $\Delta IST_{theo:h_s}$ is very similar (figure 3.10, section 5.2.2).
Observations for the direct comparison of IST (MODIS IST) have small RMSE of 1.6°C and bias of −0.9°C for clear sky conditions, in general [Hall et al., 2004]. If applied on areas with open water surfaces, errors can be large, as MODIS does not account for the warmer SST (section 2.3).

Regionally opposing signals (e.g. Kara Sea large ΔIST_{MODIS} and small theoretical ΔIST) could indicate, that other error sources must be involved. Other error sources for IST_{ERA5}, could be the representation of subsurface heat fluxes in ERA5, which is defined by constant values for sea ice properties, and a *sea surface temperature* of −1.7°C, opposing −2°C used for the theoretical error calculation [ECMWF, 2016]. In addition, ERA5 does not capture the difference between *2m air temperature* and surface temperature and its discrepancy in cloudy and clear sky conditions (section 4.3,5.1). This might indicate, that ERA5 simulates the atmospheric boundary layer with turbulence and surface based inversions insufficiently, as already pointed out by Kayser et al. [2017]; Graham et al. [2017], causing deficiencies in the radiative energy budget and IST_{ERA5}. Characteristics of $dT = T2M - SKT$ and their representation by ERA5 are not analysed further, as it is not in the scope of this work. Furthermore, cloud properties could be misrepresented [Graham et al., 2017].

The analysed clear sky periods show slight ΔIST differences, related to the ice drift, growing h_i and h_s, and different meteorological conditions. In the JAN clear sky period, local and mean regional ΔIST are higher than in the FEB period, despite growing ice and snow layers, because absolute IST were lower. This points out the high influence of absolute IST on the ΔIST, due to differences in subsurface fluxes, which ERA5 cannot simulate adequately. The decrease in extent for regional $\Delta IST_{theo:\Delta hi}$ around −10°C and increasing mean $\Delta IST_{theo:\Delta hi}$, from January to February, can be explained by increasing *ice thickness*. The growing ΔIST_{MOSAiC} and local ΔIST_{MODIS} around the MOSAiC site (≈ +1°C) is consistent with the sea ice and *snow depth* growth from JAN to FEB and the colder IST in the FEB period. The enhanced dynamic and thermodynamic ice growth due to the local minimum in h_i, might be a factor as well [Krumpen et al., 2021]. This is contrasting the pan-Arctic context (see sections 5.1, 5.2.1, 5.2.2, figure 3.10).

In summary, ERA5 global atmospheric reanalysis can simulate some characteristics of the surface temperature and misses others, in time series and a spatial context. ERA5 errors are dependent on the absolute IST, h_i and h_s and are, thus, inhomogeneous in time and space. It could be confirmed, that insufficient representation of h_i and h_s cause errors of IST

in ERA5, still more error sources must be involved. Furthermore, the ERA5 error of surface temperature at the winter MOSAiC site fits into the context of the eastern Central Arctic. Thus, it is not representative for the entire Arctic and does also not exhibit, how large the error can be. It must be taken into account, that the uncertainties of the used satellite observations do impact the results but not necessarily the conclusions.

Chapter 7

Summary & Outlook

7.1 Summary

Since the ERA5 global atmospheric reanalysis is widely used for analysing Arctic conditions and their changes in a warming climate, an understanding of the model's capability to simulate the surface energy budget is crucial. The ERA5 reanalysis deficiencies of the surface radiative energy budget over Arctic sea ice in clear sky condition and possible error sources are analysed for the recent MOSAiC expedition. Analysing the winter period from December 2019 to February 2020, a specific focus is put on two clear sky periods in early January (JAN) and mid-February (FEB). In addition to comparing ERA5 to the MOSAiC measurements along the trajectory, satellite observations of *ice surface temperature* (MODIS), *ice thickness* (CryoSat-2) and *snow depth* (AMSR-E/2, AMSR/AVHRR) are used to further understand the model deficiencies on a pan-Arctic extent.

It was discussed, that the MOSAiC expedition compliments previous drifting observatories, like SHEBA and N-ICE, as it takes place in a different region of the Arctic and in a different meteorological setting. Despite differences, the atmosphere and surface prevail predominantly in the radiatively clear or cloudy opaque state, as for N-ICE and SHEBA, indicating a pan-Arctic applicability. The MOSAiC trajectory was found to be representative for the Central Arctic, but not for the entire Arctic. The MOSAiC winter atmospheric conditions are not representative for the last decades climatology or the recent decade, that have different synoptic conditions. Still, it might be representative for a new Arctic state in similar synoptic setting.

Atmospheric synoptic aspects of near surface wind and air pressure, steered by the two atmospheric states, are represented well in ERA5. The ERA5 reanalysis cannot distinguish the two Arctic atmospheric winter states

at the surface with regards to the radiative surface radiative energy budget. In detail, surface radiation variables are not simulated correctly in range and difference due to the states. In contrast, the timing of clear sky periods is well represented in the reanalysis in the analysed domain and time period.

ERA5 global atmospheric reanalysis simulates some temporal and spatial characteristics of surface temperature and misses others. Because of the deficiencies in the surface radiative energy budget, extreme values are not captured and a warm bias of 3°C was discovered for the December to February MOSAiC trajectory. During clear sky conditions, the bias is higher in a range of 4°C to 6°C, at MOSAiC and in a pan-Arctic context. Regional errors of the surface temperature are high on thick snow and ice and low absolute temperatures. Consequently, MOSAiC does not exhibit how high regional errors can be. It is shown, that a large part of the deficiencies in the surface radiative energy budget and surface temperature, are caused by insufficient representation of *ice thickness* and *snow depth*. Still, other errors are not excluded, leaving room for future studies.

7.2 Outlook

As the surface energy budget over Arctic sea ice is a critical aspect of the Arctic system, also influencing the global climate, it is important to analyse its representation in models, understand uncertainties, and compare against available observations.

MOSAiC accomplished to gather a large variety of data from different components of the Arctic system, at different scales and covering the seasonal cycle. Thus, it could be used for model analysis, validation and in combination with satellite retrievals. Still, the representativity of the MOSAiC observations has to be analysed for the particular application.
For example, future studies could use observations from the MOSAiC campaign for validation or as training data set for satellite products, such as CryoSat/SMOS *sea ice thickness*, AMSR-E/2 and AMSR/AVHRR *snow depth*. Previously used observations are, in some parts, only representative for distinct parts of the Arctic and are not representative for the nowadays Arctic state. Thus, this could expand the applicability of the products to more regions of the Arctic and more seasons, and reduce uncertainty. In detail, future studies could address ice and snow properties (e.g. grain size and density) and their evolution during the seasons, and the distinction of snow and sea ice might be refined.

In conclusion, ERA5 global atmospheric reanalysis can simulate some aspects of the Arctic surface radiative energy budget, but also has several error

sources. Since a large part of the surface radiative energy budget deficiencies are caused by insufficient sea ice and snow representation in the model, the reanalysis could be improved by a sea ice representation with realistic spatial distribution of seasonal evolving *sea ice thickness*. The reanalysis would also benefit from simulations of snow layers on top of the sea ice, that could e.g. be imposed by atmospheric conditions. Both satellite data and expeditional in-situ observations of *snow depth* and *sea ice thickness* could be used for validation. In addition, this study could be repeated with actual snow and ice thickness observations from the MOSAiC campaign to further refine the results.
The study could also be expanded by analysing more error sources, like the subsurface heat transfer in ERA5, e.g. with MOSAiC observations of snow and sea ice properties and the measured subsurface heat fluxes from the ASFS measurement system.
As the stability of the lower atmosphere is influencing the surface energy budget, the representation of the boundary layer could be tested, e.g. using radiosonde data from MOSAiC.

This study could also be expanded by comparing the MOSAIC trajectory and winter 2019/2020 to other reanalyses and models, e.g. MERRA, JRA55 or NCEP.

Bibliography

L3 down! tipped by ice movements. *Online Blog: A Year in the Ice - MOSAiC: Multidisciplinary Drifting Observatory for the Study of Arctic Climate*, 2020. URL `https://mosaic.colorado.edu/news/l3-down-tipped-ice-movements`. (Last access: 16.2.2022).

Cryosat-2/smos merged product description document (pdd). Technical report, AWI, Alfred-Wegener-Institut Helmholtz-Zentrum für Polar- und Meeresforschung and ESA, European Space Agency, 2021a. URL `https://earth.esa.int/eogateway/documents/20142/37627/CryoSat-2-SMOS-Merged-Product-Description-Document-PDD.pdf`. (Last access: 17.2.2022).

Readme-first technical note (rm-tn). Technical report, AWI, Alfred-Wegener-Institut Helmholtz-Zentrum für Polar- und Meeresforschung and ESA, European Space Agency, 2021b. https://earth.esa.int/eogateway/documents/20142/37627/Read-me-first-note-for-the-release-of-theCryoSat-2-SMOS-Merged-Sea-Ice-Thickness.pdf. (Last access: 17.2.2022).

T. J. Ballinger, J. E. Overland, M. Wang, U. S. Bhatt, E. Hanna, I. Hanssen-Bauer, S. J. Kim, R. L. Thoman, and J. E. Walsh. Arctic report card 2020: Surface air temperature. 2020. doi:https://doi.org/10.25923/gcw8-2z06.

D. Barber, K. Dethloff, S. Gerland, C. Inoue, J. Lee, B. Loose, A. Makshtas, W. Maslowski, M. Nicolaus, D. Notz, I. Peeken, D. Perovich, O. Persson, J. Schmale, M. Shupe, M. Tjernström, T. Vihma, and J. Zhao. Mosaic - multidisciplinary drifting observatory for the study of arctic climate - science plan, 2020. URL `https://mosaic-expedition.org/wp-content/uploads/2020/12/mosaic_scienceplan.pdf`. (Last access: 1.12.2021).

Y. Batrak and M. Müller. On the warm bias in atmospheric reanalyses induced by the missing snow over arctic sea-ice. *Nature Communications*, 10(4170), 2019. ISSN 2041-1723. doi:https://doi.org/10.1038/s41467-019-11975-3.

Lana Cohen, Stephen R. Hudson, Von P. Walden, Robert M. Graham, and Mats A. Granskog. Meteorological conditions in a thinner arctic sea ice

regime from winter to summer during the norwegian young sea ice expedition (n-ice2015). *Journal of Geophysical Research: Atmospheres*, 122 (14):7235–7259, 2017. doi:https://doi.org/10.1002/2016JD026034.

ECMWF. *IFS Documentation CY41R2 - Part IV: Physical Processes*. Number 4 in IFS Documentation. ECMWF, 2016. doi:https://doi.org/10.21957/tr5rv27xu.

Robert M. Graham, Annette Rinke, Lana Cohen, Stephen R. Hudson, Von P. Walden, Mats A. Granskog, Wolfgang Dorn, Markus Kayser, and Marion Maturilli. A comparison of the two arctic atmospheric winter states observed during n-ice2015 and sheba. *Journal of Geophysical Research: Atmospheres*, 122(11):5716–5737, 2017. doi:https://doi.org/10.1002/2016JD025475.

D. K. Hall and G. Riggs. *MODIS/Terra Sea Ice Extent 5-Min L2 Swath 1km, Version 6 - USER GUIDE*, 2015a. URL `https://doi.org/10.5067/MODIS/MYD29.006`. (Last access: 1.12.2021).

D. K. Hall and G. Riggs. *MODIS Sea Ice Products User Guide to Collection 6*, 2015b. URL `https://nsidc.org/sites/nsidc.org/files/technical-references/modis-sea-ice-user-guide-C6%5B1%5D.pdf`. (Last access: 1.12.2021).

D.K. Hall, J.R. Key, K.A. Casey, G.A. Riggs, and D.J. Cavalieri. Sea ice surface temperature product from modis. *IEEE Transactions on Geoscience and Remote Sensing*, 42(5):1076–1087, 2004. doi:https://doi.org/10.1109/TGRS.2004.825587.

Hans Hersbach, Bill Bell, Paul Berrisford, Shoji Hirahara, András Horányi, Joaquín Muñoz-Sabater, Julien Nicolas, Carole Peubey, Raluca Radu, Dinand Schepers, Adrian Simmons, Cornel Soci, Saleh Abdalla, Xavier Abellan, Gianpaolo Balsamo, Peter Bechtold, Gionata Biavati, Jean Bidlot, Massimo Bonavita, Giovanna De Chiara, Per Dahlgren, Dick Dee, Michail Diamantakis, Rossana Dragani, Johannes Flemming, Richard Forbes, Manuel Fuentes, Alan Geer, Leo Haimberger, Sean Healy, Robin J. Hogan, Elías Hólm, Marta Janisková, Sarah Keeley, Patrick Laloyaux, Philippe Lopez, Cristina Lupu, Gabor Radnoti, Patricia de Rosnay, Iryna Rozum, Freja Vamborg, Sebastien Villaume, and Jean-Noël Thépaut. The era5 global reanalysis. *Quarterly Journal of the Royal Meteorological Society*, 146(730):1999–2049, 2020. doi:https://doi.org/10.1002/qj.3803.

Markus Kayser, Marion Maturilli, Robert M. Graham, Stephen R. Hudson, Annette Rinke, Lana Cohen, Joo-Hong Kim, Sang-Jong Park, Woosok Moon, and Mats A. Granskog. Vertical thermodynamic structure of the troposphere during the norwegian young sea ice expedition (n-ice2015).

Journal of Geophysical Research: Atmospheres, 122(20):10,855–10,872, 2017. doi:https://doi.org/10.1002/2016JD026089.

T. Krumpen, L. von Albedyll, H. F. Goessling, S. Hendricks, B. Juhls, G. Spreen, S. Willmes, H. J. Belter, K. Dethloff, C. Haas, L. Kaleschke, C. Katlein, X. Tian-Kunze, R. Ricker, P. Rostosky, J. Rückert, S. Singha, and J. Sokolova. Mosaic drift expedition from october 2019 to july 2020: sea ice conditions from space and comparison with previous years. *The Cryosphere*, 15(8):3897–3920, 2021. doi:https://doi.org/10.5194/tc-15-3897-2021.

Sang-Moo Lee, Hoyeon Shi, Byung-Ju Sohn, Albin J. Gasiewski, Walter N. Meier, and Gorm Dybkjær. Winter snow depth on arctic sea ice from satellite radiometer measurements (2003–2020): Regional patterns and trends. *Geophysical Research Letters*, 48(15):e2021GL094541, 2021. doi:https://doi.org/10.1029/2021GL094541. e2021GL094541 2021GL094541.

James E. Overland and Peter S. Guest. The arctic snow and air temperature budget over sea ice during winter. *Journal of Geophysical Research: Oceans*, 96(C3):4651–4662, 1991. doi:https://doi.org/10.1029/90JC02264.

Donald Perovich, W. Meier, M. Tschudi, S. Hendricks, A. A. Petty, D. Divine, S. Farrell, S. Gerland, C. Haas, L. Kaleschke, O. Pavlova, R. Ricker, X. Tian-Kunze, M. Webster, and K. Wood. Arctic report card 2020: Sea ice. 2020. doi:https://doi.org/10.25923/n170-9h57.

R. L. Raddatz, T. N. Papakyriakou, B. G. Else, M. G. Asplin, L. M. Candlish, R. J. Galley, and D. G. Barber. Downwelling longwave radiation and atmospheric winter states in the western maritime arctic. *International Journal of Climatology*, 35(9):2339–2351, 2015. doi:https://doi.org/10.1002/joc.4149.

R. Ricker, S. Hendricks, L. Kaleschke, X. Tian-Kunze, J. King, and C. Haas. A weekly arctic sea-ice thickness data record from merged cryosat-2 and smos satellite data. *The Cryosphere*, 11(4):1607–1623, 2017. doi:https://doi.org/10.5194/tc-11-1607-2017.

Annette Rinke, John J. Cassano, Elizabeth N. Cassano, Ralf Jaiser, and Dörthe Handorf. Meteorological conditions during the MOSAiC expedition: Normal or anomalous? *Elementa: Science of the Anthropocene*, 9(1), 2021. ISSN 2325-1026. doi:https://doi.org/10.1525/elementa.2021.00023.

P. Rostosky, G. Spreen, S. Gerland, M. Huntemann, and M. Mech. Modeling the microwave emission of snow on arctic sea ice for estimating the uncertainty of satellite retrievals. *Journal of Geophysical Research: Oceans*, 125(3):e2019JC015465, 2020. doi:https://doi.org/10.1029/2019JC015465.

Philip Rostosky, Gunnar Spreen, Sinead L. Farrell, Torben Frost, Georg Heygster, and Christian Melsheimer. Snow depth retrieval on arctic sea ice from passive microwave radiometers—improvements and extensions to multiyear ice using lower frequencies. *Journal of Geophysical Research: Oceans*, 123(10):7120–7138, 2018. doi:https://doi.org/10.1029/2018JC014028.

Ted A. Scambos, Terry M. Haran, and Robert Massom. Validation of avhrr and modis ice surface temperature products using in situ radiometers. *Annals of Glaciology*, 44:345–351, 2006. doi:https://doi.org/10.3189/172756406781811457.

J. Sedlar, A. Igel, and H. Telg. Processes contributing to cloud dissipation and formation events on the north slope of alaska. *Atmospheric Chemistry and Physics*, 21(5):4149–4167, 2021. doi:https://doi.org/10.5194/acp-21-4149-2021.

Mark C. Serreze and Roger G. Barry. *The Basic Atmospheric and Ocean Energy Budgets*, page 65–84. Cambridge Atmospheric and Space Science Series. Cambridge University Press, 2 edition, 2014. doi:https://doi.org/10.1017/CBO9781139583817.006.

M. Shupe, O. Persson, C. Cox, M. Gallagher, T. Uttal, D. Costa, J. Osborn, S. Morris, A. Solomon, and D. Perovich. Cloud influences on the surface energy budget at mosaic, 2020a. URL `https://agu2020fallmeeting-agu.ipostersessions.com/?s=76-93-D4-56-F9-16-25-37-8C-01-8B-4B-B6-4A-A5-1F&token=ZgQV_T9CoIZpaHaoNlFzdqnlLfyCWo8OIo5LajtShXE`. (Last access: 15.1.2022).

Matthew D. Shupe, M. Rex, K. Dethloff, E. Damm, A. A. Fong, R. Gradinger, C. Heuzé, B. Loose, A. Makarov, W. Maslowski, M. Nicolaus, D. Perovich, B. Rabe, A. Rinke, V. Sokolov, and A. Sommerfeld. Arctic report card 2020: The mosaic expedition: A year drifting with the arctic sea ice. 2020b. doi:https://doi.org/10.25923/9g3v-xh92.

Kirstie Stramler, Anthony D. Del Genio, and William B. Rossow. Synoptically driven arctic winter states. *Journal of Climate*, 24(6):1747 – 1762, 2011. doi:https://doi.org/10.1175/2010JCLI3817.1.

Taneil Uttal, Judith A. Curry, Miles G. McPhee, Donald K. Perovich, Richard E. Moritz, James A. Maslanik, Peter S. Guest, Harry L. Stern, James A. Moore, Rene Turenne, Andreas Heiberg, Mark. C. Serreze, Donald P. Wylie, Ola G. Persson, Clayton A. Paulson, Christopher Halle, James H. Morison, Patricia A. Wheeler, Alexander Makshtas, Harold Welch, Matthew D. Shupe, Janet M. Intrieri, Knut Stamnes, Ronald W. Lindsey, Robert Pinkel, W. Scott

Pegau, Timothy P. Stanton, and Thomas C. Grenfeld. Surface heat budget of the arctic ocean. *Bulletin of the American Meteorological Society*, 83(2):255 – 276, 2002. doi:https://doi.org/10.1175/1520-0477(2002)083<0255:SHBOTA>2.3.CO;2.

Von P. Walden, Stephen R. Hudson, Lana Cohen, Sarah Y. Murphy, and Mats A. Granskog. Atmospheric components of the surface energy budget over young sea ice: Results from the n-ice2015 campaign. *Journal of Geophysical Research: Atmospheres*, 122(16):8427–8446, 2017. doi:https://doi.org/10.1002/2016JD026091.

M. Webster, S. Gerland, M. Holland, E. Hunke, R. Kwok, O. Lecomte, R. Massom, D. Perovich, and M. Sturm. Snow in the changing sea-ice systems. *Nature Climate Change*, 8:946–953, 2018. doi:https://doi.org/10.1038/s41558-018-0286-7.

T. Zhang, K. Stamnes, and S. A. Bowling. Impact of clouds on surface radiative fluxes and snowmelt in the arctic and subarctic. *Journal of Climate*, 9(9):2110 – 2123, 1996. doi:https://doi.org/10.1175/1520-0442(1996)009<2110:IOCOSR>2.0.CO;2.

Appendix

	ERA5	MOSAiC	MODIS	CryoSat-2/ SMOS	AMSR-E/2	AMSR/ AVHRR
Type	global atmospheric reanalysis	interdisciplinary measurement campaign	satellite retrieval	satellite composite	satellite composite	satellite composite
Variables	LWD, LWN, pp, $u10m$, $v10m$ $T2M$, SKT, $IST/ISTL$	LWD, LWN, pp, w_{dir}, w_{sp}, $T2M$, IST, CI	IST	h_i	h_s	h_s
Assumptions	$hi = 1.5\,m$, $hs = 0\,m$	-	$hi/hs \neq 0\,m$	h_s (W99)	h_i	h_i
Resolution	hourly, 31 km	$10\,min$	$5\,km$	$25\,km$	$25\,km$	$25\,km$
Error/Bias	$\Delta IST \approx 0 - 15°\mathrm{C}$	-	$\Delta IST \approx \pm 3.7°\mathrm{C}$, mean $\Delta IST \approx -2.1°\mathrm{C}$	rel. $\Delta h_i < 25\%$	$rel.\Delta h_s \approx$ 56%(MYI), 93%(FYI)	$\Delta h_s \approx 0.09\,m$, mean $\Delta h_s \approx -0.03\,m$
Main problems (for this study)	insufficient sea ice and snow representation	point measurement	clouds	distinction of snow and ice, h_s	distinction of snow and ice, h_i, representativity limited to spring	distinction of snow and ice, h_i
References	Hersbach et al. [2020], ECMWF [2016]	Shupe et al. [2020b]; Barber et al. [2020]; Shupe et al. [2020a]	Hall et al. [2004]; Hall and Riggs [2015a,b]; Scambos et al. [2006]	Ricker et al. [2017]	Rostosky et al. [2018, 2020]	Lee et al. [2021]

Table 7.1: Overview over used data.

Site	Thresh.	hit	$miss$	$false\ alarm$	Availability
L2	LWN	41.0	10.5	17.5	100
	LWD	17.6	20.1	4.6	100
L1	LWN	40.2	12.7	16.2	100
	LWD	17.7	20.1	5.4	100
L3	LWN	38.1	14.0	17.3	65.7
	LWD	13.1	17.4	5.8	66.6

Table 7.2: Frequencies [%] of (in-) correct clear sky condition simulation, using a threshold of $LWN < -30\,W/m^2$ and $LWD < 160\,W/m^2$, as in table 4.1, but for the MOSAiC sites L1-L3. The frequencies relate to ERA5 correct simulation of occurring clear sky conditions (hit), ERA5 missing to model occurring clear sky conditions ($miss$) and ERA5 falsely simulating clear sky conditions ($false\ alarm$). The frequencies are relative to the individually available number of hourly data from 1.12.2019 to 26.2.2020. The data availability is shown relative to the full number of hours in the given time period.

L2, L1, L3	JAN	FEB
$\Delta T2M_{MOSAiC}$	2.9, 3.0, 2.7	4.2, 4.1, nan
ΔIST_{MOSAiC}	4.0, 4.4, 3.2	5.2, 5.5, nan
ΔSKT_{MOSAiC}	3.5, 3.9, 2.8	4.5, 4.8, nan

Table 7.3: Temperature bias ($\Delta T = T_{ERA5} - T_{MOSAiC}$) [°C] along the MOSAiC L2, L1 and L3 trajectory (1st, 2nd, 3rd values) for the clear sky periods JAN and FEB.

pan-Arctic	JAN	FEB
a) ΔIST_{MODIS}	6.5	5.3
b) $\Delta IST_{theo:\Delta hi(CryoSat/SMOS}$	1.8	6.9
c) $\Delta IST_{theo:\Delta hs(AMSR-E/2)}$	5.8	5.6
c) $\Delta IST_{theo:\Delta hs(AMSR/AVHRR)}$	5.6	5.5
d) $\Delta IST_{theo.(AMSR-E/2)}$	4.3	6.9
d) $\Delta IST_{theo.(AMSR/AVHRR)}$	3.9	4.5

Table 7.4: Pan-Arctic bias of surface temperature [°C] a) compared to MODIS (ΔIST_{MODIS}) and calculated theoretically dependent on b) *ice thickness* ($\Delta IST_{theo:\Delta hi}$), c) *snow depth* ($\Delta IST_{theo:\Delta hs}$) and d) both snow and ice $\Delta IST_{theo.}$, as described in section 5.2.2. The ΔIST in a)-d) relate to the spatial ΔIST a)-d) in figure 5.4,5.5. ΔIST is averaged over the Arctic domain north of $65°N$ with $CI > 80\%$ and in time for the clear sky periods JAN and FEB.

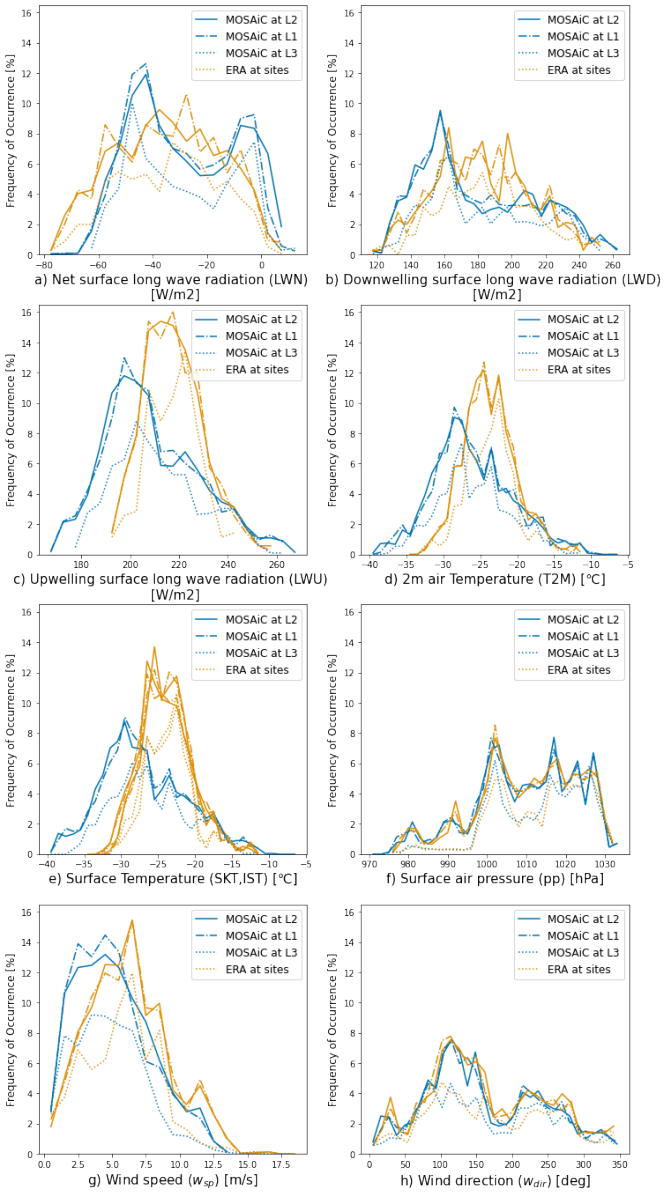

Figure 7.1: Frequency of occurrence of surface and near surface variables for winter MOSAiC observations (blue) and ERA5 reanalysis (orange) at the MOSAiC sites L2 (solid lines, same as in figure 4.1), L1 (dashed-dotted), L3 (dotted) and the associated closest reanalysis grid cell. a) *net surface long wave radiation* (LWN), b) *downwelling surface long wave radiation* (LWD), c) *upwelling surface long wave radiation* (LWU), d) *2m air temperature* ($T2M$), e) *ice surface temperature* (IST), f) *surface atmospheric pressure* (pp), g) *wind speed* (w_{sp}) and h) *wind direction* (w_{dir}). In e), SKT_{ERA5} and IST_{ERA5} are shown with the same colour and line style. The used time period is 1.12.2019 to 26.2.2020. The bin width is $5\,W/m^2$ for all radiative variables.

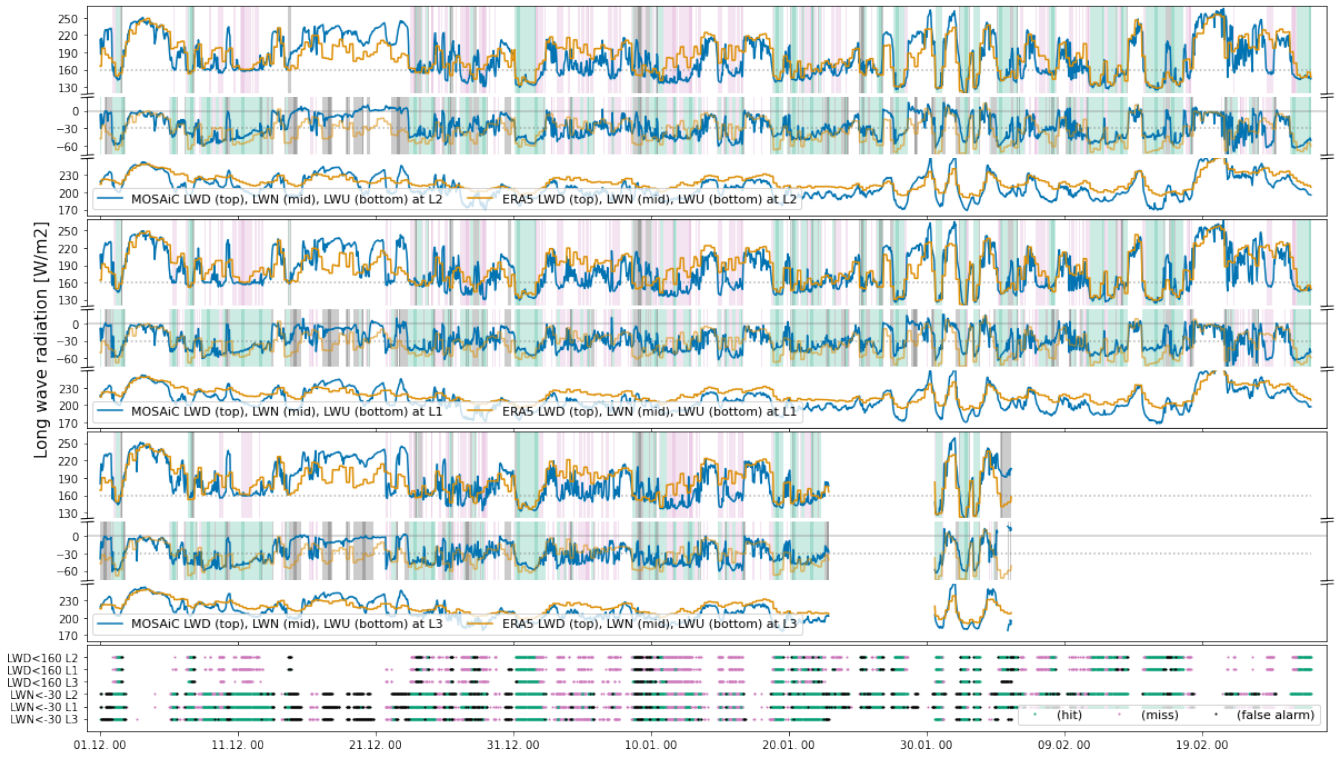

Figure 7.2: Time series of surface radiation variables *downwelling long wave radiation* (LWD) (top), *net long wave radiation* (LWN) (mid) and *upwelling long wave radiation* (LWU) (bottom in sub figure) [W/m^2] for MOSAiC observations (blue) and ERA5 reanalysis (orange) along the MOSAiC L1, L2 and L3 trajectories (first, second and third sub figure), from 1.12.2019 to 26.2.2020. Time periods of (in-) correct clear sky condition simulation are given by background colouring, as in figure 4.2. Correct ERA5 clear sky simulation (*hits*, green), clear sky conditions missed by ERA5 (*miss*, red) and false simulation of clear sky conditions by ERA5 ($false\ alarm$, grey) are marked according to the $LWD < 160\,W/m^2$ threshold within the LWD figure. The LWN figure uses the $LWN < -30\,W/m^2$ threshold accordingly. The respective LWN and LWD thresholds are depicted as horizontal dotted lines. For more detailed comparison, the bottom sub figure shows the times of (in)correctly simulation as horizontal, coloured lines for all sites and thresholds. (Like figure 4.2)

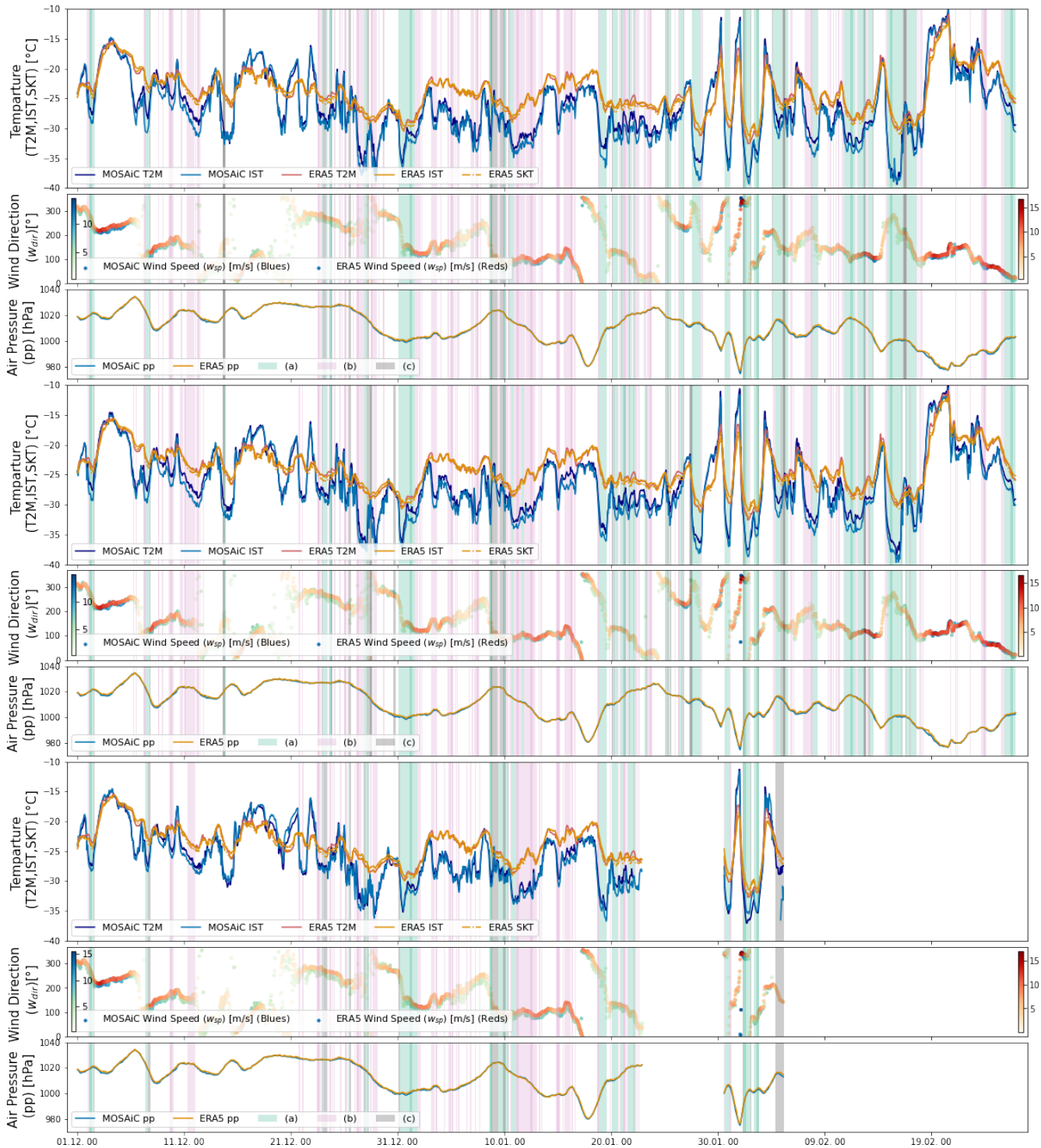

Figure 7.3: Time series of surface and near surface meteorological variables for MOSAiC observations (blue) and ERA5 (orange) reanalysis along the MOSAiC L1, L2 and L3 trajectory (first, second and third sub figure) is shown from 1.12.2019 to 26.2.2020. The sub figures show (top) temperature variables with *2m air temperature* ($T2M$) (darker colours), *ice surface temperature* (IST) (lighter colours) and ERA5 *skin temperature* (SKT_{ERA5}) (dashed), (mid) wind variables with *wind direction* (w_{dir}) (on y-axis) and *wind speed* (w_{sp}) (colour range) and (bottom) *surface air pressure* (pp). Time periods of (in-) correct clear sky condition simulation are given by background colouring, as in figure 4.2. Correct ERA5 clear sky simulation ($hits$, green), clear sky conditions missed by ERA5 ($miss$, red) and false simulation of clear sky conditions by ERA5 ($false\ alarm$, grey) are marked according to the $LWD < 160\,W/m^2$. (Like figure 4.3)

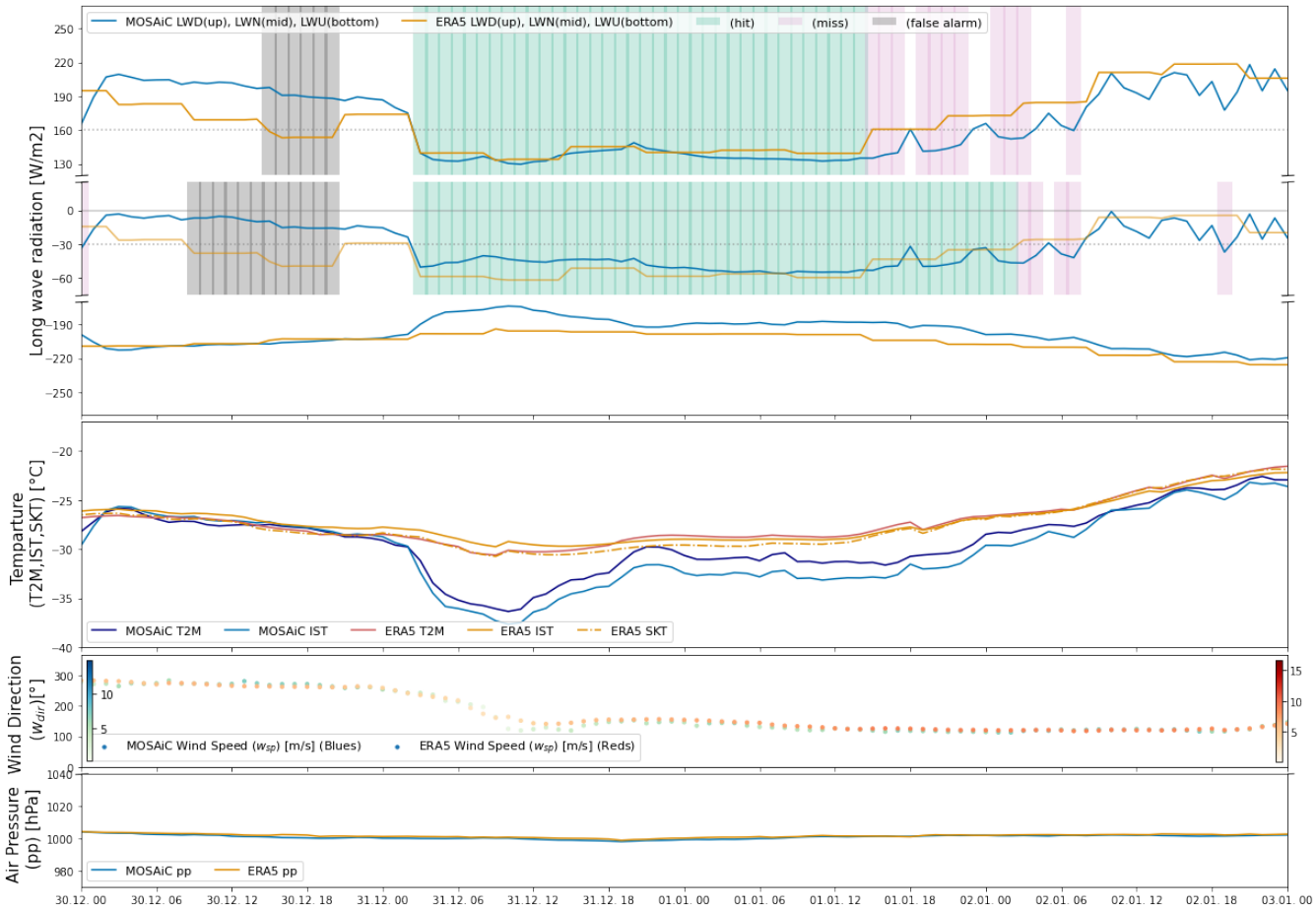

Figure 7.4: Time series of surface and near surface long wave radiation and meteorological variables for MOSAiC observations (blue) and ERA5 reanalysis (orange) along the MOSAiC L1 trajectory for the clear sky period JAN. Shown are (top row) surface radiation variables with *downwelling long wave radiation* (LWD) (top), *net long wave radiation* (LWN) (mid) and *upwelling long wave radiation* (LWU) (bottom) [W/m^2], (second row) temperature variables with *2m air temperature* ($T2M$) (darker colours), *ice surface temperature* (IST) (lighter colours) and ERA5 *surface skin temperature* (SKT_{ERA5}) (dashed), (third row) wind variables with *wind direction* (w_{dir}) (on y-axis) and *wind speed* (w_{sp}) (colour range) and (bottom row) *surface air pressure* (pp). Time periods of (in-) correct clear sky condition simulation are given by background colouring, as in figure 4.2. Correct ERA5 clear sky simulation (*hits*, green), clear sky conditions missed by ERA5 (*miss*, red) and false simulation of clear sky conditions by ERA5 ($false\ alarm$, grey) are marked according to the $LWD < 160\,W/m^2$ threshold within the LWD figure. The LWN figure uses the $LWN < -30\,W/m^2$ threshold accordingly. The respective LWN and LWD thresholds are depicted as horizontal dotted lines. (Like figure 5.1)

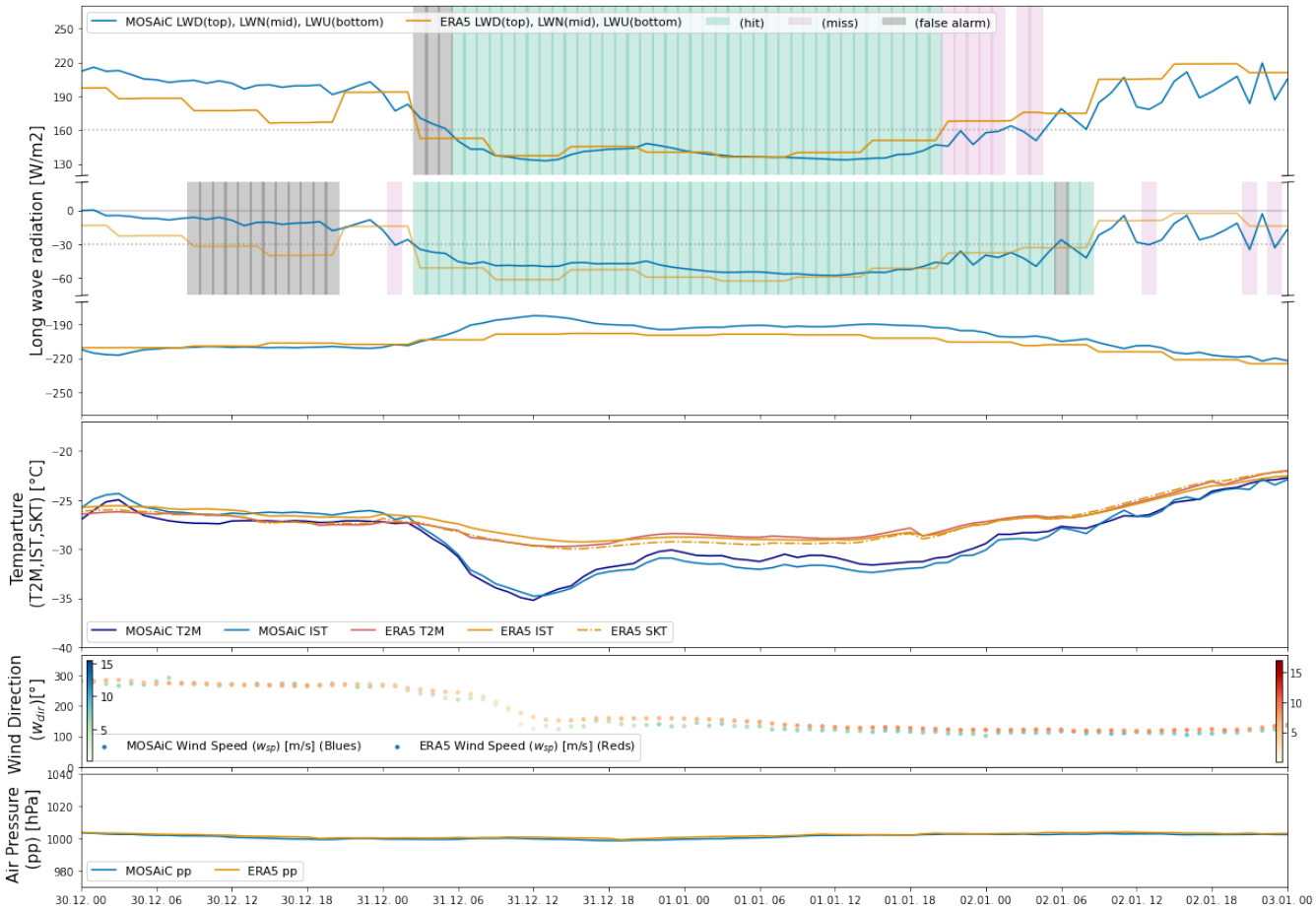

Figure 7.5: Time series of surface and near surface long wave radiation and meteorological variables for MOSAiC observations (blue) and ERA5 reanalysis (orange) along the MOSAiC L3 trajectory for the clear sky period JAN. Shown are (top row) surface radiation variables with *downwelling long wave radiation* (LWD) (top), *net long wave radiation* (LWN) (mid) and *upwelling long wave radiation* (LWU) (bottom) [W/m^2], (second row) temperature variables with *2m air temperature* ($T2M$) (darker colours), *ice surface temperature* (IST) (lighter colours) and ERA5 *surface skin temperature* (SKT_{ERA5}) (dashed), (third row) wind variables with *wind direction* (w_{dir}) (on y-axis) and *wind speed* (w_{sp}) (colour range) and (bottom row) *surface air pressure* (pp). Time periods of (in-) correct clear sky condition simulation are given by background colouring, as in figure 4.2. Correct ERA5 clear sky simulation (*hits*, green), clear sky conditions missed by ERA5 (*miss*, red) and false simulation of clear sky conditions by ERA5 (*false alarm*, grey) are marked according to the $LWD < 160\,W/m^2$ threshold within the LWD figure. The LWN figure uses the $LWN < -30\,W/m^2$ threshold accordingly. The respective LWN and LWD thresholds are depicted as horizontal dotted lines. (Like figure 5.1)

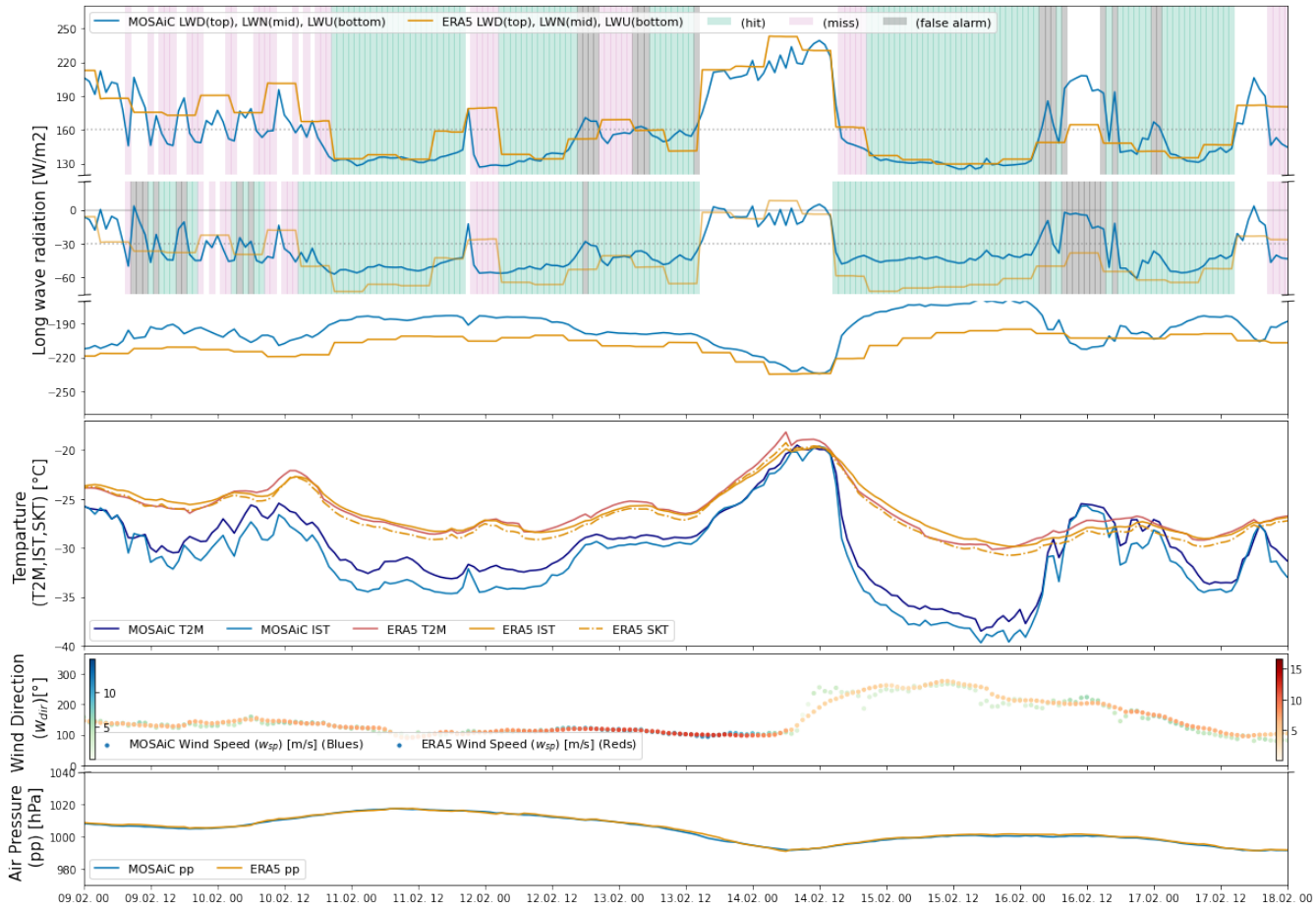

Figure 7.6: Time series of surface and near surface radiation and meteorological variables for MOSAiC observations (blue) and ERA5 reanalysis (orange) along the MOSAiC L1 trajectory for the clear sky period FEB. Shown are (top row) surface radiation variables with *downwelling long wave radiation* (LWD) (top), *net long wave radiation* (LWN) (mid) and *upwelling long wave radiation* (LWU) (bottom) [W/m^2], (second row) temperature variables with *2m air temperature* ($T2M$) (darker colours), *ice surface temperature* (IST) (lighter colours) and ERA5 *surface skin temperature* (SKT_{ERA5}) (dashed), (third row) wind variables with *wind direction* (w_{dir}) (on y-axis) and *wind speed* (w_{sp}) (colour range) and (bottom row) *surface air pressure* (pp). Time periods of (in-) correct clear sky condition simulation are given by background colouring, as in figure 4.2. Correct ERA5 clear sky simulation (*hits*, green), clear sky conditions missed by ERA5 (*miss*, red) and false simulation of clear sky conditions by ERA5 ($false\ alarm$, grey) are marked according to the $LWD < 160\,W/m^2$ threshold within the LWD figure. The LWN figure uses the $LWN < -30\,W/m^2$ threshold accordingly. The respective LWN and LWD thresholds are depicted as horizontal dotted lines. (Like figure 5.2)

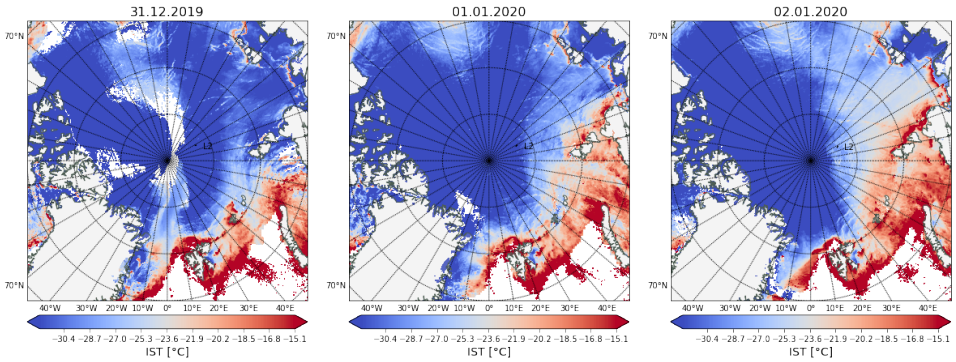

Figure 7.7: Daily mean MODIS *ice surface temperature* (IST_{MODIS}) [°C] in the Arctic on the 31.12.2019, 1.1.2020 and 2.1.2020 (JAN). Areas with $IST_{MODIS} > -2$°C are exempt. The MOSAiC L2 position of that day is marked in black.

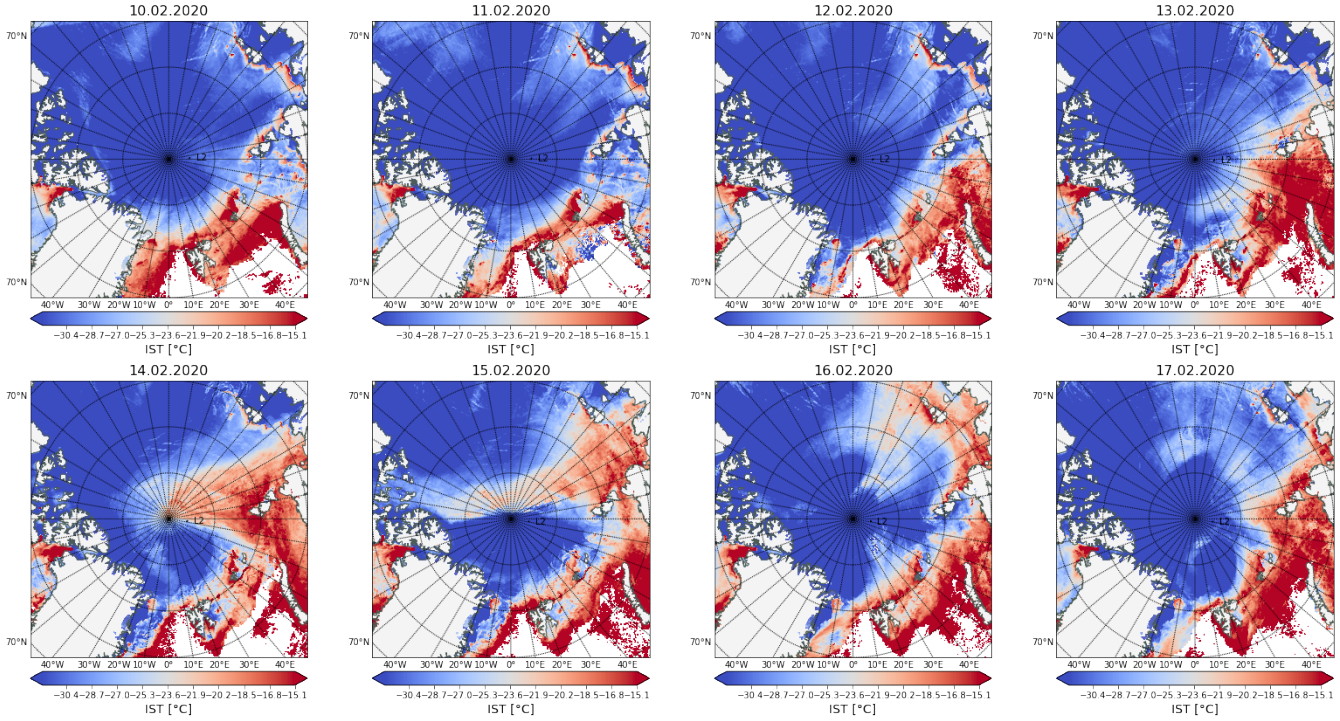

Figure 7.8: Daily mean MODIS *ice surface temperature* (IST_{MODIS}) [°C] in the Arctic for the days from 10.2.2020 to 17.2.2020 (FEB). Areas with $IST_{MODIS} > -2$°C are exempt. The MOSAiC L2 position of that day is marked in black.

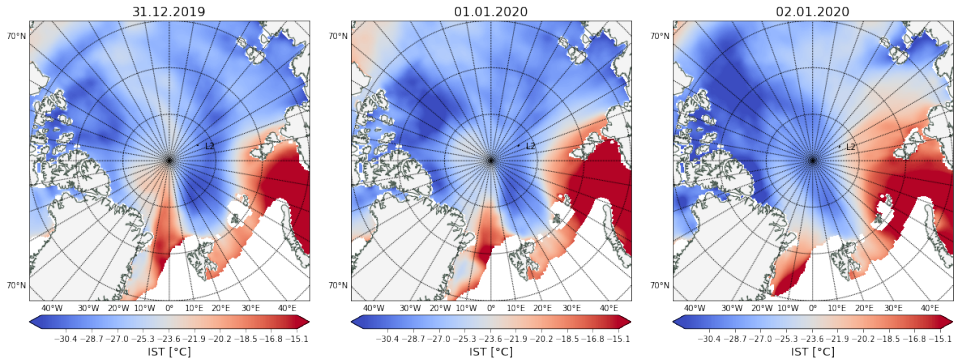

Figure 7.9: Daily mean ERA5 *ice surface temperature* (IST_{ERA5}) [°C] in the Arctic on the 31.12.2019, 1.1.2020 and 2.1.2020 (JAN). Areas with $CI < 80\%$ are exempt. The MOSAiC L2 position of that day is marked in black.

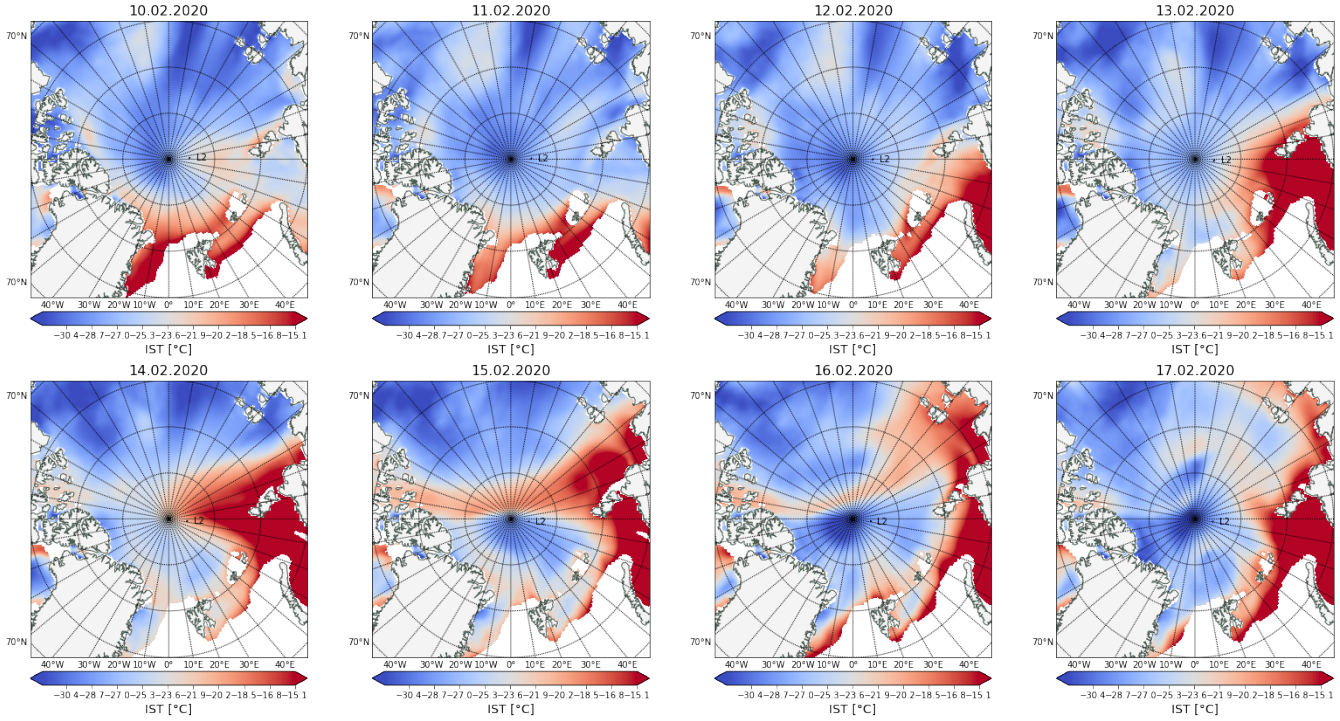

Figure 7.10: Daily mean ERA5 *ice surface temperature* (IST_{ERA5}) [°C] in the Arctic for the days from 10.2.2020 to 17.2.2020 (FEB). Areas with $CI < 80\%$ are exempt. The MOSAiC L2 position of that day is marked in black.